UNIVERSIDAD DE VALPARAÍSO

FACULTAD DE CIENCIAS

CENTRO INTERDISCIPLINARIO DE NEUROCIENCIA DE VALPARAÍSO

THE NEUROMODULATORY INFLUENCE ON FUNCTIONAL NETWORK TOPOLOGY: INSIGHTS FROM NEURAL MASS MODELS

CARLOS MIGUEL CORONEL OLIVEROS

Supervisor
PATRICIO ORIO, PH. D.

A dissertation submitted to the Faculty of Sciences of Universidad de Valparaíso, in partial satisfaction of the requirements for the degree of Doctor of Philosophy in Biophysics and Computational Biology

VALPARAÍSO – CHILE
August 2022

How does one draw a conclusion from such a model? It is almost universally believed that with enough parameters in a model, one can reproduce anything. But it is actually the inability to reproduce some details, while trying as hard as possible to be "faithful", that produces the key clues.

(Kopell, 2005)

ACKNOWLEDGMENTS

This work would have not been possible with the help, directly or indirectly, of so many people that I am lucky to be with. Not only for their academic guidance, but also for their friendship and support.

I want to thank Renny Pacheco, who was my first mentor in neuroscience. His guidance during the development of my undergraduate thesis was a valuable experience to account for. It is incredible how 6 years can go by so fast; now I am finishing the manuscript of a second dissertation. At the end of my undergraduate studies in biology, I met the professor Carlos Mantilla, one of the best that I had during my early years as a student. As a theoretical ecologist, he inspired me with the awesome applications of mathematics to biology. This motivated me to redirect my academic interests towards mathematical and computational neuroscience, to find –or trying to– the principles that rules the brain function. Possible this is more complicated than I believed before, but I am proud of the long run done in the last years to become a junior computational neuroscientist. I want to thank Carmen Andara, Eucandys Fuentes, Carlos Cadenas and Alejandra Cáceres, some excellent professors that I was lucky to meet when I studied biology.

Thanks to my supervisor, Patricio Orio, for his guidance –and extreme patience– during all these years as a graduate student. I am especially grateful not only for the teaching and support, but also for challenging my own work to grow as a more critical scientist. I would like to thank my thesis committee, Rodrigo Cofré, Nicolás Crossley and Enzo Tagliazucchi, who contributes with valuable suggestions that effectively improved the final results of this dissertation.

Fortunately, I was lucky to be in a phenomenal laboratory, where I met excellent scientists and friends. I want to thank to my labmates, Marilyn “Kanela” Gatica, Javier Palma, Jean Paul Maidana, Samy Castro, Kesheng Xu, Miguel Piñeiro, Aland Astudillo, Sebastián Orellana, Mauricio Aspé, Fernando Lehue, Pamela Illescas and Diego Becerra. Thanks for your friendship and all the nice moments. All of you inspired my work in several ways. I also want to thank my “neuro friends” Rubén Herzog and Vicente Medel for your interesting talks and fantastic ideas.

I would like to thank Carsten Gießing and Mac Shine. To Carsten for kindly provided us the empirical recordings used in this work. To both of you for critically discussing my work and

contributing with meaningfully suggestions.

I am grateful to CINV from Universidad de Valparaíso, for being a great center for studying the brain at different scales and with distinct perspectives. I wish to thank ANID for their financial support, which allowed me to be fully dedicated to my research work during these years as a graduate student. I want to thank so many researchers that contribute, indirectly with their own work, with inspiration and ideas to shape the final form of the work presented here.

I would like to thank my whole life, university and new friends, for their guidance, good advice, their support and all the funny moments. Finally, thanks to my family for all their unconditionally care and love. To my parents, María Elena Oliveros and Wilfredo Coronel. There are no words to describe everything you have done for me. Thanks for your support when I started my journey in science twelve years ago. I am proud of how far a small town boy can go. Thanks to my sister, María Coronel, for being my partner and closest friend all these years. Also, thanks to the Coronel-Oliveros big family, always following my progress and adventures. No amount of thanks will ever be enough.

Resumen

En años recientes, los modelos de cerebro completo, informados con datos de neuroimagen, han sido utilizados para hallar mecanismos que permitan explicar el cómo y el porqué de la estructura y dinámica del cerebro. A partir de un conectoma fijo, el cerebro puede manejar la transición entre diferentes patrones de actividad funcional en escalas de tiempo relativamente cortas. Los sistemas neuromodulatorios constituyen un mecanismo plausible para cambiar el flujo de la información dentro del cerebro, remoldeando conexiones funcionales en respuesta a un cambio en el contexto ambiental. Teorías recientes proponen que los sistemas colinérgico y noradrenérgico promueven topologías de red funcionales más segregadas o integradas, respectivamente. A pesar de que los efectos de la acetilcolina y la noradrenalina han sido estudiados extensivamente en humanos usando registros de actividad cerebral no invasivos, el vínculo causal entre los mecanismos biofísicos –atribuidos a los neuromodulares– y el control de la topología de red funcional no es conocido. En esta tesis, utilicé un modelo de cerebro completo de masas neuronales para ganar conocimiento acerca de los mecanismos específicos, relacionados con los sistemas colinérgico y noradrenérgico, que producen un movimiento hacia la segregación o integración funcional. En la primera parte, el muy conocido modelo de Jansen & Rit se utilizó para caracterizar el efecto de la acetilcolina y la noradrenalina sobre la segregación e integración. Herramientas de la teoría de grafos se emplearon para analizar las redes funcional obtenidas con las señales tipo fMRI BOLD simuladas. Mecanísticamente, la neuromodulación colinérgica se modeló disminuyendo los parámetros de acoplamiento global y de inhibición local del modelo. La influencia noradrenérgica se simuló incrementando la pendiente de la función de entrada-salida (llamada ganancia de filtro o neural) de las neuronas piramidales. Los resultados de las simulaciones confirman el efecto pro-segregación (integración) de la acetilcolina (noradrenalina), estableciendo mecanismos biofísicos robustos para simular el impacto de los neuromodudolares en la dinámica a nivel de cerebro completo. Luego, corroboré los resultados del modelo añadiendo el análisis de datos empíricos, encontrando que los efectos del sistema colinérgico son contexto específicos: este promueve la segregación durante una tarea atencional, pero no en condiciones de actividad espontánea. Finalmente, identifiqué algunas regiones claves

en el conectoma de humano que, al ser neuromoduladas por noradrenalina, producen un mayor incremento en la integración funcional. Estas regiones corresponden a los *hubs* estructurales del cerebro, los cuales son piezas claves para facilitar la integración de la actividad cerebral.

ABSTRACT

In recent years, whole-brain models restricted by neuroimaging data have been built to explore causal and mechanistic hypotheses about the structure and dynamics of the brain. From a fixed connectome, the brain can manage the transition between different functional connectivity patterns in relatively short timescales. Neuromodulatory systems constitute a plausible mechanism to change the flow of information within the brain, reshaping functional connections in response to a change in the environmental context. Recent theories propose that cholinergic and noradrenergic systems promote more segregated or integrated functional networks topologies, respectively. Despite the whole-brain effects of acetylcholine and noradrenaline have been extensively studied in humans using non-invasive brain recordings, the causal link between the biophysical mechanisms –ascribed to neuromodulators– and the control of functional network topology is missed. In this dissertation, I employed a whole-brain neural mass model to gain insights about the specific mechanisms, related to the cholinergic and noradrenergic systems, that produce a shift to functional segregation or integration. In the first part, the well known Jansen & Rit model was employed to characterize the effect of acetylcholine and noradrenaline on segregation and integration. Tools from graph theory were used to analyze the fMRI BOLD functional networks obtained through the model. Mechanistically, cholinergic neuromodulation was modeled by decreasing the global coupling and feedback inhibition parameters of the model. The noradrenergic influence was simulated increasing the slope of the input-output sigmoid function (named filter or neural gain) of pyramidal neurons. Simulation results confirmed the pro-segregation (integration) effect of acetylcholine (noradrenaline), establishing robust biophysical mechanisms to simulate the impact of neuromodulators on the whole-brain dynamics. Then, I corroborated the results of the model including the analysis of empirical data, finding that the effects of the cholinergic system are context-dependent: it promotes segregation during an attentional task, but not in resting-state conditions. Finally, I identified some key regions in the human connectome that, when neuromodulated by noradrenaline, produced a stronger increment in functional integration. Those regions corresponded to the brain structural hubs, which are supposed to facilitate the integration of brain activity.

PUBLICATIONS

This thesis work was involved, directly and indirectly, in the next scientific publications:

1. Coronel-Oliveros, C., Cofré, R., & Orio, P. (2021). Cholinergic neuromodulation of inhibitory interneurons facilitates functional integration in whole-brain models. PLoS Computational Biology, 17(2), e1008737. $\rightarrow$ First results chapter, with substantial modifications.

2. Coronel-Oliveros, C., Castro, S., Cofré, R., & Orio, P. (2021). Structural features of the human connectome that facilitate the switching of brain dynamics via noradrenergic neuromodulation. Frontiers in Computational Neuroscience, 61. $\rightarrow$ Third results chapter.

3. Coronel-Oliveros, C., Gießing, C., Medel, V., Cofré, R., & Orio, P. (2022). Whole-brain model of context-dependent effects of cholinergic neuromodulation on functional network properties. Manuscript submitted to Neuroimage. $\rightarrow$ Second results chapter.

4. Coronel-Oliveros, C., Pavel, P., Grace, F., Lucía, Z., Aland, A., Weinstein, A., ... & Orio, P.(2022). High altitude hypoxia is related to changes in EEG Functional Connectivity and network topology. Manuscript in preparation to be submitted in Scientific Reports.

Contents

List of Figures

List of Tables

Chapter 1

Introduction

What I think is beautiful about network science

is that you can use it to derive very

simple intuitions about really complex systems

that . . . just look like a big hairball

. . .

Danielle Bassett

1.1 INTEGRATION AND SEGREGATION IN THE BRAIN

The flexible and adaptive behavior of animals in different environmental contexts is partly possible due to the brain macro-scale "anatomical architecture", also denoted Structural Connectivity (SC), that quantifies the existence of white matter tracts physically interconnecting pairs of brain regions. The brain SC sets the basis for the processing of information by domain-specific systems (segregation), and allows the binding of this specialized processing (integration) to guide adaptive behavior (Dehaene and Changeux, 2011). In fact, integration and segregation are proposed as prominent organizational principles in the brain (Sporns, 2013; Cohen and D'Esposito, 2016; Shine, 2019), and their balance is a crucial element for the dynamical richness and flexibility of neural activity, necessary for the coherent global functioning of the brain (Kelso, 2012; Tognoli and Kelso, 2014).

Using tools from graph theory, the network defined by the connections between brain areas can be characterized in terms of segregation and integration, among other properties. The brain can be divided in anatomical or functional regions. These regions constitute the network's nodes, and the connections between brain areas represent the links. The diverse repertoire of metrics, techniques and tools, employed to characterize brain networks, are briefly described in Rubinov

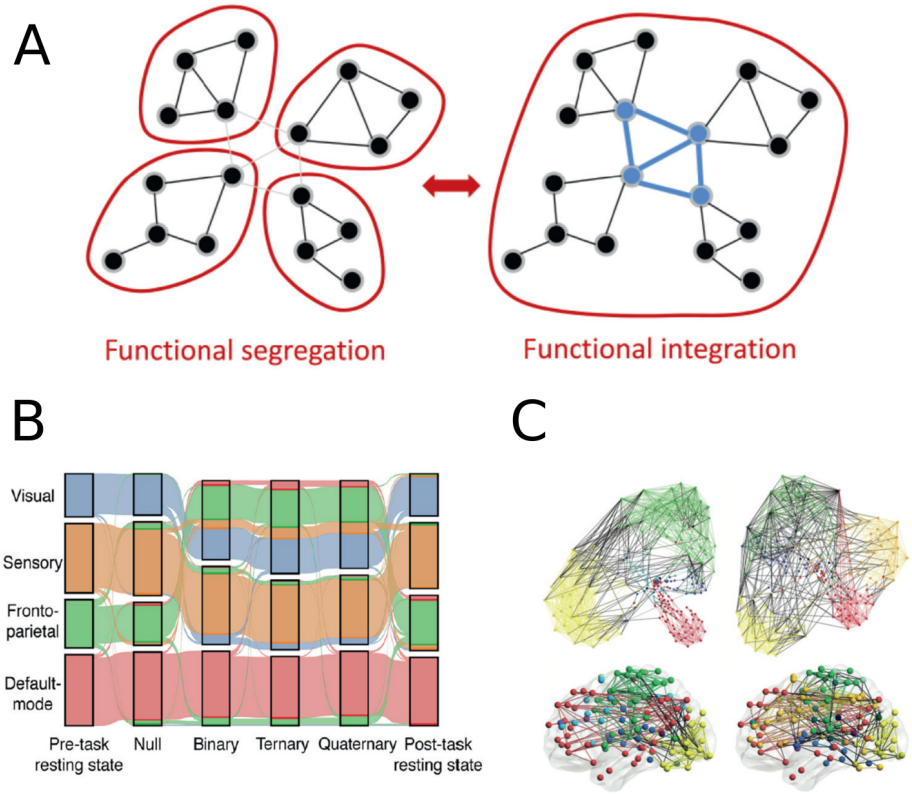

Figure 1.1: Functional brain network topology changes across brain states. A) A more segregated network consisted in modules of clusters with nodes highly intraconnected, but relatively poorly interconnected between them, that is, the between modules connectivity is lower than the within modules connectivity. A more integrated network topology allows the efficient transfer of information between the previously isolated brain modules. **B)** Changes in nodal modules assignment during a Latin square task. In comparison with the pre-task condition, the task promotes a more extensive intermodular configuration. **C)** Network topology differs between different types of tasks: the motor task promoted a more segregated functional network topology, while the N-back a more integrated one. Figure taken from Shine (2019).

and Sporns (2010). Segregation is observed when nodes are grouped in modules or clusters; nodes are highly intraconnected within clusters, and relatively poorly interconnected with non-members of their own module (Fig. 1.1A). Integration is produced when some nodes acts as "bridges", connecting the previously isolated clusters, allowing the transfer of information between them (Fig. 1.1A). Integration and segregation can be quantified both at the level of structural and functional networks, as described below.

At the macro-scale level, neural activity can be measured through electroencephalogram (EEG), magnetoencephalogram (MEG) and functional magnetic resonance imaging (fMRI) recordings, among other techniques. The functional brain organization is typically characterized

using pairwise statistical interdependencies between brain areas (e.g., correlation), building functional connectivity (FC) matrices (Bullmore and Sporns, 2009; González et al., 2016). When applying graph theoretical approaches to the brain's FC, striking fluctuations on the network topology appear between different conditions (Fig. 1.1B). In particular, a more segregated brain network is related to specific motor tasks, making brain regions more domain-specific (Cohen and D'Esposito, 2016) (Fig. 1.1C). In contrast, a reconfiguration towards the integration of the brain's network is observed in complex tasks, and arousal-related states (Cohen and D'Esposito, 2016; Shine et al., 2018b) (Fig. 1.1C). Interestingly, it has been shown that FC in resting-state (RS) conditions reveals a "default" balance between integration and segregation (Cohen and D'Esposito, 2016; Shine et al., 2016; Wang et al., 2021a). This balance changes toward segregation or integration as a function of behavioral tasks (Cohen and D'Esposito, 2016; Shine et al., 2016), or by pathological conditions (Hadley et al., 2016; delEtoile and Adeli, 2017; Chen et al., 2019). However, the SC that provides the basis for shaping the brain dynamics, remains fixed during the short time scales that are relevant for cognitive tasks. Thus, how the brain can manage the transitions between different FC patterns, starting from a fixed connectome? One candidate mechanism corresponds to neuromodulatory systems (Shine, 2019). This will be addressed in the next section.

1.2 CHANGING THE FLOW BY NEUROMODULATION

Neuromodulators change the neuron's response profile without necessarily causing the cell to fire (Thiele and Bellgrove, 2018; Shine et al., 2021), increasing or decreasing the probability of neurons to fire action potentials within entire brain regions. In this way, neuromodulators can change the flow of information within the brain in relatively short timescales, without any modification of the brain SC. In that line, a recent hypothesis pointed out that the cholinergic and noradrenergic systems are key elements in promoting more segregated and integrated functional states, respectively (Shine, 2019).

It is thought that the cholinergic system act increasing the multiplicative gain (Thiele and

Bellgrove, 2018; Shine, 2019), which increments the overall excitability of neurons (that is, the maximum firing rate of the input-output function) (Fig. 1.2). A selective increase in multiplicative gain could produce a more segregated network topology, as remarked by Shine (2019). On the other hand, the noradrenergic system increments the slope of the input-oputput function of excitatory neurons, called neural (or filter) gain (Servan-Schreiber et al., 1990; Aston-Jones and Cohen, 2005; Thiele and Bellgrove, 2018; Shine, 2019).Recent evidence supports that this system might produce a shift to functional integration (Shine et al., 2016, 2018b; Shine, 2019) (Fig. 1.2). At the behavioral level, in-task performance follows an inverted-U relationship with segregation and integration, which depends of the tone of cholinergic and noradrenergic neuromodulation (Shine, 2019) (Fig. 1.2). This complete neuromodulatory framework tries to explain how two opposite network topologies arises from distinct neuromodulatory systems. However, there is a lack of knowledge in how the mechanisms proposed can produce the aforementioned functional changes in the brain. In the case of the noradrenergic system, its effects were more intensively explored using both empirical data and computational models (Shine et al., 2016, 2018a,b; Pfeffer et al., 2021; Wainstein et al., 2021). However, how exactly the cholinergic system can change the functional network topology is a question that remains closed. In the next section I will discuss the specific biological effects of acetylcholine and noradrenaline, and how these effects can be linked to biophysical mechanisms that attempt to explain the effects of neuromodulators at the whole-brain level.

1.2.1 The Cholinergic System

In the cerebral cortex the main source of acetylcholine are projections from the basal forebrain (Kilgard and Merzenich, 1998). At the behavioral level, acetylcholine is involved in several cognitive processes, such as attention, cue detection, and memory (Hasselmo and Sarter, 2011). In the cortex, it has been suggested that acetylcholine could produce a shift from a internal-driven –high influence of excitatory inter-area feedback connections– to a sensory-driven processing of information, increasing the precision of sensory coding (Picciotto et al., 2012; Honey et al.,

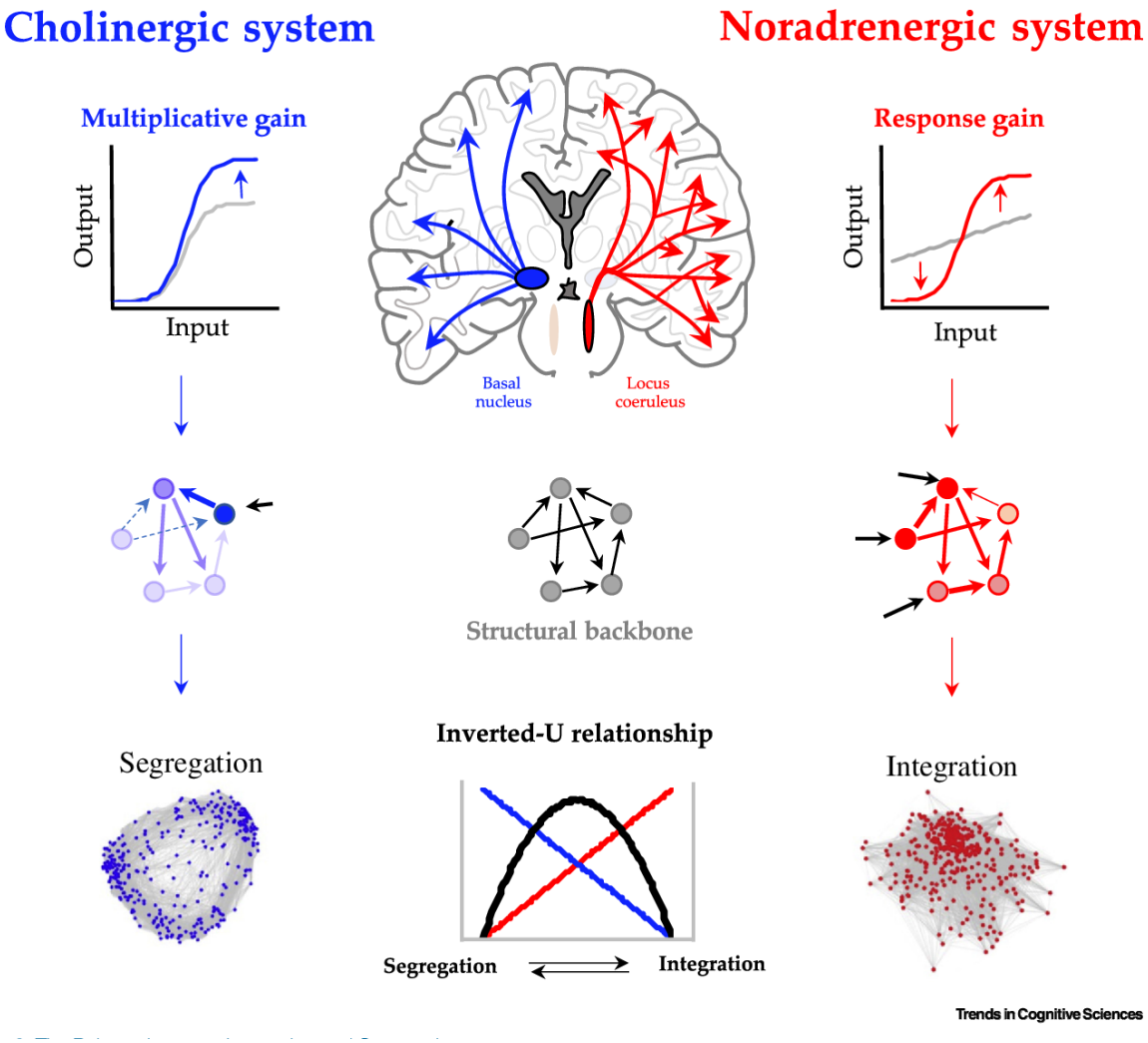

Figure 1.2: Integration and segregation balance. The cholinergic system, by increasing the multiplicative gain, can promote a more segregated functional network topology. The noradrenergic system acts by changing the response (or filter) gain, promoting integration. In-task performance follows an inverted-U relationship with segregation and integration, which can be a result of multiplicate two linear functions belonging to the tone of cholinergic and noradrenergic neuromodulation. Figure taken from Shine (2019).

2017). Following this idea, the cholinergic system can reduce the influence of long-range feedback connections, through mechanisms that rely on both muscarinic and nicotinic receptors (Kimura, 2000; Picciotto et al., 2012; Poorthuis et al., 2013) (Fig. 1.3). Also, the cholinergic system can increase the excitability of pyramidal neurons by reducing the somatic feedback inhibition mediated by interneurons (Kruglikov and Rudy, 2008; Picciotto et al., 2012; Askew et al., 2019) (Fig. 1.3). Regarding nicotinic acetylcholine receptors, activation of β_2-containing receptors by acetylcholine enhances the firing rates of dendritic-targeting gabaergic interneurons –for example, inhibitory

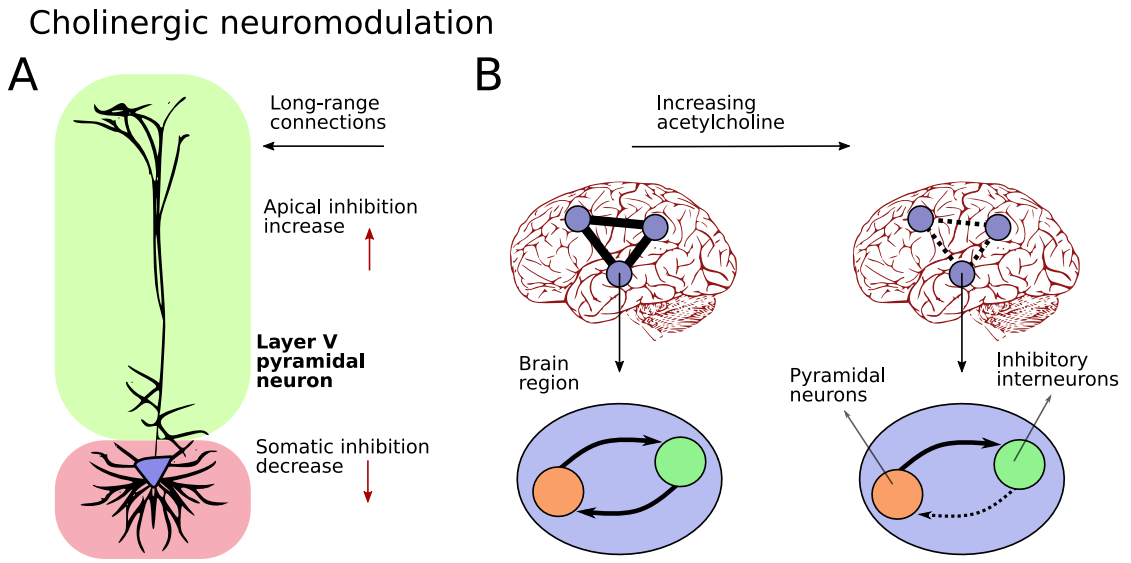

Figure 1.3: Proposed mechanisms of action for cholinergic system. A) Simplified scheme of a layer V pyramidal neuron. Cholinergic system increases apical inhibition –reducing the influence of long-range connections– and decreases direct somatic inhibition. These changes depend on both muscarinic and nicotinic receptors. **B)** When acetylcholine is released, a reduction in global coupling (inter-area connectivity) is produced, alongside a decrease in the local feedback inhibition. In this way, acetylcholine reduces the influence of the internal connectivity compared to external inputs (e.g., from thalamic sources), producing a shift from an internal- to external-driven processing of information.

Martinotti cells (Fino et al., 2013; Tremblay et al., 2016)– increasing the inhibitory tone onto apical section of deep layers pyramidal neurons, and interfering with the feedback connections that arrive to that section (Picciotto et al., 2012; Poorthuis and Mansvelder, 2013; Poorthuis et al., 2013).

The biological summary provided above suggests that a plausible way, using computational models, to simulate the effects of acetylcholine might be the reduction of the global inter-area coupling and the local feedback inhibition. Similar mechanisms were suggested to simulate the effects of cholinergic system in wakefulness, sleep, and behavioral tasks (Deco et al., 2014; Nghiem et al., 2020; Pfeffer et al., 2021), mechanisms that contrast with the increase in multiplicative gain proposed by Shine (2019) for simulating the effect of acetylcholine. However, the link between these mechanisms and the changes in functional network topology is missing. This constitutes one of the strongest points presented in this work, as remarked in **Whole-Brain Models for Understanding Neuromodulation** section.

1.2.2 The Noradrenergic System

The principal source of noradrenaline in the cerebral cortex is the locus coeruleus (LC) (Fuxe et al., 2010). The noradrenergic system is involved in arousal when subjects engage in high-load cognitive tasks (Aston-Jones and Cohen, 2005; Shine et al., 2016, 2018b). For example, in fMRI recordings during a N-back task (for assessing working memory), the pupil diameter –a marker of noradrenergic tone (Reimer et al., 2016)– increases (Shine et al., 2016, 2018b). The GANE model of gain modulation (Mather et al., 2016; Lee et al., 2018) (Fig. 1.4), proposes that the noradrenergic system modulates neural response through an excitatory feedback loop between glutamate receptors on varicosities of LC projections and adrenergic β receptors on presynaptic glutamatergic neurons. At the same time, less activated neurons are suppressed through the action of adrenergic α_2 autoreceptors expressed on the varicosities. The overall result comprises an increase of the neuron responsivity above a threshold, and a decrease of the responsivity below this threshold. This is equivalent to increasing the the slope of the input-output sigmoid function as proposed in Servan-Schreiber et al. (1990) and Aston-Jones and Cohen (2005).

The role of noradrenaline in promoting functional integration was previously addressed by Shine et al. (2016, 2018a,b), and also reported in Pfeffer et al. (2021) using both empirical and simulated data. However, computational models often employ a homogeneous assignment of parameters to simulate the effect of neuromodulation. This is the case of the works of Shine et al. (2018a) and Pfeffer et al. (2021). That is, the effect of neuromodulation, represented by some model's parameters, produced an increase or decrease of these parameters in the same direction and magnitude for overall brain regions. Despite this is the simpler way to model a phenomena through whole-brain models, it is reasonable to think that a selective neuromodulation is employed by the brain; the heterogeneous expression of different brain receptors might constitute the basis for this selective neuromodulation (Shine et al., 2019; Deco et al., 2021a), better explaining the spatiotemporal structure of brain functional connectivity (Deco et al., 2021a). That heterogeneity was incorporated in some computational models, which revealed that the distribution of neurotransmiters' receptors plays a key role in explaining the effects of

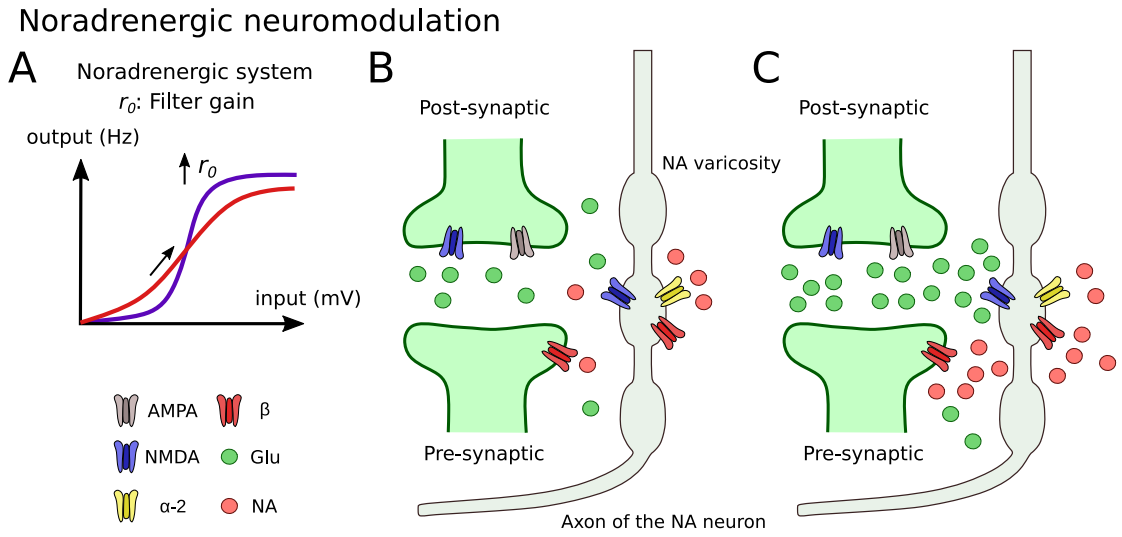

Figure 1.4: Proposed mechanisms of action for noradrenergic system. A) Noradrenaline increase the slope of the input-output function of excitatory neurons (usually a sigmoid function). A higher slope increments the responsivity of neurons to relevant stimuli, and decreases it for non-relevant or noise stimuli. The slope's change can be explained by the glutamate amplifies noradrenaline effects (GANE) model. **B)** An increase of locus coeruleus firing rate promotes the release of noradrenaline (NA) from NA varicosities. Neurons with low activity will not activate enough glutamate (Glu) NMDA receptors on NA varicosities, avoiding the release of extra NA. In consequence, NA binds to the high affinity inhibitory α_2 receptors on NA varicosities. **C)** Neurons with high activity release more glutamate, which promotes the release of extra NA. That produce an increase of NA binding to the low affinity β receptors on both glutamatergic pre-synaptic neurons and the NA varicosities, triggering the release of more glutamate and noradrenaline; the former will bind to Glu NMDA and AMPA receptors of postsynaptic neuron. Thus, noradrenaline increases the excitability of high activated neurons (at the right of the sigmoid function), and produces the opposite effect for low activated ones. Figure adapted from Lee et al. (2018).

neuromodulation (Deco et al., 2018; Kringelbach et al., 2020; Luppi et al., 2021b). I explored, in a very similar way, the effect of noradrenaline acting in a heterogeneous way, point that will be detailed in **Structural Determinants of Functional Switching** and **Whole-Brain Models for Understanding Neuromodulation** sections.

1.2.3 Neuromodulation is Context-Dependent

Computational and experimental work (Coull et al., 1999; Shine et al., 2018b; Pfeffer et al., 2021) suggest that the effects of noradrenergic and cholinergic neuromodulation are context-dependent, that is, different during the task than in RS. Specifically, the changes in FC driven by

neuromodulators depends on the behavioral context that the subject is facing, possibly because the cognitive constraints imposed by the behavioral tasks respect RS (Shine et al., 2018b).

A double dissociation of cholinergic and noradrenegic system was reported by Pfeffer et al. (2021) (Fig. 1.5) . MEG recordings were taken under the effects of donepezil –an acetylcholinesterase inhibitor– and atomoxetine –a noradrenaline reuptake inhibitor–, boosting the levels of acetylcholine and noradrenaline, respectively, in the whole brain (Fig. 1.5A). Brain activity was measured in two different conditions: in RS and during a visual-perceptual task, that consisted in presenting an ambiguous visual image, specifically a sphere without a preferential direction of rotation. They found that atomexetine, and not donepezil, increased the number of sensed changes in rotation direction. Also, atomoxetine incremented pupil diameter in subjects, a marker of arousal states (Reimer et al., 2016), in comparison with donepezil and placebo (Fig. 1.5B). Considering the FC, atomoxetine increased global correlations (i.e. FC strength) during the task, but not in RS. In contrast with the increment in FC produced by atomoxetine, donepezil generated the opposite effect: it decrease the FC strength. However, the effect is also context-dependent, decreasing overall FC in RS strongly in comparison with the task block (Fig. 1.5C). Thus, the effects of donepezil and atomoxetine can be different depending on the behavioral context; differing not only in their behavioral effect, but also at the level of FC. These results highlight the importance of characterizing the effects of drugs not only in RS, but also including the possible alterations in FC during tasks.

The context-dependent effects of atomoxetine were also reported using fMRI data. In an experimental work, Shine et al. (2018b) explored how atomoxetine impacts the functional brain topology in RS and during a N-back task. They found that atomoxetine in RS produces a global shift to a segregated functional network topology (a more modular organization). On the other hand, the drug produces a shift to integration during the task. The authors explain that this dissociation is a consequence of the context, that is, the lack of cognitive constraints at rest. Atomoxetine should potentiate the phasic noradrenergic responses and, in consequence, produce a more integrated functional brain network. However, the boosting of phasic release of noradrenaline will happen only in conditions that effectively trigger a phasic noradrenergic

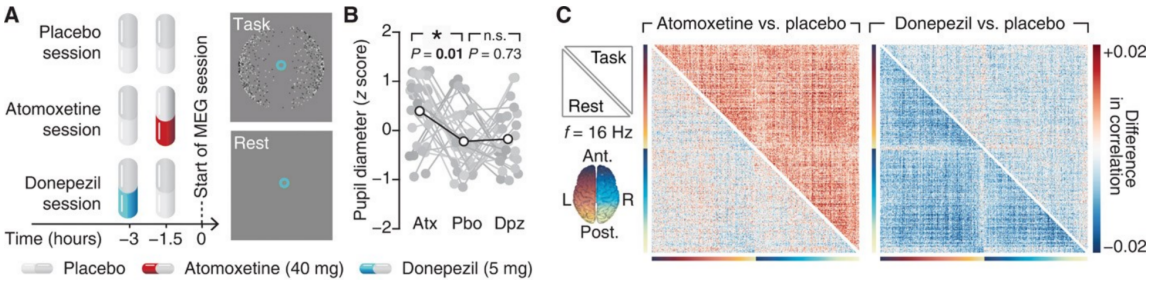

Figure 1.5: Context-dependent effects of neuromodulation. **A)** Magnetoencephalography (MEG) recordings were taken under the effects of donepezil (pro-cholinergic drug) and atomoxetine (pro-noradrenergic drug), and compared to placebo. Brain activity was measured in RS conditions and during a visual-perceptual task. **B)** Atomoxetine, and not donepezil, increases pupil diameter, an indicator of arousal levels and noradrenergic tone. **C)** The effects of neuromodulators are not the same in RS and task. Atomoxetine increases global correlations in task, but not in RS. Donepezil strongly decreases global correlations in RS, in comparison with the task block. Figure taken from Pfeffer et al. (2021).

response (Nieuwenhuis et al., 2011). This is in line with the GANE model (Mather et al., 2016; Lee et al., 2018) described before: low levels of noradrenaline activates inhibitory α_2 receptors, preventing the release of noradrenaline (Fig. 1.4). In a context of increased cognitive load, e.g. during a N-back task, a synergistic effect occurs between the phasic noradrenergic responses triggered by the task, and the increment of the free noradrenaline levels by atomoxetine. This activates the excitatory β receptors, promoting glutamate release in neurons activated by the task, and then producing functional integration. Similar results were reported by Coull et al. (1999), who studied the effects of clonidine (an α_2 adrenergic receptor agonist) using positron emission tomography, both in RS and during an attentional task (a rapid visual information processing task). They found that clonidine, in RS, decreases the functional strength of connections from frontal cortex to thalamus, and also in several connections to and from the visual cortex. On the contrary, during the attentional task, clonidine increases the connectivity from locus coeruleus to parietal cortex, and from parietal cortex to thalamus and frontal cortex. Thus, the results of Coull et al. (1999) suggest a pro-integration effect of clonidine, but limited to the task condition.

In summary, not only the effect of the cholinergic and noradrenergic systems might be pro-segregation and pro-integration, respectively, but also their effects on functional network topology could be context-dependent as remarked by Coull et al. (1999); Shine et al. (2018b); Pfeffer et al. (2021).

Neuromodulators not only change the functional network properties of the brain in a static fashion, but also altered its dynamics. They can promote more flexible brain configurations that easily allow transitions between different functional brain states over time (Shine et al., 2018a,b; Luppi et al., 2021a), or produced more constrained functional network topologies (Shine et al., 2019; Ito et al., 2020). In the next section I delve into this topic with more details.

1.3 FUNCTIONAL CONNECTIVITY DYNAMICS

The complex functional organization of the brain is possible thanks to an anatomical connectivity that combines both integrated and segregated network characteristics, such as small-world and modular properties (Sporns, 2013). In spite of this SC remaining fixed over short timescales, different patterns of FC can be observed during the execution of particular behavioral tasks Cohen and D'Esposito (2016). Moreover, fMRI neuroimaging studies show that during RS the FC is not static, but rather evolves over the recording time (Allen et al., 2014; Hansen et al., 2015; Cabral et al., 2017a), highlighting the non-linear and non-stationary properties of the FC (Guan et al., 2020). This flow of FC patterns over time is known as Functional Connectivity Dynamics (FCD).

The FCD captures how similar are the FC matrices in the entire course of brain recordings (Fig. 1.6). For building the FCD matrix, a method widely employed corresponds to the sliding window approach (Fig. 1.6A). Overlapped time windows are used to estimate the FCs time evolution across an entire set of time series (Fig. 1.6B). Then, the matrices are vectorized and compared against each other using a measure of distance or similarity (e.g., Pearson correlation) (Fig. 1.6C). The result, a time versus time matrix, captures how similar are the FC patterns between two different time windows. The matrix looks like a patchy board, indicating the appearance and vanishing of different FC patterns over time. A very patchy matrix, instead of a monotonous colored one, constitutes a visual way to conceptualize dynamical richness. In a more quantitative way, the FCD matrix could be used to compute measures of multistability and dynamical richness (Orio et al., 2018).

As mentioned before, FCD can be used to characterize the dynamical richness of brain

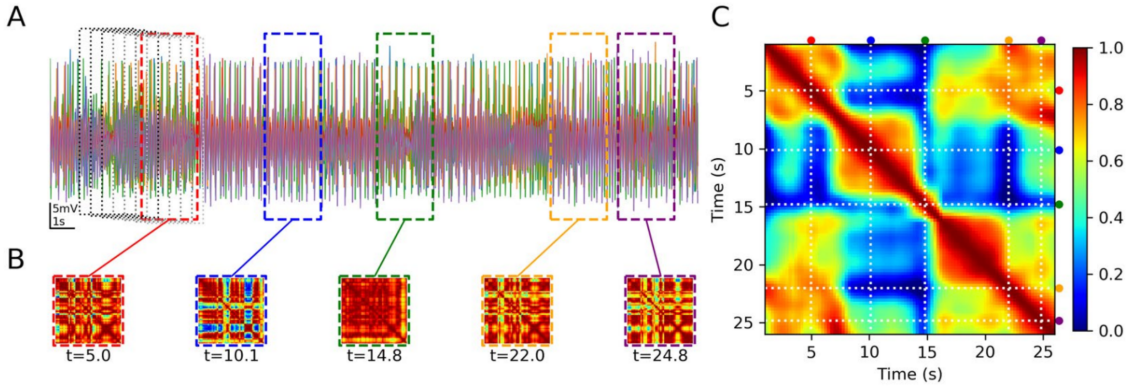

Figure 1.6: Functional connectivity dynamics. A) Time series representing neural activity (e.g, postsynaptic potentials, EEG/MEG recordings, fMRI BOLD signals). Sliding windows of fixed length were used to extract time-dependent features of neural activity. **B)** Within each window, pairwise functional connectivity was computed. **C)** Functional connectivity (FC) matrices can be vectorized and compared against each other using a measure of distance or similarity. The resulting time versus time matrix is known as the functional connectivity dynamics (FCD) matrix. In the example figure, the FCD matrix was built using Pearson correlation. The dotted lines and color points corresponded to the FCs shown in B). Figure taken from Xu et al. (2018).

activity. From a more theoretical motivation, dynamical richness is a crucial element of coordination dynamics (Kelso, 2012; Tognoli and Kelso, 2014); a special feature of the brain which allows the coexistence of multiple brain states. The brain's dynamical richness is a consequence of the multistability. It is defined as the existence of multiple stable states or attractors, which corresponded –in the brain– to distinct patterns of neural activity (Kelso, 2012; Tognoli and Kelso, 2014). If the noise is strong enough, it could produce transitions between the different attractors or brain states. Also, the brain has another property, the metastability. In coordination dynamics, metastability arises in dynamical systems with ghost attractors; in that case, stable and unstable states no longer exist. However, the attraction remains to where the fixed points used to be. That produces, in absence of noise, a dynamical flow where uncoordinated (segregated) and coordinated (integrated) brain states coexist and alternate in time (Kelso, 2012; Tognoli and Kelso, 2014).

It is hypothesized that at rest, the brain maximizes its dynamical repertoire, that is, the possible FCs patterns that can be found in a relatively long period of time (Foster et al., 2016; Shine et al., 2019). From this point, the brain can easily switch to other FC configurations when required (Foster et al., 2016; Shine et al., 2019), that is, when subjects performed a task, or experienced a change in their arousal levels (danger, sleep). From a more clinical and practical

perspective, the FCD had been use as a biomarker for depression (Alonso Martínez et al., 2020), for characterizing brain dynamics in the healthy aging (Cabral et al., 2017b; Battaglia et al., 2020), for testing the effects of drugs in brain activity (Deco et al., 2018; Kringelbach et al., 2020), and to find common mechanisms related to different states of altered consciousness (Luppi et al., 2021a,b).

In a similar way, the integration and segregation of brain activity are not static over time. Theoretical and computational work suggest that, at rest, the human brain balances its functional segregation and integration features, and alternates between more segregated or integrated states in the entire course of brain recordings (Shine et al., 2016, 2018a,b, 2019; Wang et al., 2019; Fukushima and Sporns, 2020; Wang et al., 2021a). A shift occurs (more time in integrated or segregated states) when the behavioral context is changed. Similar to the FCD, the time evolution of functional network topology constitutes marker of dynamical richness at rest. Further, some works reported a correlation between the functional flexibility –a greater disposition to experiment spontaneous changes in FC– with behavioral performance (Shine et al., 2018b; Battaglia et al., 2020).

Far away from the “static scenario”, an interesting topic to be addressed relies on the effect of neuromodulation on brain dynamics. From RS, we can expect that a shift to a more segregated or integrated, faster or slower regimes will be produced under neuromodulation. This will move the brain from its dynamically rich position at rest, to a more redundant (integrated and slower) or disorganized (segregated and faster) regime of activity.

1.4 STRUCTURAL DETERMINANTS OF FUNCTIONAL SWITCHING

While recent theoretical articles point out that a non-uniform neuromodulation can explain better the effects of neuromodulatory systems on brain dynamics (Deco et al., 2018; Kringelbach et al., 2020; Deco et al., 2021a; Luppi et al., 2021b), most studies so far have considered homogeneous neuromodulation, i.e., acting in all nodes in the same way (Deco et al., 2014; Shine et al., 2018a; Pfeffer et al., 2021). For example, incorporating the $GABA_A$ regional receptor expression

betters reproduces the empirical FCD under anesthesia (Luppi et al., 2021b). Similar results were obtained using the 5HT2$_A$ regional expression for simulating the FCD under the effects of LSD (Deco et al., 2018). Using a neural mass model to simulate neural activity, Shine et al. (2018a) showed that rich club regions were strongly neuromodulated compared with non-rich club members, especially between the transition from functional segregation to integration. This work notably suggests that some particular brain regions play a key role in the switching between different functional states via neuromodulation. In fact, brain hubs are key elements for integrating –coordinating– the activity within the brain (Griffa and Van den Heuvel, 2018). Thus, it is possible that a focused neuromodulation can target, preferentially, the brain hubs, because their determinant role in coordinating brain activity as the "network pivots" of the brain (Deco et al., 2017; Griffa and Van den Heuvel, 2018).

In my work, instead of quantifying what regions would be strongly neuromodulated, I studied how much would be the impact on integration and segregation of the neuromodulation of specific subsets of nodes, and analyzed the structural features that define the nodes that, upon modulation, have the largest effect on the network dynamics as a whole.

In a more macro-scale scenario, there is evidence about the importance of network properties of the human connectome (Cabral et al., 2014; Zamora-López et al., 2016; Wang et al., 2019; Castro et al., 2020). For example, its hierarchical modular organization is needed to sustain a richer brain dynamics (Zamora-López et al., 2016; Wang et al., 2019). Then, the repertoire of network configurations, as a way to conceptualize the dynamical richness, can be affected by neuromodulation. I explored how the more macro-scale features of the human SC set the basis for the effects produced by neuromodulation.

1.5 WHOLE-BRAIN MODELS FOR UNDERSTANDING NEUROMODULATION

Whole-brain models can be used to gain insights about possible mechanisms, employed by the brain, to sustain the healthy brain function. Models can be used to perform *in silico* experiments, which can be very difficult to execute in living beings. A good model should be capable of

answer three fundamental questions (Blohm et al., 2020). 1) *What?*: the experimental results. 2) *How*: the underlying mechanisms of action that produce these results. 3) *Why?* the motivation (or reason) of the "entity" to use the described mechanisms and the possible relationships with the experimental observations. In the case of neuromodulation, the model should be capable of 1) reproduced the changes in functional network topology by neuromodulation described experimentally (Gießing et al., 2013; Shine et al., 2018b; Pfeffer et al., 2021); 2) proposed plausible biophysical mechanisms for explaining the effects of neuromodulation (Deco et al., 2014; Shine et al., 2018a; Nghiem et al., 2020; Pfeffer et al., 2021); and 3) explain (or try to) how the changes produced by neuromodulators are related to behavior (Gießing et al., 2013; Shine et al., 2018b).

Next, I will summarize what we know (and what we don't) about neuromodulation and its impact on the topology of brain functional networks:

- We know: cholinergic and noradrenergic systems might promote functional segregation and integration, respectively (Shine, 2019).
- We know: the mechanisms of action, at the micro-scale level of cholinergic and noradrenergic neuromodulation (Servan-Schreiber et al., 1990; Aston-Jones and Cohen, 2005; Picciotto et al., 2012; Mather et al., 2016; Thiele and Bellgrove, 2018; Shine et al., 2021).
- We don't know: how these mechanisms can produce a shift to segregation or integration at the macro-scale (whole-brain) level. There are some works (Deco et al., 2014; Shine et al., 2018a; Nghiem et al., 2020; Pfeffer et al., 2021) that attempt to address this point, but the link between the mechanisms, the empirical data and the changes in functional network topology is missing.
- We know: the effects of acetylcholine and noradrenaline are context-dependent (Shine et al., 2018b; Pfeffer et al., 2021).
- We don't know: whether the MEG results of Pfeffer et al. (2021) apply to fMRI BOLD data, and whether the changes in network topology are context-dependent too.

- We know: several works suggest that noradrenergic neuromodulation promotes functional integration (Shine et al., 2018b; Pfeffer et al., 2021).
- We don't know: what the influence of the cholinergic system on the integration/segregation balance is.
- We know: brain hubs are strongly influenced by neuromodulation (Deco et al., 2017; Shine et al., 2018a; Castro et al., 2020; Herzog et al., 2020).
- We know: the heterogeneous expression of neurotransmitters' receptors might be the basis for a selective neuromodulation of brain regions (Deco et al., 2018; Shine et al., 2018a; Luppi et al., 2021b).
- We don't know: what brain regions, based on the features of the human connectome, facilitate the transition to functional integration when neuromodulated (e.g., by noradrenaline).

The points that we don't know will be addressed in three different chapters of this thesis. In **Results Part One: Cholinergic and Noradrenergic Switching of Functional Network Topology**, I analyzed, using a whole-brain neural mass model, if the mechanisms of action for cholinergic and noradrenergic systems can promote a more segregated or integrated functional network topologies, respectively. When coupling the neural mass model to a hemodynamic model to simulate BOLD-like signals, I obtained functional networks whose topology was analyzed using tools from graph theory. The **Results Part Two: Whole-Brain Model of Context-Dependent Effects of Cholinergic Neuromodulation on Functional Network Properties** constitutes a link between the model and the empirical data. I first analyzed empirical fMRI recordings under the effects of nicotine, in two different blocks: RS and during an attentional task. In this way, I attempted to answer two questions: if the cholinergic system is really pro-segregation, and if the effects are context-dependent. Then, I proposed mechanisms of action to reproduce the possible context-dependent effects of nicotine. Moreover, I correlated the subjects' performance in the task with the changes in the functional network topology. In **Results Part Three: Structural Features of the Human Connectome That Facilitate the Switching of Brain Dynamics via Noradrenergic Neuromodulation**, I identified key regions in the human connectome that, when

neuromodulated by noradrenaline, produced a greater increase in functional integration. That regions could be used by the brain to easily switch from different functional states. Finally, in **Discussion**, I analyzed the results under the light of the current literature, with emphasis in the usefulness of the computational approach employed to extent the knowledge of how neuromodulation works, and what are the behavioral and functional consequences, in the brain, of the neuromodulatory influence.

Chapter 2

Hypothesis and Objectives

2.1 HYPOTHESIS

Hypothesis 1: *the cholinergic and noradrenergic systems promote whole-brain functional segregation and integration, respectively.*

Hypothesis 2: *the effect of cholinergic neuromodulation on functional network topology is context-dependent, that is, not the same during tasks than in resting-state. Specifically, I hypothesize that nicotine produces a more segregated functional network topology in the task condition, which correlates with in-task performance.*

Hypothesis 3: *there is a set of nodes which, upon being neuromodulated by noradrenaline, will have a greater overall effect on the functional integration of the brain.*

2.2 MAIN OBJECTIVE

Study how the cholinergic and noradrenergic neuromodulatory systems change the functional network topology, both in simulated and empirical data.

2.3 SPECIFIC OBJECTIVES

1. Characterize, using a whole-brain neural mass model, the effects of cholinergic and noradrenergic systems on functional integration and segregation.
2. Analyze the possible changes in FC, from experimental and simulated fMRI BOLD recordings, under the effects of a pro-cholinergic drug (i.e., nicotine) in two different blocks: RS and during an attentional task.

3. Study how a selective noradrenergic neuromodulation of brain regions impacts the functional network topology.

Chapter 3

Methods

This chapter was divided into four sections. The first one, **General Methods**, describes the common procedures shared by all results. The **Specific Methods 1**, comprehends all the methods of the first part of results, related to computational modeling of cholinergic and noradrenergic systems by an exhaustive parameter exploration. The **Specific Methods 2**, includes the description of empirical datasets used to study the effect of cholinergic system on function brain network topology, alongside the approach employed to fit the model to the empirical data. In the last one, **Specific Methods 3**, methods for selective noradrenergic neuromodulation were described.

Relevant changes in model parameters or data analysis will be commented within each section. If not, the reader might assume that no important changes were made from **General Methods**.

3.1 GENERAL METHODS

3.1.1 Whole-Brain Neural Mass Model

I simulated neuronal activity using the Jansen & Rit neural mass model (Jansen et al., 1993; Jansen and Rit, 1995). In this model, a brain area consists of three populations of neurons: pyramidal neurons, excitatory and inhibitory interneurons (Fig. 3.1A). The dynamical evolution of the three populations within the brain areas is modeled by two blocks each. The first block transforms the average pulse density in average postsynaptic membrane potential (which can be either excitatory or inhibitory) (Fig. 3.1B). This block, denominated post synaptic potential (PSP) block, is represented by an impulse response function. For the excitatory outputs:

$$h_E(t) = \begin{cases} Aate^{-at}, & t \geq 0 \\ 0, & t < 0 \end{cases} \tag{3.1}$$

and for the inhibitory ones

$$h_I(t) = \begin{cases} Bbte^{-bt}, & t \geq 0 \\ 0, & t < 0, \end{cases} \tag{3.2}$$

The constants A and B define the maximum amplitude of the PSPs for the excitatory (EPSPs) and inhibitory (IPSPs) cases respectively, while a and b represent the inverse characteristic time constants for the excitatory and inhibitory postsynaptic action potentials, respectively. The second block transforms the postsynaptic membrane potential in average pulse density, and is given by a sigmoid function of the form

$$S(\nu, r) = \frac{\zeta_{max}}{1 + e^{r(\nu_{th} - \nu)}}, \tag{3.3}$$

with ζ_{max} as the maximum firing rate of the neuronal population, r the slope of the sigmoid function, ν_{th} the half maximal response of the population, and ν their average PSP. Additionally, pyramidal neurons receive an external background input $p(t)$, whose values are taken from a Gaussian distribution with mean μ (impulses/s) and standard deviation σ. The values of μ and σ were indicated in **Exploring Parameter Space**, **Nicotine and Task modeling** and **Selective Neuromodulation**. In the model, each node $i \in [1 \dots n]$ represents a single brain area. The global coupling is scaled by a parameter α, and nodes are connected by a structural connectivity matrix M (Fig. 3.1C). This matrix is derived from a human connectome (Deco et al., 2018) parcellated in $n = 90$ cortical and subcortical regions (listed in Table1) with the automated anatomical labeling (AAL90) atlas (Tzourio-Mazoyer et al., 2002); the matrix is undirected and takes values between 0 and 1. Because long-range connections are mainly excitatory (Gilbert et al., 1990; McGuire et al., 1991), only links between the pyramidal neurons of a node i with pyramidal neurons of a node j

are considered. The set of equations, for a node i, includes the within and between nodes activity

$$\begin{aligned}
\dot{x}_{0,i}(t) =& y_{0,i}(t) \\
\dot{y}_{0,i}(t) =& Aa\left[S(C_2 x_{1,i}(t) - C_4 x_{2,i}(t) + C\alpha z_i(t), r_0)\right] - 2a y_{0,i}(t) - a^2 x_{0,i}(t) \\
\dot{x}_{1,i}(t) =& y_{1,i}(t) \\
\dot{y}_{1,i}(t) =& Aa\left[p(t) + S(C_1 x_{0,i}(t), r_1)\right] - 2a y_{1,i}(t) - a^2 x_{1,i}(t) \\
\dot{x}_{2,i}(t) =& y_{2,i}(t) \\
\dot{y}_{2,i}(t) =& Bb\left[S(C_3 x_{0,i}(t), r_2)\right] - 2b y_{2,i}(t) - b^2 x_{2,i}(t) \\
\dot{x}_{3,i}(t) =& y_{3,i}(t) \\
\dot{y}_{3,i}(t) =& A\bar{a}\left[S(C_2 x_{1,i}(t) - C_4 x_{2,i}(t) + C\alpha z_i(t), r_0)\right] - 2\bar{a} y_{3,i}(t) - \bar{a}^2 x_{3,i}(t)
\end{aligned} \tag{3.4}$$

where x_0, x_1, x_2 correspond to the local outputs of the PSP blocks of the pyramidal neurons, and excitatory and inhibitory loops, respectively, and x_3 the long-range outputs of pyramidal neurons. The constants C_1, C_2, C_3 and C_4 scale the connectivity between the neural populations (see Fig. 3.1A). I used the original parameter values of Jansen & Rit (Jansen et al., 1993; Jansen and Rit, 1995), except for C_4: $\zeta_{max} = 5$ s^{-1}, $\nu_{th} = 6$ mV, $r_0 = r_1 = r_2 = 0.56$ mV^{-1}, $a = 100$ s^{-1}, $b = 50$ s^{-1}, $A = 3.25$ mV, $B = 22$ mV, $C_1 = C$, $C_2 = 0.8C$, $C_3 = 0.25C$, and $C = 135$. The parameter C_4 was not the same for all simulations, and was defined in **Exploring Parameter Space**, **Nicotine and Task modeling** and **Selective Neuromodulation**. Parameter values can be consulted in Table 2. For comparison, the default value of C_4, proposed in (Jansen et al., 1993; Jansen and Rit, 1995), is equal to $0.25C$

The parameters A, B, a and b were selected to produce IPSPs longer in amplitude and latency in comparison with the EPSPs. The inverse of the characteristic time constant for the long-range EPSPs was defined as $\bar{a} = 0.5a$. This choice was based on the fact that long-range excitatory inputs onto pyramidal neurons target their apical dendrites, and consequently this slows down the time course of the EPSPs at the soma (Branco and Häusser, 2011).

The input from brain areas $j \neq i$ to the region i is given by

$$z_i(t) = \sum_{j=1, j\neq i}^{n} M_{ij} x_{3,j}(t) \tag{3.5}$$

The average PSP of pyramidal neurons in region i characterizes the EEG-like signal in the

Brain regions	
Precental gyrus	Lingual gyrus
Superior frontal gyrus, dorsolateral	Superior occipital gyrus
Superior frontal gyrus, orbital part	Middle occipital gyrus
Middle frontal gyrus	Inferior occipital gyrus
Middle frontal gyrus, orbital part	Fusiform gyrus
Inferior frontal gyrus, opercular part	Postcentral gyrus
Inferior frontal gyrus, triangular part	Superior parietal gyrus
Inferior frontal gyrus, orbital part	Inferior parietal
Rolandic operculum	Supramarginal gyrus
Supplementary motor area	Angular gyrus
Olfactory cortex	Precuneus
Superior frontal gyrus, medial	Paracentral lobule
Superior frontal gyrus, medial orbital	Caudate nucleus
Gyrus rectus	Lenticular nucleus, putamen
Insula	Lenticular nucleus, pallidum
Anterior cingulate and paracingulate gyri	Thalamus
Median cingulate and paracingulate gyri	Heschl gyrus
Posterior cingulate gyrus	Superior temporal gyrus
Hippocampus	Temporal pole: superior temporal gyrus
Parahippocampal gyrus	Middle temporal gyrus
Amygdala	Temporal pole: middle temporal gyrus
Calcarine fissure and surrounding cortex	Inferior temporal gyrus
Cuneus	

Table 3.1: List of brain regions regions of AAL90 parcellation. The atlas comprises 90 brain areas (45 per hemisphere).

source space; it is computed as (Jansen et al., 1993; Jansen and Rit, 1995)

$$\nu(t)_i = C_2 x_{1,i}(t) - C_4 x_{2,i}(t) + C\alpha z_i(t) \tag{3.6}$$

The firing rates of pyramidal neurons, defined as

$$\zeta_i(t) = S(\nu(t)_i, r_0) \tag{3.7}$$

were used to simulate the fMRI BOLD-like signals.

The system of stochastic differential equations (3.4) was solved with the Euler–Maruyama method, using an integration step of 1 ms. Codes were written in Python and are available in `https://github.com/vandal-uv/Structural_Neuromod_2021`.

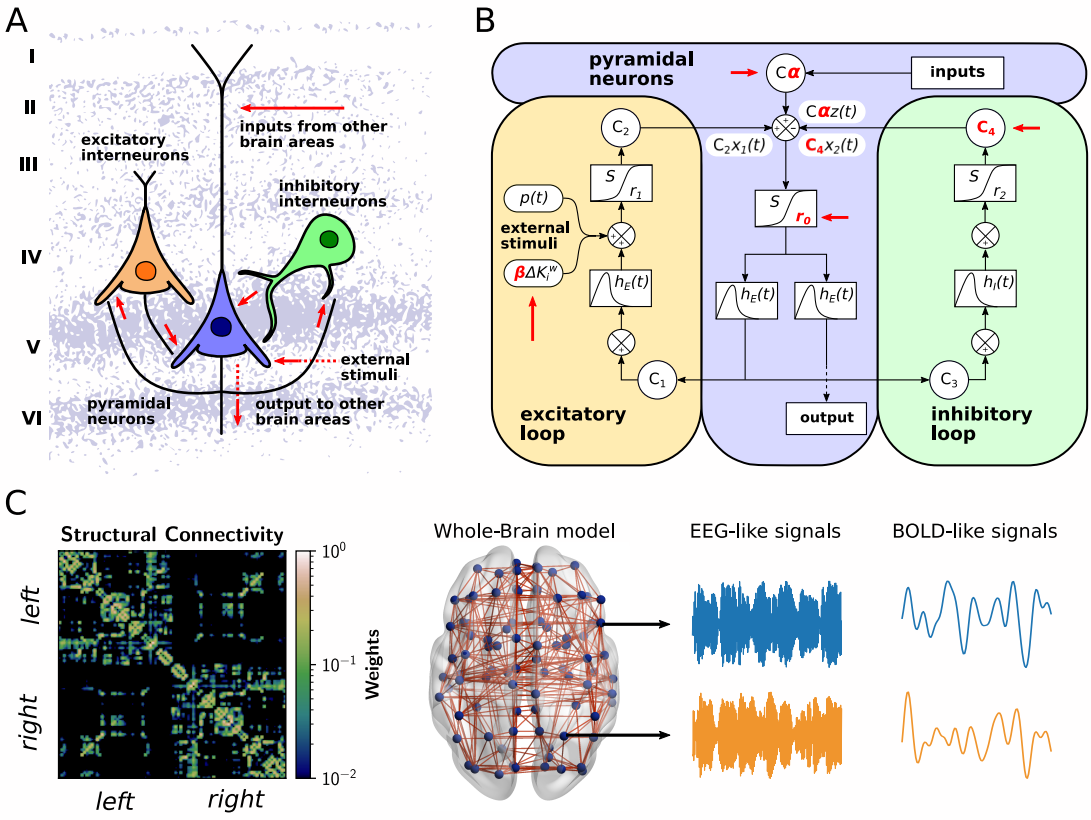

Figure 3.1: Detailed description of the neural mass model. **A)** Simplified scheme of the Jansen & Rit model; it is composed of a population of pyramidal neurons with excitatory and inhibitory feedback mediated by interneurons. **B)** Constants C_i connect each population. The outputs are transformed from average pulse density to average postsynaptic membrane potential by an excitatory (inhibitory) impulse response function $h_E(t)$ ($h_I(t)$). Then, a sigmoid function S performs the inverse operation. Pyramidal neurons project to distant brain areas and receive both uncorrelated Gaussian-distributed inputs $p(t)$ and inputs from other regions $z(t)$, scaled by a global coupling parameter α. For simulating the task, a term ΔK_i^w modifies heterogeneously the background input $p(t)$ to pyramidal neurons. The slope of the input-output function of pyramidal neurons, r_0, was used to model the influence of noradrenergic system. Cholinergic system was modelled by decreasing α and C_4. In every chapter, I only modified the parameters highlighted by the red arrows. **C)** Each node represents a brain region, whose dynamics are ruled by the Jansen & Rit equations. The structural connectivity matrix is the map of the connections (and their weight in the color bar) between brain regions (row and columns of the matrix). For each region, the model produces both EEG-like and BOLD-like signals. The brain figure in C) was obtained using the BrainNet Viewer. (Xia et al., 2013). The background figure in A) was adapted from Schmolesky (2016) with permission.

3.1.2 Neuromodulation

The effects of the cholinergic system were modeled by the parameters α and C_4. The parameter α corresponds to the global coupling of the model, and controls the long-rage pyramidal to

Parameter	Value	Unit
A	3.25	mV
B	22	mV
a	100	s^{-1}
b	100	s^{-1}
$\bar{a}$	50	s^{-1}
C	135	Unitless
C_1	1C	Unitless
C_2	0.8C	Unitless
C_3	0.25C	Unitless
C_4	$\in [0.3C, 0.9C]$	Unitless
α	$\in [0, 1]$	Unitless
r_0	$\in [0, 1]$	mV^{-1}
r_1	0.56	mV^{-1}
r_2	0.56	mV^{-1}
ζ_{max}	5	s^{-1}
ν_{th}	6	mV
μ	2 or 4.8	mV
σ	1	mV
β	$\in [-0.5, 2.5]$	Unitless
Simulation time	600 or 1200	s
Integration step	1	ms

Table 3.2: Parameters employed in the Jansen & Rit model. Some of the parameters are fixed across all simulations.

pyramidal neuron coupling through the M matrix. Meanwhile, C_4 controls the local feedback inhibition onto pyramidal neurons. To simulate the effects of acetylcholine, I decreased the value of α and C_4 independently. This mimic the effect, in a simpler way, of nicotinic and muscarinic acetylcholine receptors on long-range connectivity (Kimura, 2000; Picciotto et al., 2012; Poorthuis et al., 2013) and feedback inhibition (Kruglikov and Rudy, 2008; Picciotto et al., 2012; Askew et al., 2019; Zerbi et al., 2019). The effects of the noradrenergic system, designated as filter gain, were simulated controlling the parameter r_0, which represents the sigmoid function slope of the pyramidal population, and increases the signal-to-noise ratio of pyramidal cells (Servan-Schreiber et al., 1990; Thiele and Bellgrove, 2018).

3.1.3 Frequency and Power

The oscillation frequency ω_i of each node i was computed as the peak frequency of its power spectral density function denoted $PSD(\omega)$. This function was calculated using the Welch's method (Welch, 1967), with 4 s time windows overlapped by 50%.

Using the $PSD(\omega)$ function, the absolute power in the common EEG frequency bands was computed by integration within the frequency range of interest: delta (0.5 - 4 Hz), theta (4 - 8 Hz), alpha (8 - 12 Hz) and broadband (0.5 - 12 Hz). Relative power was calculated as the ratio between the band absolute power and the broadband absolute power.

3.1.4 Synchrony

As a measure of global synchronization I calculated the Kuramoto order parameter $R(t)$ (Acebrón et al., 2005) of the EEG-like signals $\nu(t)$ derived from the Jansen & Rit model. The raw signals were filtered with a 3rd order Bessel band-pass filter using their frequency of maximum power (usually between 4 and 10 Hz) ± 3 Hz. Then, the instantaneous phase $\phi(t)$ was obtained with the Hilbert transform. The global phase synchrony is computed as:

$$\bar{R} = \left\langle \left| \langle e^{j\phi_i(t)} \rangle_N \right| \right\rangle_t$$

where $\phi_i(t)$ is the phase of the oscillator i over time, $j = \sqrt{-1}$ the imaginary unit, $|\bullet|$ denotes the module, $\langle\rangle_N$ denotes the average over all nodes, and $\langle\rangle_t$ the average over time. A value of $\bar{R}$ equal to 1 indicates perfect in-phase synchronization of all the set N of oscillators, while a value equal to 0 indicates total asynchrony.

3.1.5 Hemodynamic Model

I used the firing rates $\zeta_i(t)$ (3.7)to simulate BOLD-like signals using a generalized hemodynamic model presented in Stephan et al. (2007). In this model, an increment in the firing rate $\zeta_i(t)$

triggers a vasodilatory response s_i, producing blood inflow f_i, changes in the blood volume v_i and deoxyhemoglobin content q_i. The corresponding system of differential equations is

$$\begin{aligned}
\dot{s}_i(t) =& \zeta_i(t) - \frac{s_i(t)}{\tau_s} - \frac{f_i(t) - 1}{\tau_f} \\
\dot{f}_i(t) =& s_i(t) \\
\dot{v}_i(t) =& \frac{f_i(t) - v_i(t)^{1/\kappa}}{\tau_v} \\
\dot{q}_i(t) =& \frac{\frac{f_i(t)(1-(1-E_0)^{1/f_i(t)})}{E_0} - \frac{q_i(t) v_i(t)^{1/\kappa}}{v_i(t)}}{\tau_q},
\end{aligned} \tag{3.8}$$

where $\tau_s = 0.65$, $\tau_f = 0.41$, $\tau_v = 0.98$, $\tau_q = 0.98$ represent the time constants for the signal decay, blood inflow, blood volume and deoxyhemoglobin content, respectively. The stiffness constant (resistance of the veins to blood flow) is given by κ, and the resting-state oxygen extraction rate by E_0. I used $\kappa = 0.32$, $E_0 = 0.4$. The BOLD-like signal of node i, denoted $B_i(t)$, is a non-linear function of $q_i(t)$ and $v_i(t)$

$$B_i(t) = V_0 \left[k_1 \left(1 - q_i(t)\right) + k_2 \left(1 - \frac{q_i(t)}{v_i(t)}\right) + k_3 \left(1 - v_i(t)\right) \right], \tag{3.9}$$

where $V_0 = 0.04$ represents the fraction of venous blood (deoxygenated) in resting-state, and $k_1 = 2.77$, $k_2 = 0.2$, $k_3 = 0.5$ are kinetic constants. Parameters values can be consulted in Table 3.

The system of differential equations (3.8) was solved using the Euler method with an integration step of 10 ms. The signals were band-pass filtered between 0.01 and 0.1 Hz with a 3rd order Bessel filter. These BOLD-like signals were used to build the (FC) matrices using pairwise Pearson correlations.

The implemented codes can be found in `https://github.com/vandal-uv/Structural_Neuromod_2021`.

3.1.6 Functional Segregation and Integration

Starting from the FC matrices, I first applied a proportional threshold to remove possible spurious connectivity values (Rubinov and Sporns, 2010). Then, FC matrices were binarized and graph measures were computed. Specifically, I calculated the binary global efficiency and transitivity,

Parameter	Value	Unit
τ_s	0.65	s
τ_f	0.41	s
τ_v	0.98	s
τ_q	0.98	s
κ	0.32	Unitless
E_0	0.4	Unitless
V_0	0.04	Unitless
k_1	2.27	Unitless
k_2	0.2	Unitless
k_3	0.5	Unitless

Table 3.3: Parameters employed in the hemodynamic model. Parameters are fixed across all simulations.

metrics related integration and segregation, respectively (Rubinov and Sporns, 2010). As an example, metrics were presented in Fig. 3.2.

Global efficiency is based in paths, and was defined as (Latora and Marchiori, 2001)

$$E = \frac{1}{n}\sum_{i}^{n} E_i = \frac{1}{n}\sum_{i}^{n} \frac{\sum_{j\neq i}^{n} d_{ij}^{-1}}{n-1} \tag{3.10}$$

with E_i as the nodal efficiency, $n = 90$ the total number of nodes, and d_{ij} the shortest path that connects two nodes ij. The global efficiency is bounded between 0 and 1. Higher values are expected to be found in very integrated networks, where nodes can easily reach each other; values near 0 means the opposite. Transitivity is based on the count of the triangular motifs of the network, and it was computed as (Newman, 2003)

$$T = \frac{\sum_{i}^{n} 2t_i}{\sum_{i}^{n} k_i(k_i-1)} \tag{3.11}$$

where t_i corresponds to the number of triangles around the node i, and k_i the node degree. The first one is defined as

$$t_i = \frac{1}{2}\sum_{j\neq i}^{n}\sum_{h\neq j, h\neq i}^{n} a_{ij}a_{ih}a_{jh} \tag{3.12}$$

with $a_{ij} = 1$ if two nodes ij are connected in the graph, and 0 otherwise. Transitivity captures the degree of local (short range) interactions between nodes and, in more common words, counts "in to what extent my friends are also friends between them". Higher values are expected from segregated networks, and 0 the opposite (e.g., completely random networks).

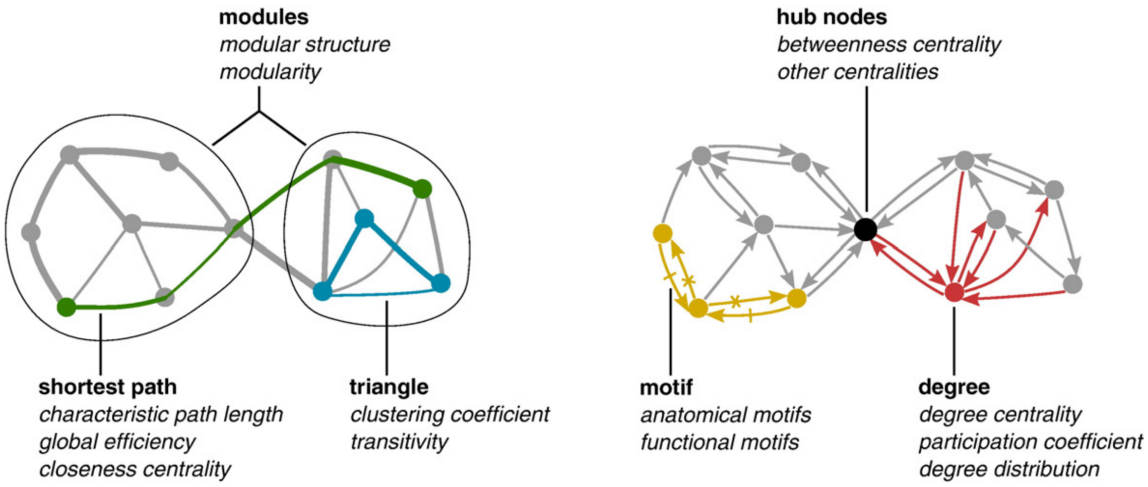

Figure 3.2: Common measures of network topology. Classical integration measures are based on shortest paths (green line). The basic segregation measures consisted in the count of the network's triangular motifs (in blue), or in detecting the so-called network communities or modules (circles around nodes). Within the degree-based metrics (red), the participation coefficient is considered a measure of intergration. Hub nodes (black) are identified using centrality measures. Anatomical motifs are depicted in yellow. Figure taken from Rubinov and Sporns (2010).

I also calculated other two measures of integration and segregation: the participation coefficient PC and modularity Q, respectively, both based on the detection of the network's communities (Rubinov and Sporns, 2010). The detection of so-called communities or network modules in the thresholded FC matrix, was based on Louvain's algorithm (Newman, 2006; Blondel et al., 2008). The algorithm assigns a module to each node in a way that maximizes the modularity (3.13). I used the binary version of the modularity (Newman, 2004) defined as

$$Q = \frac{1}{l} \sum_{i,j \in N} \left[a_{ij} - \frac{k_i k_j}{l} \right] \delta_{m_i, m_j} \tag{3.13}$$

where, l is the total number of links of the network, m_i (m_j) the module of the node i (j). The Kronecker delta δ_{m_i,m_j} is equal to 1 when $m_i = m_j$ (that is, when two nodes belong to the same module), and 0 otherwise. Because Louvain's algorithm is stochastic, I employed the consensus clustering algorithm (Lancichinetti and Fortunato, 2012). Louvain's algorithm was run 200 times with the resolution parameter set to 1.0 (this parameter controls the size of the detected modules; larger values of this parameter allows the detection of smaller modules). Then, I built an agreement matrix G, in which an entry G_{ij} indicates the proportion of partitions in which the pairs of nodes (i, j) share the same module (so, the entries of G are bounded between 0 and 1). Then, I applied an absolute threshold of 0.5 to the matrix G, and ran again Louvain's algorithm 200 times using G

as input, producing a new consensus matrix G'. This last step was repeated until convergence to an unique partition.

Finally, I computed the binary version of the participation coefficient (Guimera and Amaral, 2005). This metric quantifies, for each individual node, the strength of between-module connections respect to the within-module connections, and is defined as

$$\langle PC \rangle_N = \frac{1}{n} \sum_{i \in N} PC_i = \frac{1}{n} \sum_{i \in N} \left(1 - \sum_{m \in \mathcal{M}} \left(\frac{k_i(m)}{k_i} \right)^2 \right)$$

where PC_i is the participation coefficient for the node i, and $\langle PC \rangle_N$ is the average across nodes.

To avoid the arbitrariness of choosing a single proportional threshold, I used a range of thresholds from 5 to 20% with linear increments of 1%. I reported the area under the curve (AUC) of each graph metric as a function of the threshold (Ginestet et al., 2011).

Another issue regarding network analysis in FC is related to the influence of overall FC (the strength of the FC matrix) on functional network topology (van den Heuvel et al., 2017). When overall FC is low, the contrast between true correlations and spurious correlations becomes less marked. In consequence some of these spurious connections –also random placed within the FC matrix– might be included after FC thresholding, producing an artificial increment of functional integration. To divorce the effect of overall FC from topology, I regressed out the overall FC from each graph metric as suggested by van den Heuvel et al. (2017). Regression was done combining the subjects (or seeds) in all conditions (placebo and nicotine in both RS and task). A linear regression was performed (overall FC vs network metric), and the slope was used to regress out the Overall FC. I reported the corrected graph metrics.

The graph analysis was performed using the Brain Connectivity Toolbox for Python (`https://github.com/fiuneuro/brainconn`) (Rubinov and Sporns, 2010).

3.1.7 Functional Connectivity Dynamics

To test the hypothesis that dynamical variability peaks on the critical boundary, I performed a FCD analysis over the filtered BOLD-like signals. The FCD matrix captures the evolution of FCs patterns and, consequently, the dynamical richness of the network (Hansen et al., 2015; Cabral

et al., 2017a). I used the sliding window approach (Hansen et al., 2015; Orio et al., 2018) depicted in the Fig. 4.6. Window length was set to 100 s with a displacement of 2 s between consecutive windows (Fig. 4.6A). The length was chosen on the basis of the lower limit of the band-pass filter (0.01 Hz), in order to minimize spurious correlations (Leonardi and Van De Ville, 2015). For each window, a FC matrix was calculated from the pairwise Pearson correlations of BOLD-like signals (neglecting negative values), thus I obtained 251 weighted and undirected FCs matrices from the 600 s simulated BOLD-like signals (Fig. 4.6B).

The upper triangle of each FC matrix is unfolded to make a vector, and the FCD is built by calculating the Clarkson angular distance $\lambda(x,y) = \frac{1}{\sqrt{2}} \left|\left| \frac{x}{||x||} - \frac{y}{||y||} \right|\right|$ (Clarkson, 1936) between each pair of FCs (Fig. 4.6C)

$$FCD_{ij} = \lambda(FC(t_i), FC(t_j))$$

The variance of the values in the upper triangle of the FCD, with an offset of $\tau = 100$ s from the diagonal (i.e., the variance of the histograms of Fig. 4.6D), is taken as a measure of dynamical richness (Orio et al., 2018).

The speed of the FCD was measured as described by Battaglia et al. (2020). I computed the histogram of FCD values through a straight line from FCD$(\tau, 0)$ to FCD$(t_{max}, t_{max} - \tau)$, with t_{max} as the total time-length of the signals and $\tau = 100$ s. The median of the histogram distribution corresponded to the typical FCD speed d_{typ}. Values closer to 1 indicate a constant switching of states, and values closer to 0 correspond to stable FC patterns.

Codes for FCD can be obtained in `https://github.com/vandal-uv/Structural_Neuromod_2021`.

3.1.8 Statistical Comparison

All pairwise comparisons, such as overall FC and and network metrics, were performed with nonparametric permutation tests. These tests are suitable when using small sample sizes, and do not require any assumptions about normality (Nichols and Holmes, 2002). The real difference between groups (computed as the mean difference) was compared with the distribution obtained

from 10000 random surrogates; they were acquired by randomly reassigning the measures between groups (e.g., placebo and nicotine). I reported the p values, and results were considered as statistically significant for p values < 0.05. In addition, statistical relationships were measured using Pearson and Spearman correlations.

3.2 SPECIFIC METHODS 1

3.2.1 Simulations

I ran simulations to generate the equivalent of 11 min real-time recordings, discarding the first 60 s. 10 random seeds were used, which controlled the initial conditions and the stochasticity of the simulations. To simulate the influence of the cholinergic system alone, I swept the parameters $\alpha \in [0, 0.5]$ and $C4 \in [0.3C, 0.6C]$, for a fixed $r_0 = 0.56$. Then, to include the effect of the noradrenergic system, I swept $\alpha \in [0, 1]$ and $r_0 \in [0, 1]$, fixing $C_4 = 0.5C$. For this set of simulations I employed $\mu = 2$ and $\sigma = 1$. All the simulations were implemented in Python, and the codes are freely available at `https://github.com/vandal-uv/Neuromod2020`.

3.2.2 Cartographic Profile

To analyze, in the simulations, how FC brain network topology changes across time, I used again the sliding windows method described in **Functional Connectivity Dynamics**. Within each window I computed the FC matrices, and then calculated the binary versions of the global efficiency, E, and transitivity, T. The resulting time series corresponded to the time-dependent topological features of the FC brain networks. Similar to Shine et al. (2016) and Shine et al. (2018a), I computed the standard deviation of $E(t)$ and $T(t)$ (time courses for global efficiency and transitivity), as measures of temporal topological variability.

3.3 SPECIFIC METHODS 2

3.3.1 Subjects and Nicotine Administration

The study involves a re-analysis of a previously published dataset (Gießing et al., 2013). Eighteen healthy right-handed cigarette smokers were studied in a double-blind, randomized, placebo-controlled, crossover design in which once nicotine was delivered in the form of a 4 mg nicotine polacrilex gum (Nicorette, McNeil AB) and once a placebo in the form of a taste- and size-matched gum. The gum was chewed for 30 minutes; then the scanning started immediately. Subjects were asked to refrain from smoking 2 hours before the experiment.

3.3.2 Paradigm and Task

The placebo and nicotine sessions were separated by at least 2 weeks, and each session was divided into different time periods in which resting-state oscillations or task activations were measured using fMRI (Fig. 3.3A). Three resting state-blocks comprising 256, 256, and 512 scans were measured alternately with two task blocks of 339 scans. During the task blocks, participants performed a reversed version of the continuous performance test measuring processes related to attention and vigilance (Conners, 1994) (Fig. 3.3B). During resting-state periods, participants were instructed to lie within the scanner, to keep their eyes open and to attend to a centrally presented visual stimulus.

3.3.3 fMRI Data Acquisition

Scanning was performed with a Siemens MAGNETOM Sonata MRI system (1.5 T). 1729 T2*-weighted echo-planar images with BOLD contrast were measured with a repetition time of 1.5 s and echo time of 50 ms. Detailed information on the investigated sample, nicotine administration,

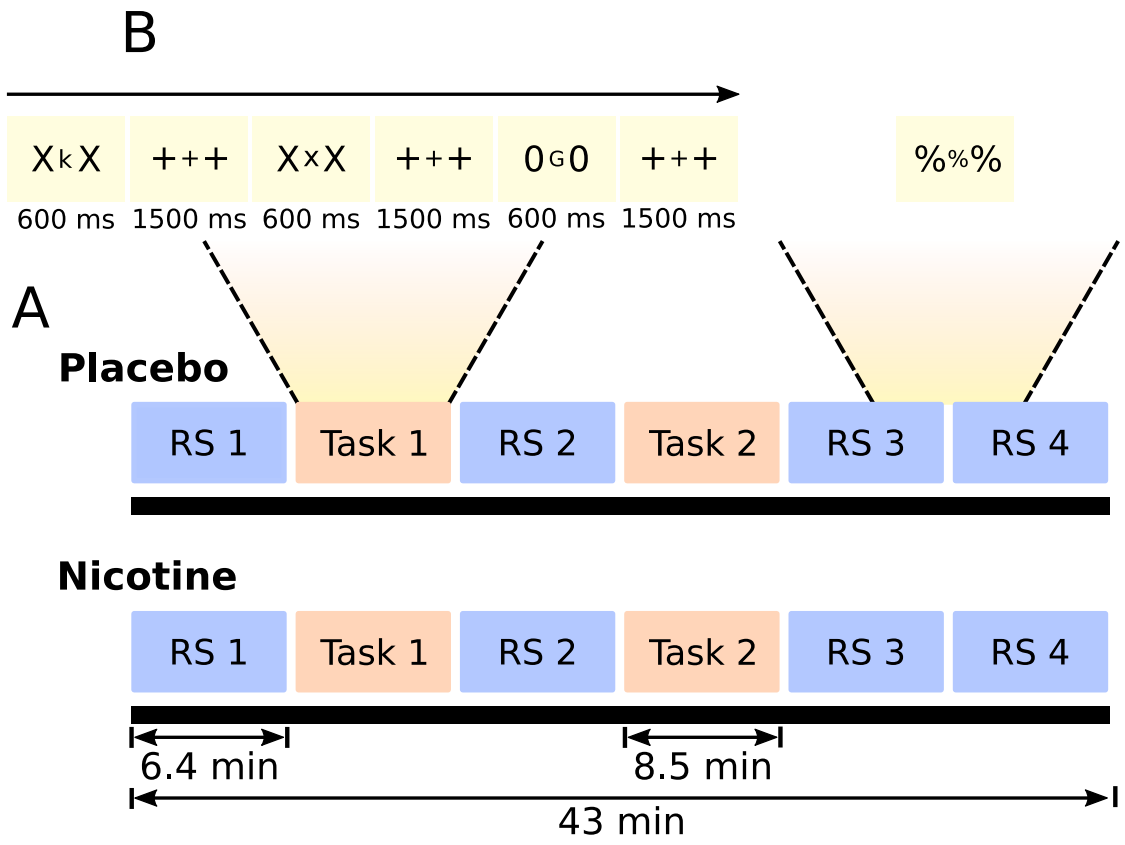

Figure 3.3: Paradigm and task. A) fMRI BOLD recordings were taken in several and consecutive RS and task blocks. Two conditions were considered, placebo and nicotine, separated by at least two weeks. RS and task blocks had a duration of 6.4 and 8.5 minutes, respectively, for a total scan time of 43 min. **B)** Reversed version of the continuous performance test (Go/No-Go task). During RS periods, subjects kept their eyes open and looked at a centrally presented stimulus (%%%). Figure adapted from Gießing et al. (2013).

the paradigm, and the fMRI data acquisition can be found in Gießing et al. (2013).

3.3.4 Preprocessing and Time Series Analysis

The brain scans were corrected for head motions by spatial realignment, corrected for slice timing offsets, co-registered with the subjects' anatomical images, spatially normalized to standard stereotaxic MNI space (Montreal Neurological Institute; `http://www.mni.mcgill.ca/`), and detrended. Next, nuisance covariates associated with the six linear head movements parameters were regressed out from the data (Hallquist et al., 2013). To remove the possible effects of small and transient head movements on FC, the framewise displacements (FD) and the root mean

square of voxelwise percentage signal change (DVARS) of the preprocessed time series were quantified. In accordance with previously reported methods for "scrubbing" (Power et al., 2012), all frames of data with FD $>$ 0.5 mm and/or DVARS $>$ 0.5% were removed. The fMRI BOLD time series were band-pass filtered between 0.01 and 0.1 Hz with a 3rd order Bessel filter, and then used to build the FC matrices –employing pairwise Pearson correlations– from which the subsequent analysis of functional network properties was performed.

Average volumetric PET images were collected for 3 different cholinergic receptors and transporters across 5 studies with open-dataset (Hansen et al., 2021), which include nicotinic $\alpha_4\beta_2$ (Hillmer et al., 2016), muscarinic M_1 (Naganawa et al., 2021), and the vesicular acetylcholine transporter (VAChT) (Hansen et al., 2021; Bedard et al., 2019; Aghourian et al., 2017).

3.3.5 Nicotine and Task modeling

I ran simulations to generate the equivalent of 21 min real-time recordings, discarding the first 60 s. 100 random seeds were used, which controlled the initial conditions and the stochasticity of the simulations. The model was implemented in Python and can be obtained in `https://github.com/vandal-uv/Nicotine-Whole-Brain`.

To simulate the effects of nicotine, I decreased the value of the global coupling α, and the inhibitory-to-pyramidal neurons connectivity constant C_4, as mentioned previously in **Neuromodulation** section. To simplify the fitting, I defined C_4 as a linear function of global coupling: $C_4 = (0.3 + 0.6\alpha)C$. For simulating the task condition, I changed the input slope β. This parameter scales the vector ΔK_i^w, which represents the averaged empirical difference between the nodal strength in the first RS and task blocks (placebo condition). A change in β can increase or decrease the mean of the background input that arrives at brain regions, depending on the entries of ΔK_i^w, producing a heterogeneous stimulation as an effect of the task.

For this set of simulations I employed $\mu = 4.8$ and $\sigma = 1$. Increasing the value of μ, in comparison with the employed in the **Exploring Parameter Space** section, increases the power of alpha oscillations that can be observed in the model.

3.3.6 Model Fitting

I used the averaged empirical FC matrices across subjects as "targets" for model fitting. From the simulated BOLD-like signals, I built the simulated FC matrices with pairwise Pearson correlation. I vectorized the upper triangular of the empirical and simulated FC matrices, and then the vectors were compared using the euclidean distance. A lower distance value corresponded to a better fitting; the aim was to minimize the euclidean distance between empirical and simulated FCs.

Before fitting the model to the empirical fMRI data, I performed an optimization procedure over the human SC matrix M (Deco et al., 2019). I swept the parameter $\alpha \in [0.55, 0.89]$, and chose the value of alpha that better reproduces the features of the empirical FC matrix in the placebo condition - RS block: $\alpha = 0.651$ for a correlation, between matrices, around 0.3. From this point I updated the values of the matrix M iteratively –discarding negative entries– as following

$$M_{ij} = M_{ij} + \epsilon \left(FC_{ij}^{emp} - FC_{ij}^{sim} \right) \tag{3.14}$$

with FC_{ij}^{emp} as the empirical FC matrix in the placebo condition - RS block, FC_{ij}^{sim} the simulated FC matrix at $\alpha = 0.651$, and $\epsilon = 0.01$ the rate of convergence. I used 20 random seeds in each iteration, and computed an averaged FC matrix across random seeds. The results of the optimization are presented in the Fig. 5.5, where the euclidean distance decreases and correlation increases across iterations, indicating an improvement of the fitting. I employed the optimized SC matrix in the subsequent simulations. Thus, the optimized SC matrix was not changed for simulating the effect of both nicotine and task. The codes for SC optimization can be found in `https://github.com/vandal-uv/Nicotine-Whole-Brain`.

To fit the model to the placebo and nicotine conditions - RS block, I swept $\alpha \in [0.6, 0.7]$ in steps of 0.001. Using the value of the placebo condition - RS block ($\alpha = 0.648$), I swept the input slope $\beta \in [-0.5, 2.5]$ in steps of 0.03 for fitting the model to the placebo condition - task block. Then, employing $\beta = 0.58$ I again swept $\alpha \in [0.6, 0.7]$ to fitt the model to the nicotine condition - task block. At the end, I found four α and β values for simulating placebo - RS block ($\alpha = 0.648, \beta = 0$), nicotine - RS block ($\alpha = 0.644, \beta = 0$), placebo - task block ($\alpha = 0.648, \beta = 0.58$), and nicotine - task block ($\alpha = 0.641, \beta = 0.58$).

I informed the model with acetylcholine-related receptors maps obtained by PET (Hillmer et al., 2016; Aghourian et al., 2017; Baldassarri et al., 2018; Bedard et al., 2019; Hansen et al., 2021; Naganawa et al., 2021), to test the possibility of improving the model fitting with the addition of the maps. Specifically, I used the nicotinic $\alpha_4\beta_2$ receptor density map –into AAL90 parcellation– because this was the only one that correlates with the change in nodal FC strength (nicotine - placebo averaged for RS and task blocks, Fig. 5.8A). Also, I compared the original map with random and constant versions of the former. Starting from the placebo condition ($\alpha = 0.648$), I changed the α and C_4 parameters linearly with the receptor's density vectors, obtaining convex curves similar to those observed in the Fig. 5.6. A narrow range of α values were employed: $\Delta\alpha \in [-0.012, 0.010]$ in steps of 0.0003. The quantity $\Delta\alpha$ corresponded to the mean α difference (from placebo) for overall nodes. I calculated the minimal euclidean distance of the curves, and compared the values obtained with the three maps. The better model corresponded to the one with the lower minimal euclidean distance. Before computing the minimal euclidean distance, I performed a polynomial regression (two degrees polynomial) and then I calculated the minimal distance from the fitted curves.

3.3.7 Statistical Dimensionality

As a measure of information-theoretic relevance of functional states, the statistical dimensionality of the neural activity was computed as described in (Litwin-Kumar et al., 2017; Ito et al., 2020). First, FC matrices were built using covariance between the pairs of time series: EEG-like or BOLD-like signals. Then, single value decomposition was used to obtain the eigenvalues of the FC matrices, and the statistical dimensionality corresponded to the number of eigenvalues needed to explain variance greater than some fixed threshold. When more eigenvalues are required, data dimensionality was higher (Ito et al., 2020). A threshold of 50% was employed for both EEG-like and BOLD-like FCs.

3.4 SPECIFIC METHODS 3

3.4.1 Structural Metrics

Macro-scale: to compare different macro-scale features of the connectome I used four connectivity matrices (see Fig. 6.1). The first matrix corresponds to the original human connectome (Human, Fig. 6.1A) (Deco et al., 2018). The second to a degree and strength preserving randomization of the matrix (DSPR, Fig. 6.1B) (Rubinov and Sporns, 2011). The third is a randomization, which only preserves the weight distribution of the original matrix (Random, Fig. 6.1C). The fourth matrix was built setting to 0 all entries of $M_{ij} < 0.05$, and 1 otherwise (Homogeneous, Fig. 6.1D).

Meso-scale: I identified the nodes belonging to the "rich club" sub-network of the graph (Van Den Heuvel and Sporns, 2011). Nodes were ranked according to degree, and then a subgraph was built using a threshold K, retaining the nodes with a degree greater than K. For each K value the weighted rich-club coefficient was computed as (Opsahl et al., 2008)

$$\phi^w(K) = \frac{W_{>K}}{\sum_{l=1}^{E_{>K}} w_l^{rank}} \tag{3.15}$$

where $W_{>K}$ is the sum of the weighted edges of the subgraph of nodes with a degree greater than K, $E_{>K}$ represent the total number of edges of the subgraph, and w_l^{rank} a vector that contains all the weighted edges of the entire network sorted from high to low values. If $\phi^w(K) = 1$ the sum of the weights of the "rich nodes" is maximal. Otherwise, $\phi^w(K) < 1$ indicates the proportion of the weighted edges of the network that are into the sub-network, and then some of the stronger connections were missed when applying the threshold K. The rich club coefficient was normalized in relation to DSPR surrogate graphs.

$$\phi^w_{norm}(K) = \frac{\phi^w(K)}{\phi^w_{rand}(K)} \tag{3.16}$$

being $\phi^w_{norm}(K)$ the normalized rich club coefficient, and $\phi^w_{rand}(K)$ the mean rich club coefficient for a set of 1000 random surrogates graphs. Values of $\phi^w_{norm}(K) > 1$ indicates a rich-club organization, and nodes retained at K are defined as "rich club" nodes (Fig. 6.5A). The nodes that do not belong to the rich club, but are connected with these nodes are called "feeders". The

remaining nodes correspond to “local” nodes (Fig. 6.5B). For a maximum $\phi^w_{norm}(K) = 1.367$ $(p < 0.002)$, I identified 17 “rich club” nodes, 60 feeder nodes and 13 local nodes (Fig. 6.5B). Because the high density of the structural matrix M $(\approx 40\%)$ hindered the discerning of the local nodes from feeders, I identify these nodes applying an absolute threshold of 0.05 to M. I selected this value as the maximum threshold that when applied preserves the fitting of the model to the empirical placebo RS FC matrix (Deco et al., 2018).

The core-periphery organization (Hagmann et al., 2008) was analyzed performing a *s*-core decomposition (Garas et al., 2012; Eidsaa and Almaas, 2013), which identifies the cores of densely interconnected nodes in the network. The method consists in removing recursively a shell of nodes with strength less than s to obtain the network core nodes. The nodes were assigned to a category that corresponded to the maximal s value at which they are still connected to the network (Fig. 6.6A). I defined three categories for different s values: s_1 with 24 nodes $(s < 1.48)$, s_2 with 56 nodes $(1.48 < s < 1.54)$, and s_3 with 10 nodes $(1.54 < s < 1.78)$ (Fig. 6.6B).

Local-scale: I employed three different metrics to characterize individual nodes. Node strength (weighted degree) was computed as

$$K^w_i = \sum_{j \in N, j \neq i} w_{ij}, \tag{3.17}$$

where N is the set of nodes and w_{ij} the weighted edge of the matrix M (Rubinov and Sporns, 2010).

I computed the nodal efficiency as

$$E^w_i = \frac{\sum_{j \in N, j \neq i} (d^w_{ij})^{-1}}{n-1}, \tag{3.18}$$

where d^w_{ij} is the shortest path between the nodes i and j. Nodes with high values of E^w_i are those with a high proportion of short paths with the rest of the nodes of the network (Rubinov and Sporns, 2010). Finally, I calculated the clustering coefficient for each node (Rubinov and Sporns, 2010)

$$C^w_i = \frac{2t^w_i}{k_i(k_i-1)}, \tag{3.19}$$

where t^w_i is the proportion of triangles around the node i, calculated as

$$t^w_i = \frac{1}{2} \sum_{j,h \in N} (w_{ij} w_{ih} w_{jh})^{1/3}. \tag{3.20}$$

A node with a high C_i^w is highly connected with adjacent (local) nodes.

3.4.2 Selective Neuromodulation

Following (Birn et al., 2013), I ran simulations to generate the equivalent of 11 min real-time recordings, discarding the first 60 s. I used 10 random seeds which controlled the initial conditions, the stochasticity of the simulations, and the randomization of connectomes ((if applicable)). I simulated neuronal activity sweeping the parameters $\alpha \in [0, 1]$ and $r_0 \in [0, 1]$, for the macro-scale scenario. In the local and meso-scale scenarios, I swept $r_0 \in [0.33, 1]$ for a subset of nodes, considering a basal value of $r_0 = 0.33$ and a fixed $\alpha = 0.65$. Details are presented below. For this set of simulations I employed $\mu = 2$, $\sigma = 1$ and $C_4 = 0.5C$. The effect of the noradrenergic system was simulated controlling the parameter r_0 (filter gain) (see the **Neuromodulation** section). I analyzed the effect of the noradrenergic neuromodulation in three scenarios:

Macro-scale: noradrenergic neuromodulation was studied in interaction with the cholinergic system, represented by the parameter α. The parameters were the same for all nodes. I changed the features of the connectivity matrix M (Fig. 6.1) to study the combined effect in neural coordination.

Meso-scale: nodes were classified in different categories, either according to the rich club organization (Van Den Heuvel and Sporns, 2011) or *s*-core decomposition of the network (see the **Structural Metrics** section) (Garas et al., 2012; Eidsaa and Almaas, 2013). I incremented r_0 in a subset of 24 nodes belonging to a particular category, and compared the results with the neuromodulation of an equal-length random subset of nodes. Because the categories differ in the number of nodes, a fair comparison must consider subsets of equal size. To achieve that, I complemented the rich club with 7 randomly selected feeder nodes, while the local nodes were complemented with 11 randomly selected feeders. Likewise, I complemented the S_3 category with 14 randomly selected S_2 nodes. From both the "feeders" and S_2 nodes I selected 24 nodes randomly. All subsets consisted of 24 nodes, were generated 10 times with different random seeds and the results averaged.

Local-scale: nodes were sorted using one of three metrics: node strength K_i^w, nodal efficiency E_i^w, or clustering coefficient C_i^w (Rubinov and Sporns, 2010). I neuromodulated – increasing r_0– node by node in increments of three nodes, considering the metric from high to low and vice-versa.

3.4.3 Segregation and Integration

I used the weighted versions of global efficiency, E^w, and modularity, Q^w, as measures of integration and segregation, respectively. Metrics were described in Rubinov and Sporns (2010), and equations are similar to the presented in **Functional Integration and Segregation**, with the difference that the weighted links and degree (the strength) were employed, instead of their binary versions. Metrics were not corrected for overall FC.

Instead of employing an absolute or proportional thresholding, I thresholded the FC matrices using Fourier transform (FT) surrogate data (Lancaster et al., 2018) to avoid the problem of introducing spurious correlations. The FT algorithm uses a phase randomization process to destroy pairwise correlations, preserving the spectral properties of the signals (the surrogates have the same power spectrum as the original data). I generated 500 surrogate time series of the original set of BOLD-like signals, and then built the surrogate sFCs matrices. For each one of the $(n^2 - n)/2$ possible connectivity pairs (with $n = 90$) I fitted a normal distribution of the surrogate values. Using these distributions, I tested the hypothesis that a pairwise correlation is higher than chance (that is, the value is at the right of the surrogate distribution).

To reject the null hypothesis, I selected a p-value equal to 0.05, and corrected for multiple comparisons with the FDR Benjamini-Hochberg procedure (Benjamini and Hochberg, 1995) to decrease the probability of making type I errors (false positives). The entries of the sFC matrix associated with a p-value greater than 0.05 were set to 0. The result is a thresholded, undirected, and weighted (with only positive values) sFC matrix.

3.4.4 Gene Expression Maps

To quantify the expression of some noradrenergic receptor genes in brain regions, I used the microarray expression data of the Allen Human Brain Atlas (Shen et al., 2012). The dataset was processed and normalized employing the Abagen library for Python (`https://github.com/rmarkello/abagen/tree/0.1.`) (Arnatkevicute et al., 2019), and then parcellated using the AAL atlas (Tzourio-Mazoyer et al., 2002). I compared the expression of the ADRA2A, ADRA2C and ADRB1 genes in rich club, feeders and local nodes.

Chapter 4

Results Part One: Cholinergic and Noradrenergic Switching of Functional Network Topology

Computational models for simulating the effects of acetylcholine (Deco et al., 2014; Nghiem et al., 2020; Pfeffer et al., 2021) and noradrenaline (Servan-Schreiber et al., 1990; Aston-Jones and Cohen, 2005; Shine et al., 2018a; Pfeffer et al., 2021) have been proposed. From a more theoretical perspective, a hypothesis suggests that a possible effect of cholinergic and noradrenergic systems is to promote more segregated and integrated functional states, respectively (Shine, 2019). However, the link between the mechanisms proposed, and the changes in functional network topology by neuromodulation is not established yet. Here, I attempted to model the effects of acetylcholine and noradrenaline at the whole-brain level, using a neural mass model capable of simulating neural activity in the faster timescale of EEG. The output of the model is linked to an hemodynamic model to obtain signals having the slower time scale of fMRI BOLD. From the fMRI BOLD-like signals, I quantified functional integration and segregation making use of graph theory tools (Rubinov and Sporns, 2010). Also, I conclude this section with a dynamical analysis based in FCD (Hansen et al., 2015; Cabral et al., 2017a; Orio et al., 2018), inspired in the idea that neuromodulation moves the brain, at rest, from a dynamical rich regime to a more globally integrated or segregated one over time.

4.1 ACETYLCHOLINE PROMOTES FUNCTIONAL SEGREGATION BY CHANGES IN GLOBAL COUPLING AND FEEDBACK INHIBITION

I assessed the effects of the neuromodulatory systems using a whole-brain neural mass model of brain activity. In the model, each node corresponds to a brain area and is represented by a neural mass consisting of three populations (Jansen et al., 1993; Jansen and Rit, 1995): pyramidal

neurons (that reside in cortical column layer V), excitatory interneurons (nearby pyramidal cells which reside in the same layer than the principal pyramidal population), and inhibitory interneurons (Fig. 3.1A-B). The nodes are connected through a weighted and undirected structural connectivity matrix derived from human data (Deco et al., 2018), parcellated in 90 cortical and sub-cortical regions with the automated anatomical labeling (AAL) atlas (Tzourio-Mazoyer et al., 2002) (Fig. 3.1C). Connections between nodes are made by pyramidal neurons, considering that long-range projections are mainly excitatory (Gilbert et al., 1990; McGuire et al., 1991). Using the firing rates of each node as inputs to a generalized hemodynamic model (Stephan et al., 2007), I obtained fMRI BOLD-like signals from which integration and segregation of the resulting FC matrices were calculated.

I first analyzed the isolated effects of cholinergic neuromodulation, by manipulating the global coupling, α, and the feedback inhibition, C_4, parameters. This is done under the hypothesis that one of the effects of acetylcholine, at the whole-brain level, is to decrease the long-range inter-area coupling and the local feedback inhibition (see for example the sections **The Cholinergic System** and **Neuromodulation**). Thus, is it important to remark that an increase in α and C_4 reflects a decrease in the cholinergic tone, and not the opposite. Integration was measured using the global efficiency, E, and participation coefficient, PC. Segregation was computed as transitivity, T, and modularity, Q. The binary versions of metrics were employed, and they were corrected for overall FC (**Functional Integration and Segregation** section).

In Fig. 4.1, integration and segregation of the FC were measured as a function of α and C_4. In the first row the complete parameter space was shown, and in the second row the values following the a diagonal straight line in the parameter space: $C_4/C = (0.3 + 0.6\alpha)$. The vertical red dotted red lines correspond to the point in which the fitting between the empirical and simulated FCs is closest to its best (Fig. 4.2D). That point was chosen to reflect that, for lower values of the parameters α and C_4, the fitting of the model FC to empirical FC was relatively bad. In consequence, the results of analyzing the simulated FC matrices, at the left of the red lines, using network measures might led to incorrect results, for example, higher integration for a completely disconnected network. To the right –and also to the left– of the red lines, functional

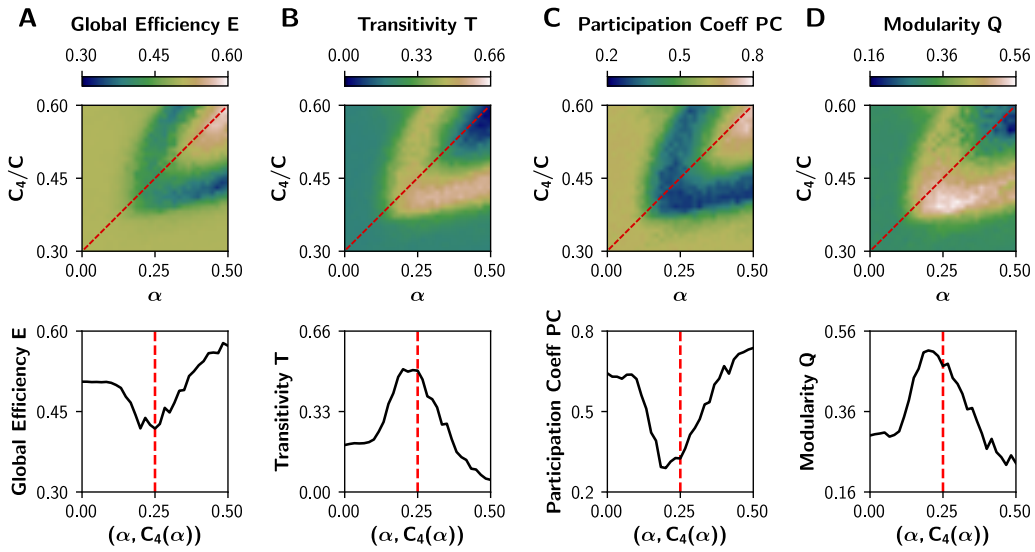

Figure 4.1: Impact of cholinergic neuromodulation on functional network topology. **A)** Global efficiency, E, and **C)** participation coefficient, PC, measures of integration. **B)** Transitivity, T, and **D)** modularity, Q, metrics related to segregation. The binary and corrected graph measures were employed. In the first row the complete (α, C_4) parameter space is plotted. The second row corresponded to the values following a straight line from the left-bottom to the right-top corner. The vertical dotted red lines mark the point where the simulated FCs start to resemble the empirical FC.

integration, measured using E and PC, increases with α and C_4 (Fig. 4.1A,C). Conversely, functional segregation, calculated using T and Q, decreases in the same direction (Fig. 4.1B,D). Thus, a decrease in the cholinergic neuromodulation produces a transition from segregation to integration, at least in the region at the right of the red line. As commented above, although increased integration can be observed at the left of the vertical dotted red line, the increment in integration could be a consequence of having more spurious correlations values, triggered by lower global correlations (van den Heuvel et al., 2017).

Beyond the functional network topology, I computed other informative measures (Fig. 4.2). In a faster timescale –using the EEG-like signals– the increment of α and C_4 increases the global phase synchrony of the network (Fig. 4.2A). Also, the regions of the parameter space associated with higher phase synchrony overlaps with regions with reduced oscillatory frequency (Fig. 4.B); oscillatory frequency drops off from ~ 10 Hz (alpha band) to ~ 5 Hz (theta band). 10 Hz oscillations can be observed when increasing α with low C_4 values (e.g. $C_4 = 0.3C$) Thus, a decrease in the cholinergic tone not only produces a shift from segregation to integration, but also slows down

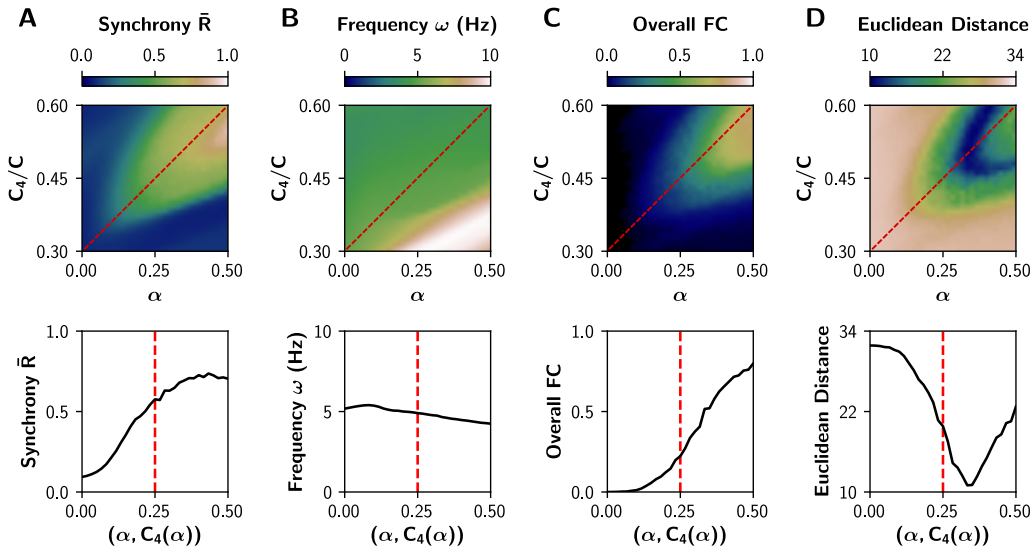

Figure 4.2: Effect of cholinergic neuromodulation on complementary measures. **A)** Global phase synchrony, $\bar{R}$, and **B)** mean oscillatory frequency, ω, both measured from the EEG-like signals. **C)** Global correlations, named overall FC, and **D)** euclidean distance between the simulated and empirical FCs; both metrics were quantified from the fMRI BOLD FCs. In the first row the complete (α, C_4) parameter space is plotted. The second row corresponded to the values following a straight line from the left-bottom to the right-top corner. The vertical dotted red lines mark the point where the simulated FCs start to resemble the empirical FC.

and synchronizes the dynamics in the faster EEG timescale. Back to the slower fMRI BOLD-like signals, an increment in α and C_4 produces the rise of global correlations (the average of the FC matrix, named overall FC), as observed in other computational models (Fig. 4.2C). The fitting to the empirical FC matrix, averaged RS - placebo (Deco et al., 2018), was better (lower euclidean distance) when global correlations were near 0.5.

To show in more detail how the cholinergic system shifts the integration/segregation balance Fig. 4.3 shows some BOLD-like signals and their respective FC matrices. Five tuples of (α, C_4) parameters were chosen, marked with red circles in Fig. 4.3A. Integration and segregation increase and decrease, respectively, following the direction of the diagonal (left to right, bottom to top). The FCs evolve from a completely or nearly disconnected network (Fig. 4.3B-C), to a partially connected network (Fig. 4.3D). That last FC network better resembles the empirical fMRI BOLD FC matrices in RS (Deco et al., 2018). Then, a further increment of both α and C_4 produces a shift to functional integration, where fully connected FC matrices can be appreciated (Fig. 4.3E-F). Thus, the results show that the simulated effect of acetylcholine moves the network from

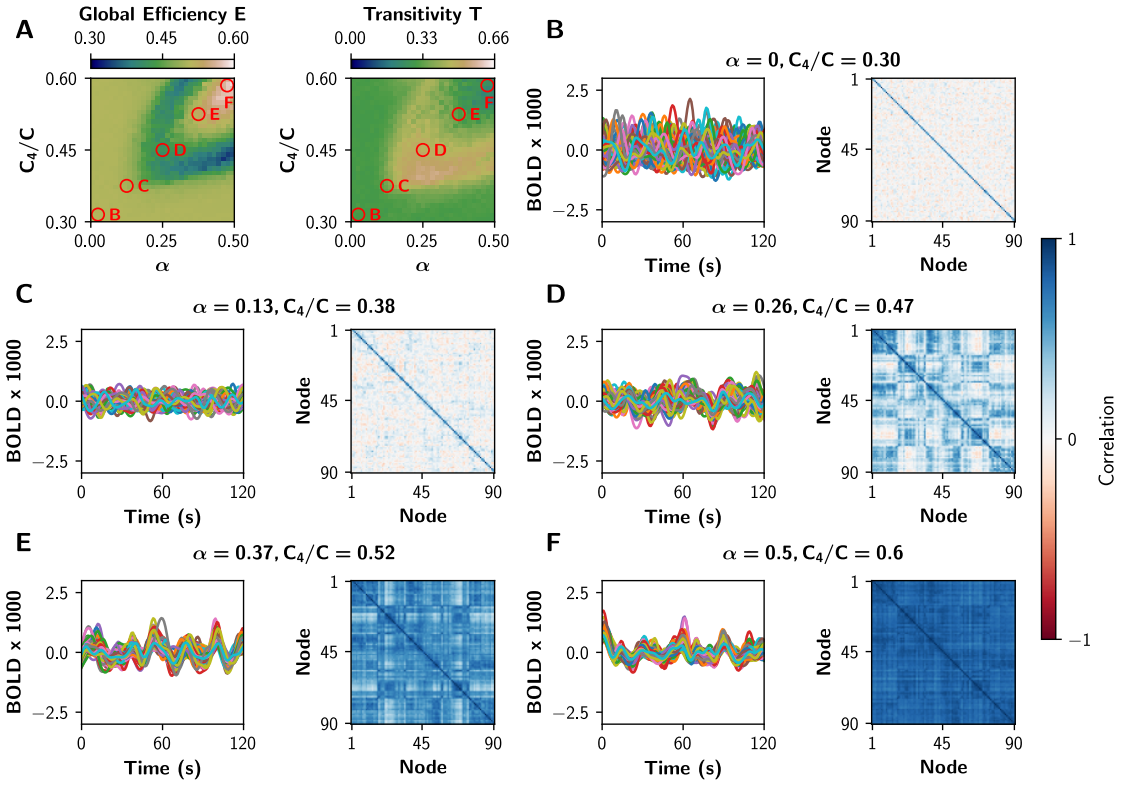

Figure 4.3: fMRI BOLD-like FCs at different values of α and C_4. A) The red circles represent pairs of (α, C_4) values in which different integration/segregation profiles can be observed. **B-F)** BOLD-like signals, and their respective FC matrices, for the (α, C_4) values shown in A). The FC networks evolve from neither integration nor segregation in **B)**, where the nodes are disconnected, to a more segregated FC in **C)**. In **D)** the FC is more likely to be balanced (integration/segreation balance). In **E)** and **F)** the FC network becomes fully integrated. I showed only 120 s of BOLD-like signals, while FC matrices were built with the full-length time series (600 s).

fully connected FCs, to completely disconnected ones. This, in fact, is in line with the effects of acetylcholine on decreasing the inter-area coupling and global correlations (Picciotto et al., 2012; Gießing et al., 2013; Deco et al., 2014; Nghiem et al., 2020; Pfeffer et al., 2021). As commented before, although integration is relatively high in FCs of (Fig. 4.3B-C), the low global correlations of simulated FC matrices' introduces spurious connectivity values which inflates, for example, global efficiency (van den Heuvel et al., 2017).

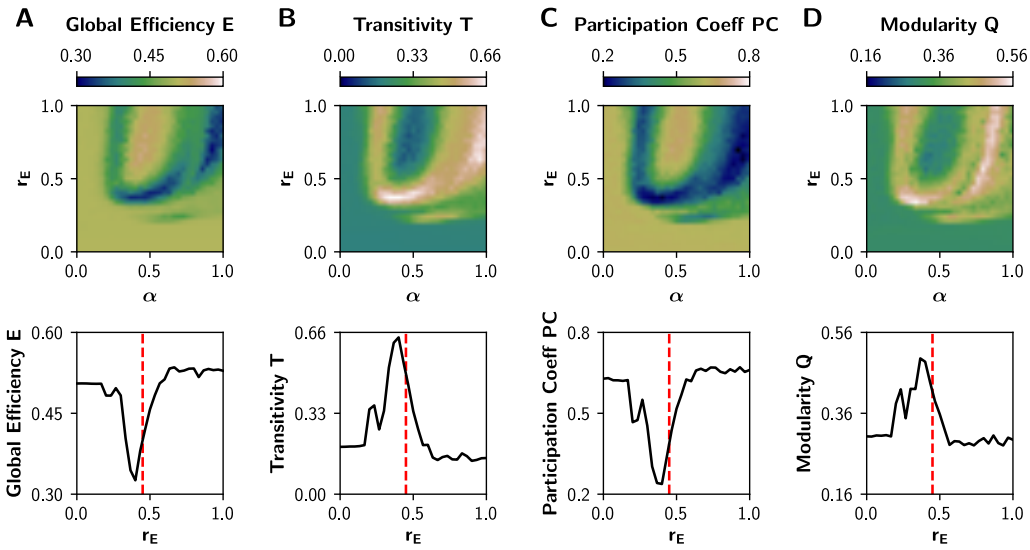

Figure 4.4: Impact of noradrenergic neuromodulation on functional network topology. **A)** Global efficiency, E, and **C)** participation coefficient, PC, measures of integration. **B)** Transitivity, T, and **D)** modularity, Q, metrics related to segregation. I employed the binary and corrected graph measures. In the first row the complete (α, r_0) parameter space is plotted, for a fixed $C_4 = 0.5C$. The second row corresponded to the r_0 values for $\alpha = 0.5$. The vertical dotted red lines mark the point where the simulated FCs start to resemble the empirical FC.

4.2 NORADRENALINE-MEDIATED INCREASE IN FILTER GAIN PRODUCES MORE INTEGRATED FUNCTIONAL STATES

Next, I simulated the effect of the noradrenergic system increasing the slope of the input-output function of pyramidal neurons, denoted here as filter gain (see the sections **The Noradrenergic System** and **Neuromodulation**). As remarked by Shine (2019), it is thought that this system promotes functional integration. An increment in the filter gain parameter, r_0, corresponds to an increase in noradrenergic tone. For this set of simulations, I fixed $C_4 = 0.5C$ and swept both α and r_0 parameters. The results of manipulating r_0 on functional network topology are shown in Fig. 4.4. For intermediate values of α, the increment of r_0 produces an increase of functional integration, computed using E and PC (Fig. 4.4A,C). At the same time, functional segregation, measured using T and Q, decreases with r_0 (Fig. 4.4B,D), Thus, increasing the tone of the noradrenergic system produces, in opposition to the cholinergic system, a transition from functional segregation to integration.

Similar to the results in Fig. 4.2B, the increment in functional integration goes along with

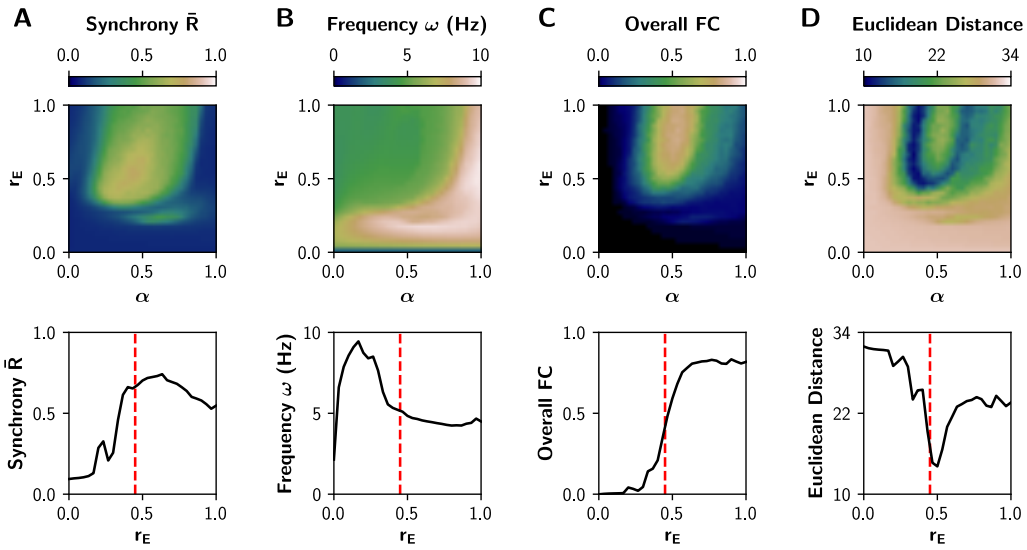

Figure 4.5: Effect of noradrenergic neuromodulation on complementary measures. **A)** Global phase synchrony, $\bar{R}$, and **B)** mean oscillatory frequency, ω, both measured from the EEG-like signals. **C)** Global correlations, named overall FC, and **D)** euclidean distance between the simulated and empirical FCs; both metrics were quantified from the fMRI BOLD FCs. In the first row the complete (α, r_0) parameter space is plotted, for a fixed $C_4 = 0.5C$. The second row corresponded to the r_0 values for $\alpha = 0.5$. The vertical dotted red lines mark the point where the simulated FCs start to resemble the empirical FC.

an increase in the global phase synchrony (EEG-like signals, Fig. 4.5A), a drop off in oscillatory frequency (EEG-like signals, Fig. 4.5B), and a rise in global correlations (BOLD-like signals, Fig. 4.5C). The fitting to the empirical data is better near the transition from segregation to integration (Fig. 4.5D). In the second row of Fig. 4.5, the vertical dotted red lines mark the point (the value of r_0, for a fixed $\alpha = 0.5$), where the simulated and empirical FCs become more similar (better fitting, equivalent to low values of euclidean distance).

At this point, we can observed that the cholinergic and noradrenergic systems, through different mechanisms, move the brain to different regimes of activity: the acetylcholine to a more segregated and asynchronous regime of activity, while noradrenaline to a more integrated and synchronize regime. For intermediate values of the parameters, which reflects the action of neuromodulatory systems, I found that the simulated FCs better resemble the empirical FC (similar to the FC of Fig. 4.3D). There, segregation and integration are balanced (Wang et al., 2021a), and also the brain transits between different FC patterns, which appear and disappear over time. This "dynamic" switching between FC patterns will be studied in the next section.

4.3 NETWORKS' DYNAMIC GET RICHER BETWEEN INTEGRATED AND SEGREGATED BRAIN STATES

As suggested by experimental (Shine et al., 2016, 2018b, 2019) and computational studies (Fukushima and Sporns, 2020; Shine et al., 2018a; Wang et al., 2021a), a shift to a more segregated or integrated functional states decreases the topological variability of the network. Also, near the critical transitions for segregation to integration, network variability and communicability peak (Shine et al., 2018a). I tested this hypothesis performing a FCD analysis (Hansen et al., 2015; Cabral et al., 2017a) on the BOLD-like signals, using the sliding windows approach depicted in Fig. 4.6A-C (Orio et al., 2018). The resulting time vs time FCD matrix describes the concurrence of FC patterns, visualized as square blocks. I computed the standard of the FCD, std(FCD), as a multistability index (Orio et al., 2018), where values greater than 0 indicate the switching between different FC patterns. Additionally, I calculated the FCD speed, d_{typ}, as described by Battaglia et al. (2020), which captures how fast the FC patterns fluctuate over time. Values closer to 1 indicate a recurrent change of diverse FC patterns, and closer to 0 the concurrence of stable and similar states over time. Also, using the same sliding windows method, the time courses of network segregation and integration were characterized by calculating E and T within each sliding window. Similar to Shine et al. (2018a) and Fukushima and Sporns (2020), I computed the standard deviation of $E(t)$ and $T(t)$ (global efficiency and transitivity time courses), as measures of dynamical richness.

In Fig. 4.6D I show a set of FCD matrices obtained at different values of α and r_0 (the parameter space of Fig. 4.4), together with the histograms of their off-diagonal values. Red FCD matrices (with high values) correspond to incoherent states, as the FC continuously evolves in time. On the other hand, a blue FCD matrix (with low values) indicates a fixed FC throughout the simulation. Multistability is higher for green/yellow patchy matrices, because this indicates FC patterns that change and also repeat over time. As can be inferred from observing the FCD distributions, the standard deviation of the values in the histograms –std(FCD)– can be used as a measure of multistability (Orio et al., 2018).

Fig. 4.7 shows how multistability –std(FCD)– and FCD speed, d_{typ}, change in the whole

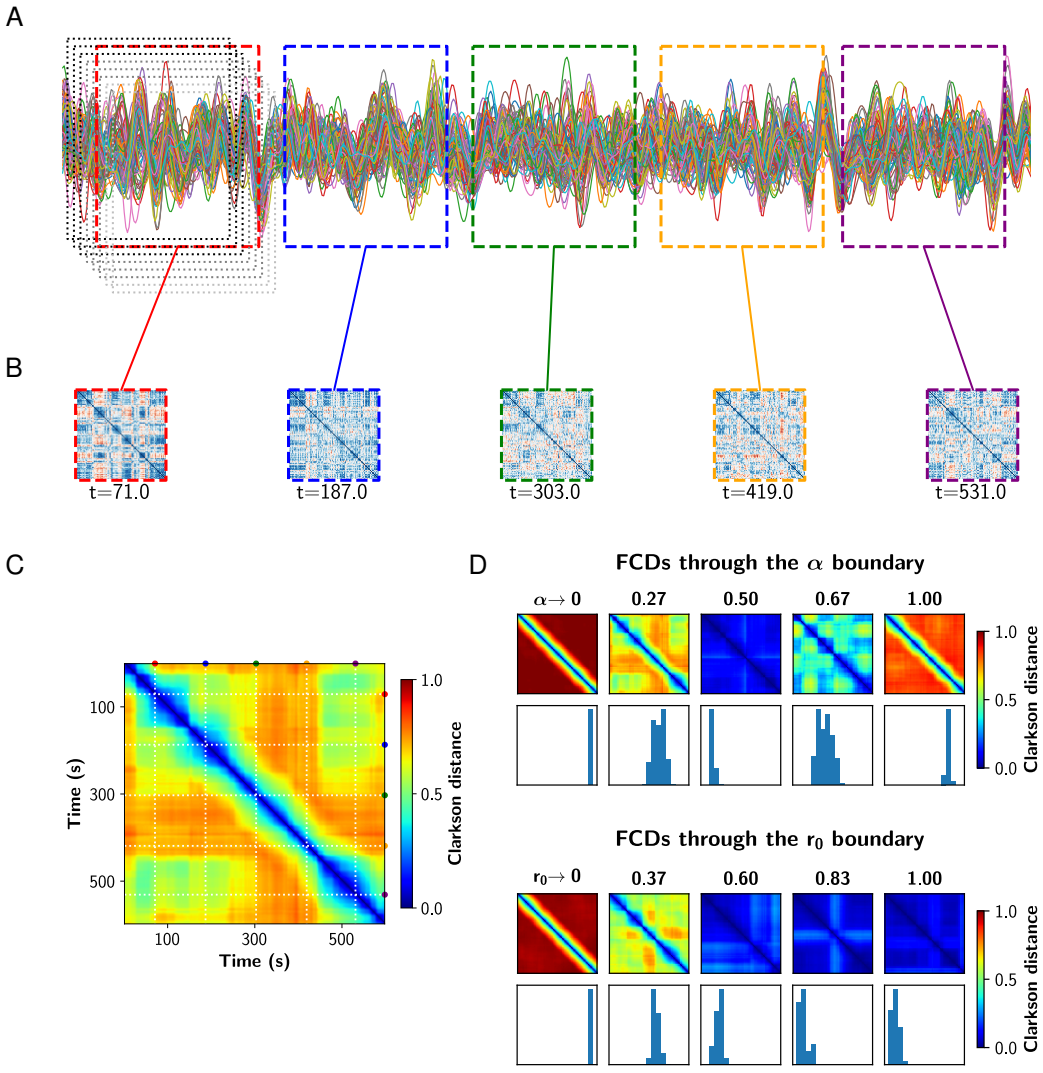

Figure 4.6: Analysis of Functional Connectivity Dynamics.
A) Sample fMRI BOLD time series showing the fixed length and overlapping time windows at the begginging. In color, the time windows corresponding to the FCs shown in B). **B)** FC matrices obtained in the colored time windows. **C)** Functional Connectivity Dynamics (FCD) matrix, where all the FCs obtained were vectorized and then compared against each other using a vector-based distance (Clarkson distance). **D)** FCD matrices in both α ($r_0 = 1$) and r_0 ($\alpha = 0.5$) direction. Below each FCD, a histogram of its upper triangular values is shown. The standard deviation of these values constitutes a measure of multistability.

(α, r_0) space, for $C_4 = 0.5C$. At low levels of both α and r_0, the neuronal activity is constituted mainly by noisy asynchronous signals, conditions associated to low (near 0) values of std(FCD), and with a high d_{typ} (all FC patterns differ from each other, as expected for asynchronous signals) (Fig. 4.7A-B). In the other extreme, for $r_0 > 0.5$ and $\alpha \in [0.4, 0.6]$, values that correspond to the integrated states, std(FCD) is also small and d_{typ} falls close to 0. In consequence, integrated states

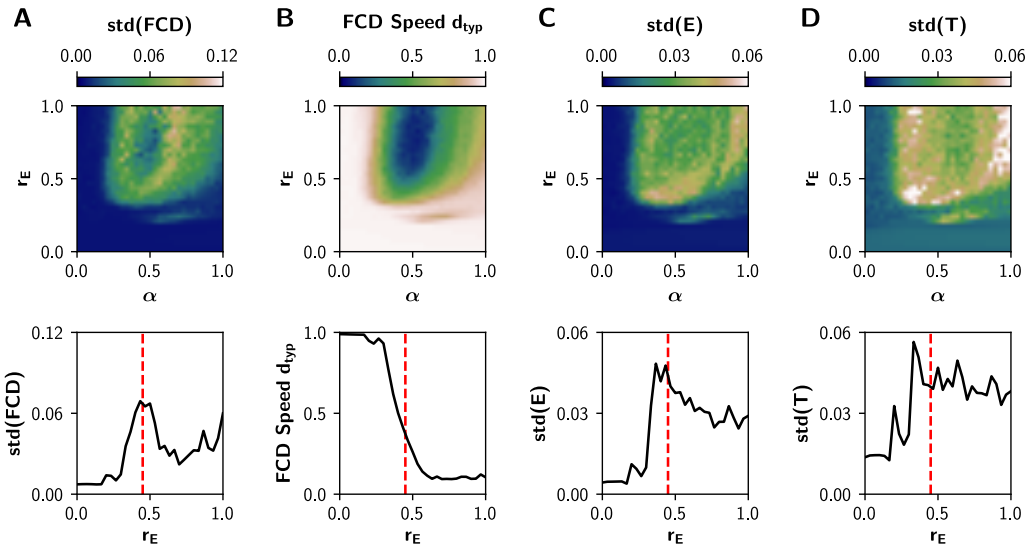

Figure 4.7: Noradrenergic neuromodulation influence on dynamics. **A)** Standard deviation of FCD matrix, std(FCD), which constitutes a measure of multistability. **B)** FCD speed, d_{typ}, that quantifies how "fast" the FC patterns change over time. **C-D** Standard deviation of the global efficiency and transitivity time courses, denoted by $E(t)$ and $T(t)$, respectively. The binary graph measures were employed. In the first row the complete (α, r_0) parameter space is plotted, for a fixed $C_4 = 0.5C$. The second row corresponded to the r_0 values for $\alpha = 0.5$. The vertical dotted red lines mark the point where the simulated FCs start to resemble the empirical FC.

are more stable and less susceptible to network reconfiguration over time. A similar description applies for the network variability, measured as the standard deviation of $E(t)$ and $T(t)$ (Fig. 4.7C-D); both metrics peak near the transition between integration and segregation. The second row of Fig. 4.7 shows, for a fixed $\alpha = 0.5$, the dynamic-related metrics as a function of r_0. The vertical dotted red lines are the same as in Fig. 4.4 and Fig. 4.5. Near the r_0 value marked with the red lines, the standard deviation of the FCD, $E(t)$ and $T(t)$ peaks, meanwhile d_{typ} is near 0.5 (half speed). That r_0 value is near to the minimal euclidean distance in Fig. 4.5D (second row). In consequence, when the model better reproduces the empirical FC matrix in RS, the dynamical richness of the former is at its highest values; the FCD also changes "not so fast, not so slow", allowing the re-appearance and vanish of FC patterns over time. The results point out that, at rest, the brain is within a dynamical rich regime, where integrated and segregated functional states co-exist and interleave.

4.4 SUMMARY

I characterized here the effects of cholinergic and noradrenergic systems on functional network topology. Using a computational model, I showed that acetylcholine moves the *in-silico* whole-brain from functional integration to segregation. Noradrenaline produces the opposite effect. Thus, I proposed here biophysical mechanisms for explaining how those two neuromodulatory systems change FC. Finally, I demonstrated that the switch between integration and segregation, driven by neuromodulation, comes hand in hand with a decrease in the brain's dynamical richness. It gets high in the transition from segregation to integration, where the working point of the brain –in RS conditions– is supposed to be.

Chapter 5

Results Part Two: Whole-Brain Model of Context-Dependent Effects of Cholinergic Neuromodulation on Functional Network Properties

In this section, I verified the results of the computational modeling of cholinergic system, presented in this dissertation. I analyzed fMRI data previously published in Gießing et al. (2013), in both RS and task conditions (Go/No-Go attentional task), under the effects of nicotine. Specifically, I analyzed the FC using tools from graph theory to quantify integration, as global efficiency, and segregation, as transitivity (Rubinov and Sporns, 2010). Then, I built a whole-brain model from Jansen & Rit neural masses (Jansen and Rit, 1995) interconnected using a human connectome. fMRI BOLD-like signals were generated from the firing rates of neural masses (Stephan et al., 2007) and simulated FC matrices were computed. The model was fitted to reproduce the empirical FC matrices in both RS and task under the effect of nicotine or placebo. At the behavioral level, I correlated the performance of the subjects in the Go/No-Go task with metrics computed from the empirical FC matrices. Finally, I verified if the regional expression cholinergic-related receptors and transporters, obtained by positron emission tomography (PET), correlates with regional changes in FC.

5.1 EFFECTS OF NICOTINE ON FUNCTIONAL NETWORK TOPOLOGY ARE CONTEXT-DEPENDENT

I first analyzed the empirical fMRI data (Gießing et al., 2013), under the hypotheses that 1) nicotine promotes functional segregation, and 2) the effects are context-dependent. Recordings were taken from 18 healthy smokers in two different conditions: placebo, and under the effects of nicotine in the form of a 4 mg nicotine polacrilex gum (Nicorette; McNeil AB). Brain areas were defined

using the AAL90 anatomical parcellation, which reduces the brain to 90 cortical and subcortical regions (Tzourio-Mazoyer et al., 2002). BOLD-fMRI was measured in RS and during a Go/No-Go attentional task and the main focus of attention is the functional brain networks captured by the FC matrix.

The main effect of nicotine was to decrease the mean values within the FC matrices (named overall FC, Fig. 5.1A), the effect being stronger in the task block than in RS. Statistically significant differences in overall FC were found for task ($p < 0.05$), but not for RS ($p = 0.196$). Then, the FC matrices were assessed for functional integration and segregation, as described in **Functional Segregation and Integration** section. Segregation was measured by the transitivity T, which is based on the count of the network's triangular motifs; a higher value is related to a network with local neighbors highly interconnected (Rubinov and Sporns, 2010). Integration was quantified by the global efficiency E, which depends on shortest paths; higher values are expected for networks with nodes that can easily reach each other (Rubinov and Sporns, 2010). As overall FC has an effect on the thresholded FC network topology (van den Heuvel et al., 2017), I regressed out the overall FC from graph metrics with a simple linear regression (Fig. 5.2). Throughout this work, I report the corrected graph metrics.

Nicotine produces an increase of E (integration) in RS, and a decrease during the task (Fig. 5.1A). However, results were not statistically significant for either condition ($p = 0.419$ and 0.199, respectively). On the contrary, nicotine increases T (segregation), being this effect significant for the task block ($p < 0.05$), but not for RS ($p = 0.337$) (Fig. 5.1A). The results suggest that nicotine has a pro-segregation effect on the functional brain network topology, explained by the decrease in both overall FC and E and the increase in T. However, these effects were observed only in the task block, pointing out the context-dependent nature of nicotine modulation.

Next, to find a link between functional network topology and behavior (task performance), I analyzed the reaction time (RT) of the Go trials, the errors (percentage of incorrect responses) of the No-Go trials, and the metrics computed from the FC matrices in the task block. As previously reported (Gießing et al., 2013), the main effect of nicotine was to decrease the RT of the subjects during the task ($p < 0.01$) (Fig. 5.1B). Thus, subjects performed better under the effects of

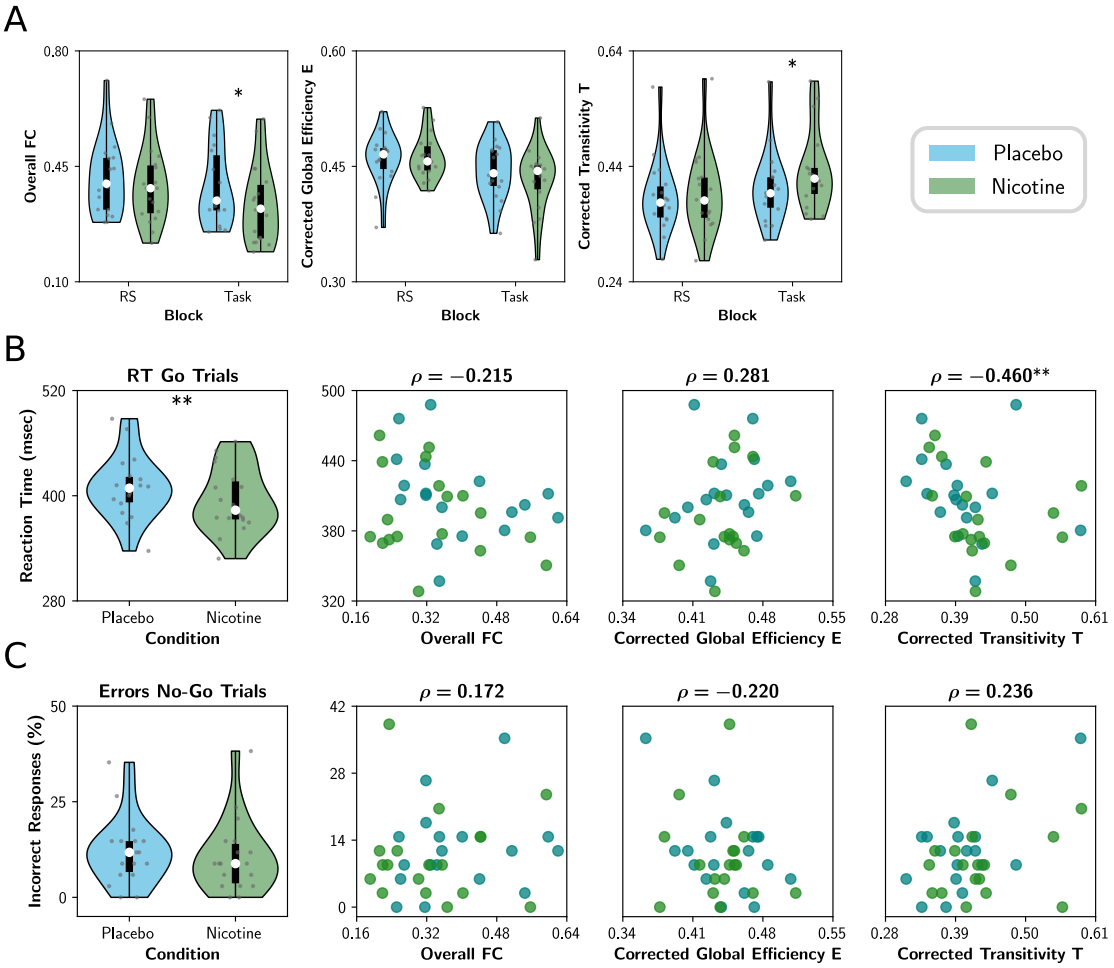

Figure 5.1: Empirical changes in functional connectivity produced by nicotine. A) Effect of nicotine on FC and functional network topology, both in RS and task. Violin plots represent the distributions of points (18 subjects per condition); the box plot is constituted by the median (white circle), the first and third quartiles (box limits), and sample range (whiskers). **B)** Correlation of task FC metrics with the reaction time (RT) of the Go trials. **C)** Correlation of task FC metrics with the percentage of incorrect responses of the No-Go trials. Spearman ρ was used as a correlation measure. Points corresponded to participants (18 subjects per condition). ** : $p < 0.01$, * : $p < 0.05$.

nicotine: a reduction in RT is a signature of enhanced attention (Carlson et al., 1983). When the RT is correlated with FC network metrics, I only found a significant negative correlation with the transitivity T ($p < 0.01$), finding no correlation with the overall FC ($p < 0.197$) and a positive but non-significant correlation with E ($p < 0.01$) (Fig. 5.1B). Regarding the error rate (Fig. 5.1C), there is a trend of nicotine to reduce the percentage of incorrect responses, but the result was not significant ($p = 0.321$). Also, I did not find a correlation between RT with overall FC ($p = 0.314$), E ($p = 0.198$) and T ($p = 0.166$). Thus, subjects that increase their segregation (transitivity) the most,

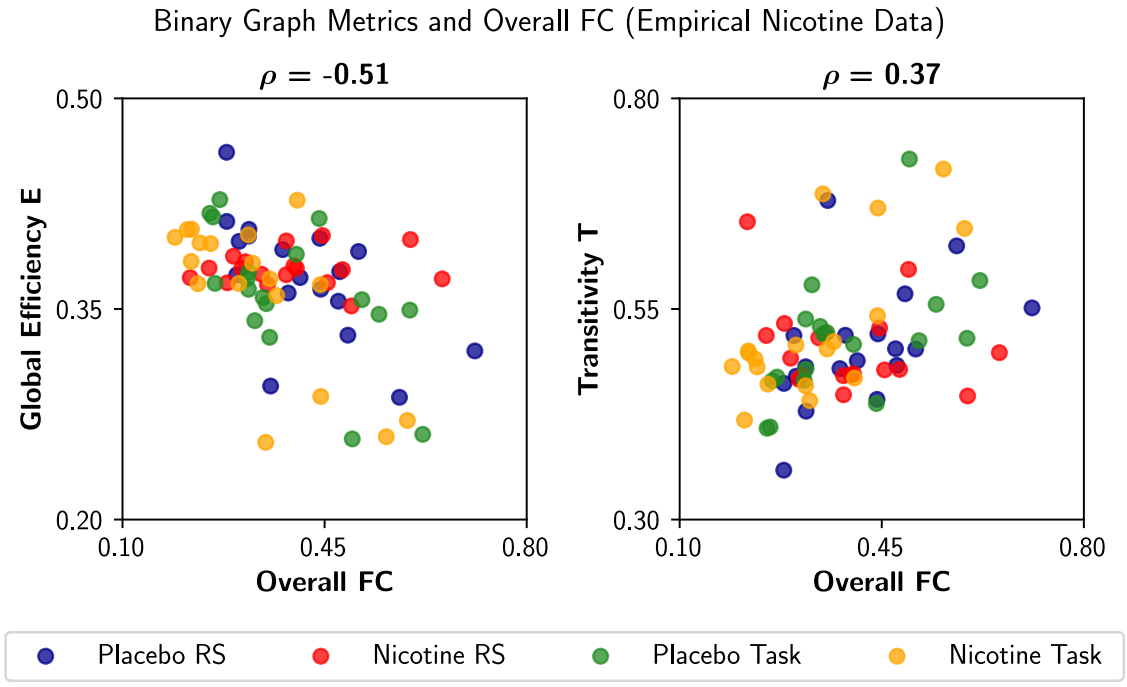

Figure 5.2: Effect of overall FC on functional network metrics (empirical data). Pearson ρ was used as a correlation measure. Points corresponded to participants (18 subjects per condition).

also decrease their RT. From the results it can be inferred that 1) a segregated network is suitable for the task (Go/No-Go), and 2) nicotine improves the reaction time of the subjects promoting a more segregated functional network topology during the task.

To emphasize the context-dependent effect of nicotine, I repeated the network analysis on the three additional RS periods published in Gießing et al. (2013). The first period is the one in (Fig. 5.1A). The remaining periods were analyzed to explore the effect of fatigue on FC: time-on-task increases from RS period 1 to 4 (Fig. 5-3). Nicotine prevented the increase in overall FC triggered by time-on-task. Also, the increase of E and decrease of T caused by nicotine were more pronounced in RS periods 2 to 4, compared to period 1. Thus, in conditions of prolonged time-on-task, nicotine breaks the changes in RS FC triggered by tiredness (Gießing et al., 2013). However, for the remaining analysis I will include only the first RS period, because considering the effects of fatigue in the computational model falls beyond the scope of my work.

Finally, I verified if the effects of the functional network topology on performance are specific of the task, I repeated the previous analysis using the metrics of the RS block (Fig. 5-4). I did not find a correlation between RT and errors with neither overall FC, E, nor T ($p > 0.380$ for all cases).

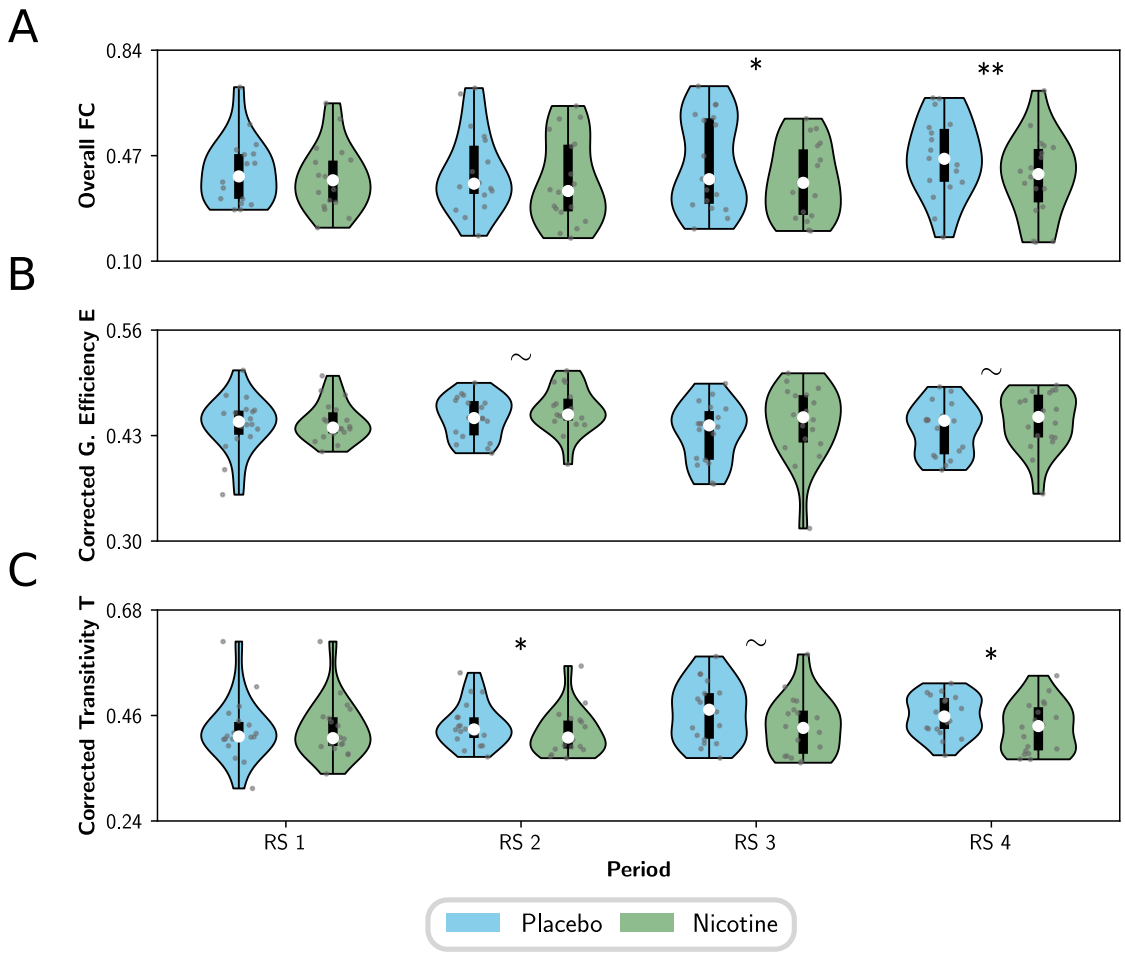

Figure 5.3: Empirical changes in functional connectivity across RS periods. **A)** Global correlations (overall FC); **B)** corrected global efficiency E (integration); and **C)** and corrected transitivity T (segregation). Violin plots represent the distributions of points (18 subjects per condition); the box plot is constituted by the median (white circle), the first and third quartiles (box limits), and sample range (whiskers). ** : $p < 0.01$, * : $p < 0.05$, $\sim$: $p < 0.1$.

Thus, RS metrics cannot predict the outcomes of the subjects in the Go/No-Go attentional task.

5.2 MODELING THE EFFECTS OF NICOTINE ON FUNCTIONAL CONNECTIVITY

To suggest biophysical mechanisms for the effects of nicotine on functional network topology, I simulated whole-brain dynamics using the Jansen & Rit neural mass model (Jansen and Rit, 1995). As with the experimental data, brain areas were defined using the AAL90 anatomical parcellation, and connected with a SC matrix derived from MRI (Deco et al., 2018). The model

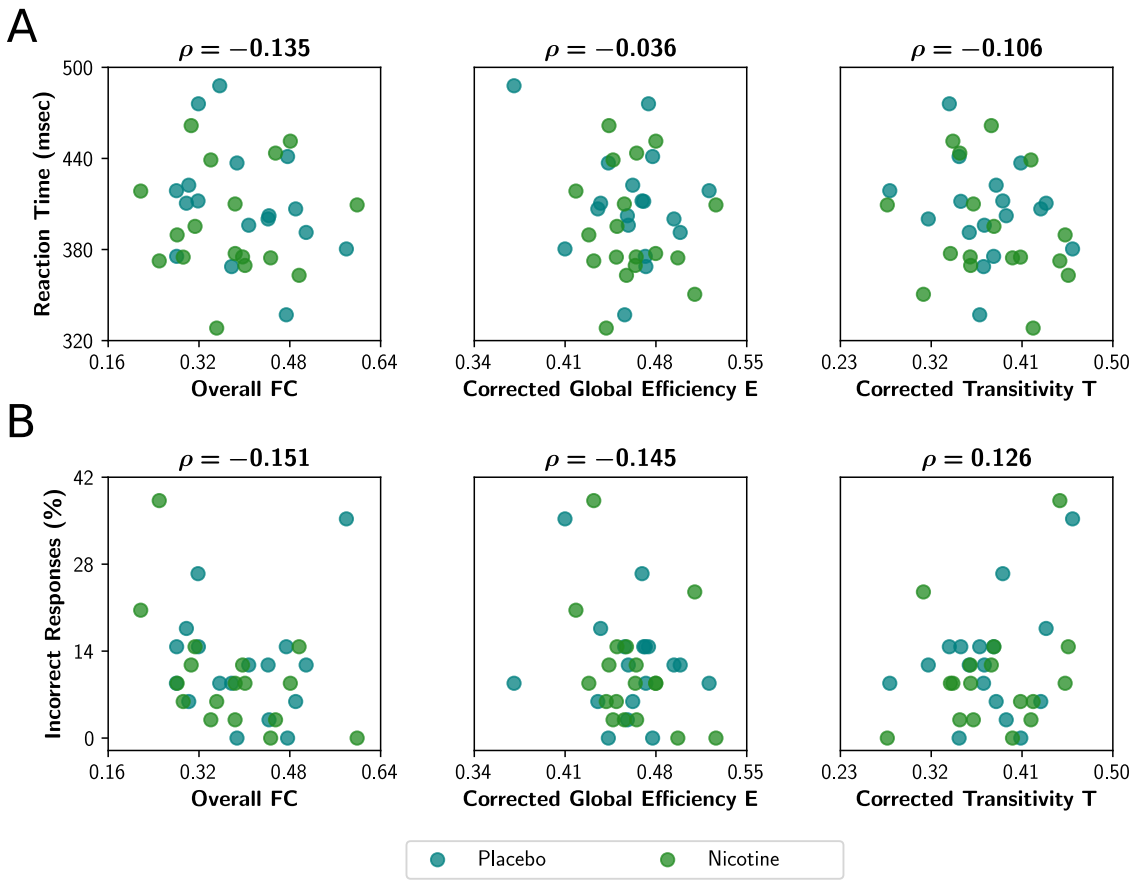

Figure 5.4: Correlation of RS FC metrics with performance A) Correlation with the reaction time (RT) of the Go trials. **C)** Correlation with the percentage of incorrect responses of the No-Go trials. Spearman ρ was used as a correlation measure. Points corresponded to participants (18 subjects per condition).

was also informed with the empirical fMRI BOLD signals (Gießing et al., 2013) (see below).

The Jansen & Rit model is built from three populations of neurons, depicted in the Fig. 3.1A-B: pyramidal neurons, excitatory interneurons and inhibitory interneurons. The brain regions are connected through a weighted undirected SC matrix. I employed an optimized SC matrix (Fig. 3.1C), obtained with an iterative optimization (Deco et al., 2019) of the original SC matrix used in Deco et al. (2018) ((Fig. 5.5)). As long-range projections are mainly excitatory (Gilbert et al., 1990; McGuire et al., 1991), brain regions in the model are connected through pyramidal populations. The simulations generate firing rates in each node of the network, which are used as an input to a generalized hemodynamic model (Stephan et al., 2007) to generate BOLD-like signals (Fig. 3-1) from which I built the FC matrices. I compared the empirical (averaged across subjects) and

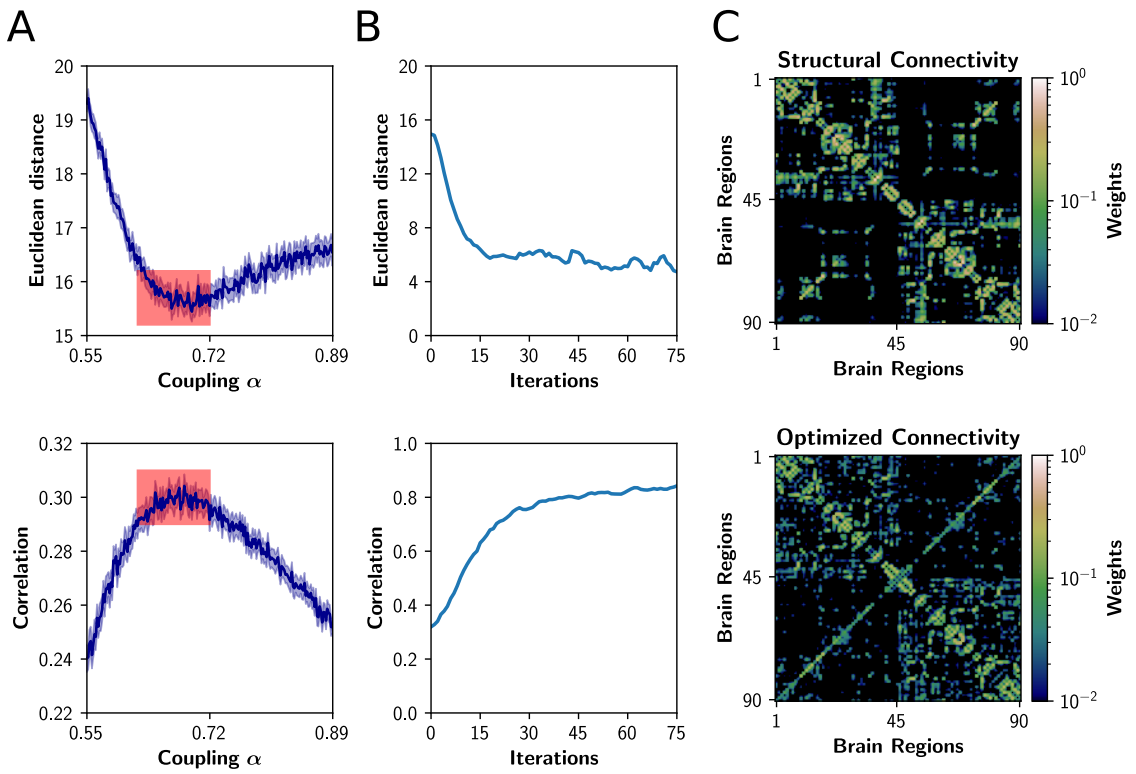

Figure 5.5: Optimization of structural connectivity. **A)** Fitting to placebo condition in RS using the original SC matrix. A better fitting corresponds to low values of euclidean distance and high values of Pearson correlation. A value of $\alpha = 0.651$, within the red squares, was used for SC optimization. **B)** Euclidean distance and Pearson correlation across iterations, for a fixed $\alpha = 0.651$. **C)** The original structural connectivity matrix (iteration number 0, top) and the optimized matrix (final iteration, bottom).

simulated FC matrices using the euclidean distance between the vectorized FCs; a lower value of distance is equivalent to a better fitting.

The set of steps are presented in the Fig. 5.6A. First, using $\beta = 0$ (no task input) the model was fitted to RS, sweeping the global coupling α and comparing the simulated FC to an average of placebo and nicotine RS FCs. The comparison was made with the euclidean distance between matrices, and I found a minimum at $\alpha = 0.648$, for placebo, and at $\alpha = 0.644$, for nicotine (Fig. 5.6B). This confirms the previous hypothesis that a decrease in α and C_4 can be used to mimic the effects of nicotine. Next, to simulate the effect of the placebo condition - task block, I swept the input slope β (Fig. 5.6C), finding a minimum at $\beta = 0.58$. A higher value of β, in general, represents an increase in the background input for almost all nodes, consistent with the idea that nodes that changed mostly their FC nodal strength, also increased its background input largely as

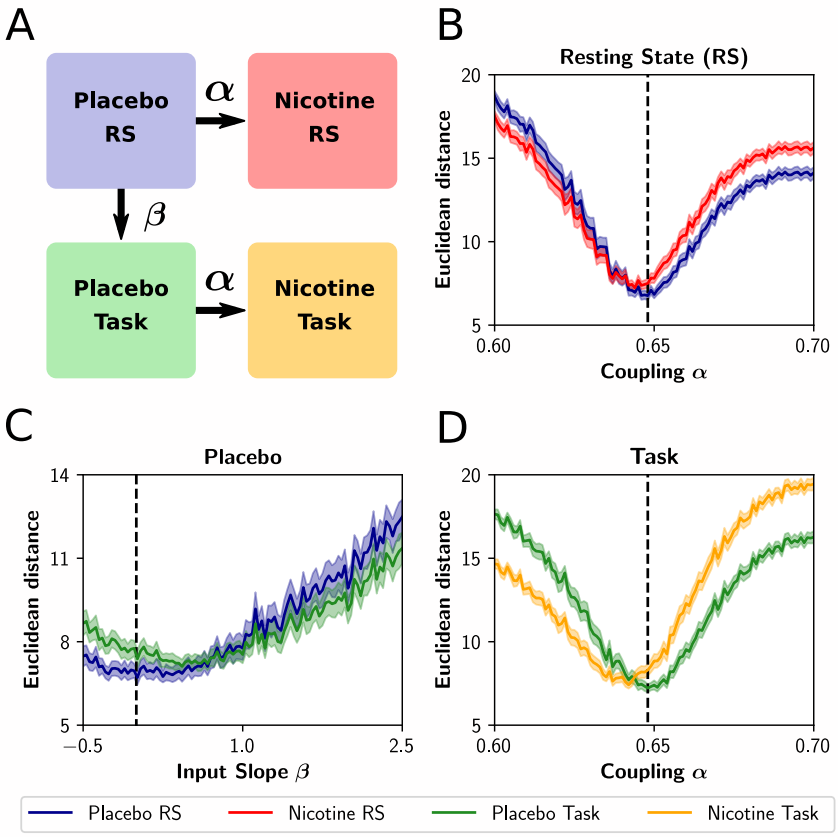

Figure 5.6: Fitting the whole-brain model. **A)** Starting from the model fitted to the placebo condition in RS, the model was then fitted to the nicotine condition in RS decreasing the value of the parameter α, and to the placebo condition during the task increasing β. Using the β value for task, nicotine condition during the task was reproduced decreasing α. **B-D)** Euclidean distance between simulated and empirical FCs as a function of α and β. The minima of the euclidean distances between empirical and simulated FC represent the values of the parameters α and β that better reproduce the empirical FCs. Dotted lines corresponded to the optimal values found for placebo - RS (B and C) and placebo - task (D). A decrease in α was accompanied by a decrease in C_4. Shaded areas represent the 95% confidence intervals (using 100 random seeds).

an effect of the task. Finally, using $\beta = 0.58$ I fitted the model to the nicotine condition - task block, sweeping α and finding a minimum at $\alpha = 0.641$ (Fig. 5.6D). Thus, a larger decrease in global coupling and feedback inhibition is required to simulate the effects of nicotine during the task.

Using the model with the fitted values of α, C_4 and β, 100 simulated FCs were obtained (with different random seeds) for all four conditions (Fig. 5-7). Qualitatively, the averaged empirical (Fig. 5.7A) and simulated (Fig. 5.7B) FC matrices show that both nicotine and task decrease global correlations. Applying the network measures to the simulated FCs, the model reproduced the empirical results. First, nicotine decreases the overall FC (Fig. 5.7C) in both RS ($p < 0.001$) and

the task blocks ($p < 0.001$), being the effect stronger in the latter. Similar to the empirical data, the following networks metrics were corrected for Overall FC (Fig. 5.8). Second, nicotine reduces E in task ($p < 0.001$) (Fig. 5.7C), but not in RS ($p = 0.419$). Lastly, nicotine increases T (Fig. 5.7C) and the effect was stronger and significant in the task block ($p < 0.001$) but not in RS ($p = 0.263$). Thus, both simulated and empirical data suggest that nicotine has a pro-segregation effect on network topology during the task, but not in RS.

5.3 NICOTINIC RECEPTORS PARTIALLY MEDIATE THE CHANGES IN FUNCTIONAL CONNECTIVITY

Computational models suggest that the regional expression of neurotransmitter receptors is a key element to precisely reproduce the changes in brain dynamics by neuromodulation (Deco et al., 2018; Luppi et al., 2021b). To assess this possibility, I tested if the regional expression of cholinergic-related receptors can explain the effects of nicotine on FC. I used regional density maps, obtained with PET (Hillmer et al., 2016; Aghourian et al., 2017; Baldassarri et al., 2018; Bedard et al., 2019; Hansen et al., 2021; Naganawa et al., 2021), to test what acetylcholine-related receptors are associated with the changes in FC observed in the empirical data. Specifically, I considered density maps –parcellated using AAL90– for the $\alpha_4\beta_2$ nicotinic receptor, the M_1 muscarinic receptor, and the vesicular acetylcholine transporter (VAChT). The difference in the empirical FC nodal strength between nicotine and placebo conditions (averaged across subjects and blocks) was calculated, and this vector was correlated with the density maps. Also, I included the nodal strength of the optimized SC in the analysis.

The correlation of density maps and SC with the changes in FC nodal strength is shown in Fig. 5.9. First, I found a negative correlation between SC nodal strength and the change in FC ($p < 0.001$, Fig. 5.9A). Thus, the nodes that are heavily connected in the network decrease most, by nicotine, their FC strength. On the side of receptors, I only found a modest negative correlation between the density of the $\alpha_4\beta_2$ receptor with the change in FC ($p < 0.05$, Fig. 5.9A), but not for the M_1 receptor ($p = 0.622$, Fig. 5.9A) and the VAChT ($p = 0.517$, Fig. 5.9A). These results

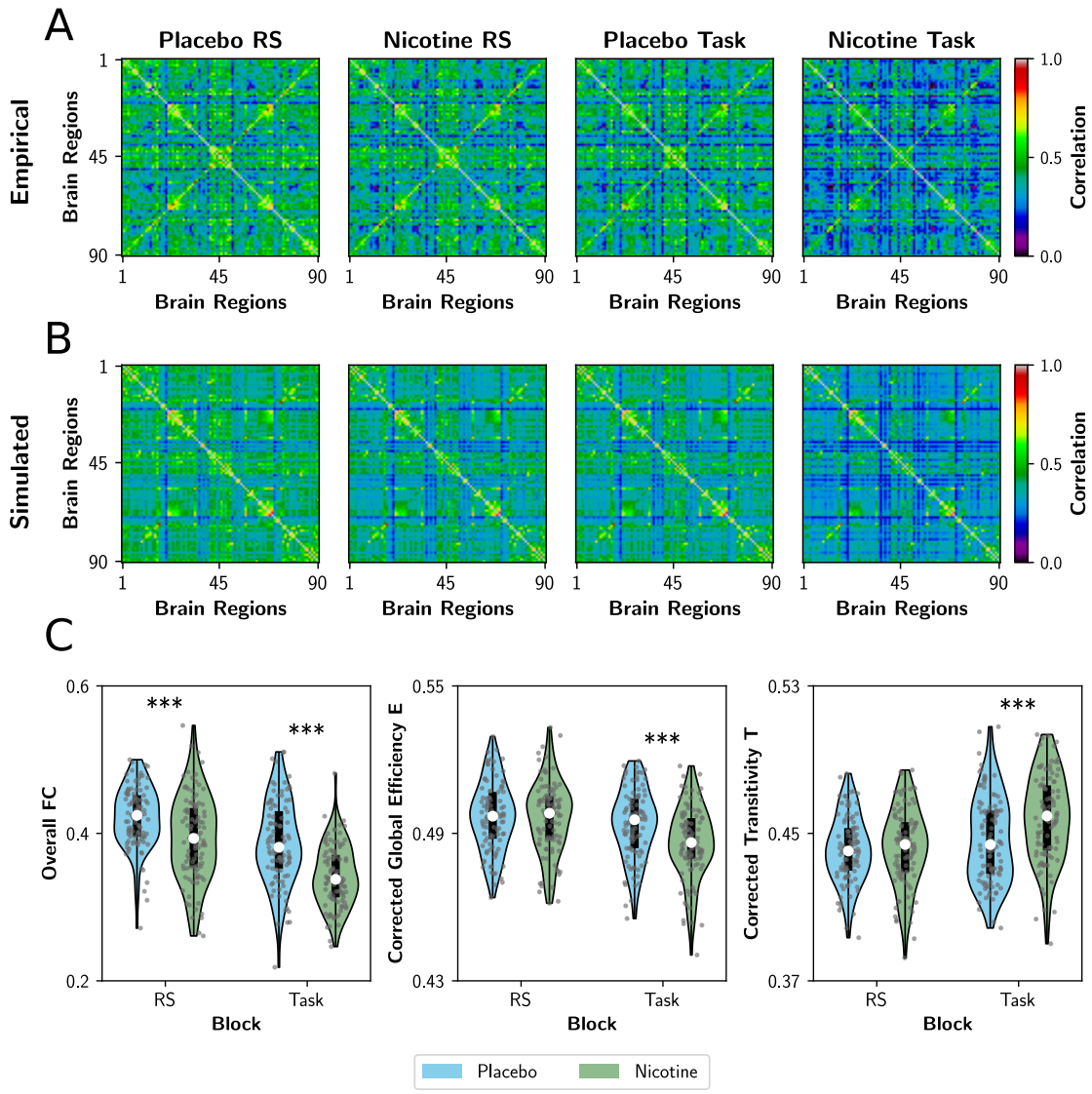

Figure 5.7: Simulated changes in functional connectivity produced by nicotine.. **A)** Empirical and **B)** simulated FC matrices, built using Pearson correlation. For the empirical data, the averaged matrices across subjects were shown ($n = 18$), and for the simulated data the averaged using different random seeds were shown ($n = 100$). **C)** Effect of nicotine on FC and network topology, both in RS and task. Violin plots represent the distributions of points (100 random seeds per condition); the box plot is constituted by the median (white circle), the first and third quartiles (box limits), and sample range (whiskers). *** : $p < 0.001$.

suggest that both the brain SC and the $\alpha_4\beta_2$ receptor might play a role in explaining the effects of nicotine on FC. To further validate if the $\alpha_4\beta_2$ receptor have a significant role in the nicotine-mediated changes in FC, I performed a multiple linear regression using the SC nodal strength and the $\alpha_4\beta_2$ density map as independent variables, and the change in FC as the dependent variable. I compared the two variables model (named SC + PET), with the simple linear regressions used

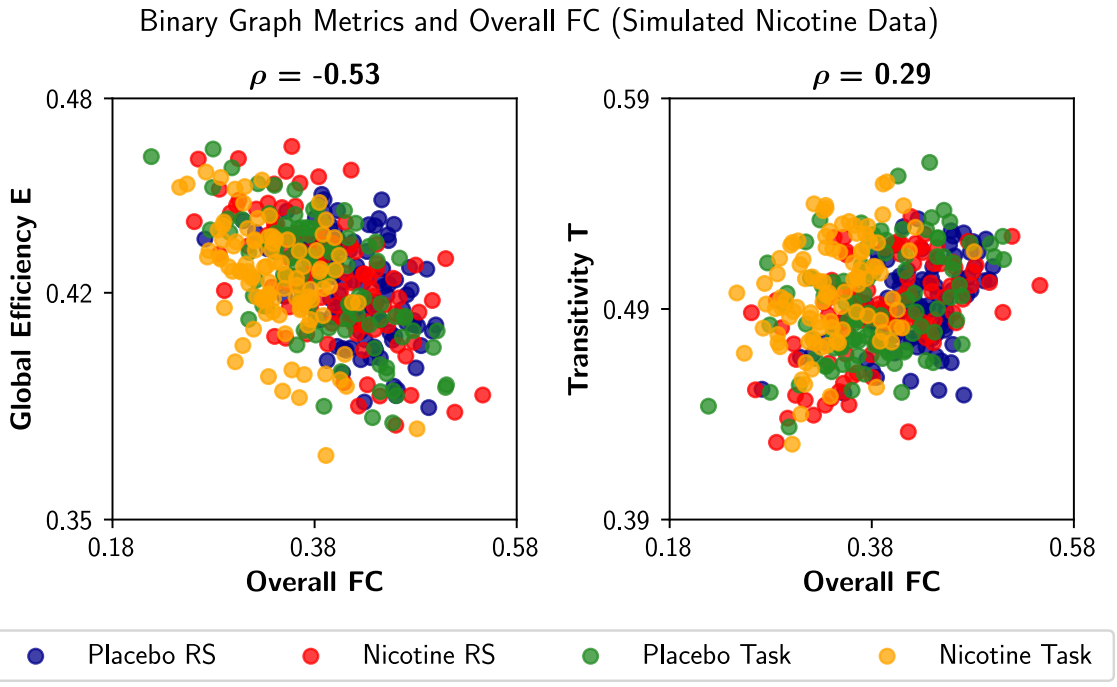

Figure 5.8: Effect of overall FC on functional network metrics (simulated data). Pearson ρ was used as a correlation measure. Points corresponded to participants (18 subjects per condition).

before (SC and PET only). For each model, I calculated the Akaike information criterion (AIC) and found that the SC + PET model for the $\alpha_4\beta_2$ receptor was the best model (AIC = 302, r^2 = 0.189), in comparison with the SC only (AIC = 306, r^2 = 0.145) and the PET only models (AIC = 315, r^2 = 0.051). Thus, both SC and nicotinic $\alpha_4\beta_2$ receptor density are key elements to explain the effects of nicotine on whole-brain FC.

If the $\alpha_4\beta_2$ receptor density map correlates with the changes in FC, a model informed with the distribution of this receptor across the brain should improve the fitting to the empirical data. I analyzed this possibility repeating the fitting performed in Fig. 5-6 for the nicotine condition, both in RS and task blocks. However, this time I changed the parameters α and C_4 proportionally to the $\alpha_4\beta_2$ receptor density map, starting from the placebo condition ($\alpha = 0.648$). Also, I used two different surrogates for comparison purposes. They consisted in a randomization of the $\alpha_4\beta_2$ receptor density vector, and an constant vector same as the one used in Fig. 5-6. I found that the $\alpha_4\beta_2$ receptor density map produces a better fitting than the two surrogates maps, but just in the task block ($p < 0.05$) and not in RS ($p > 0.148$) Fig. 5.9B. Complementary, Cohen's d indicates

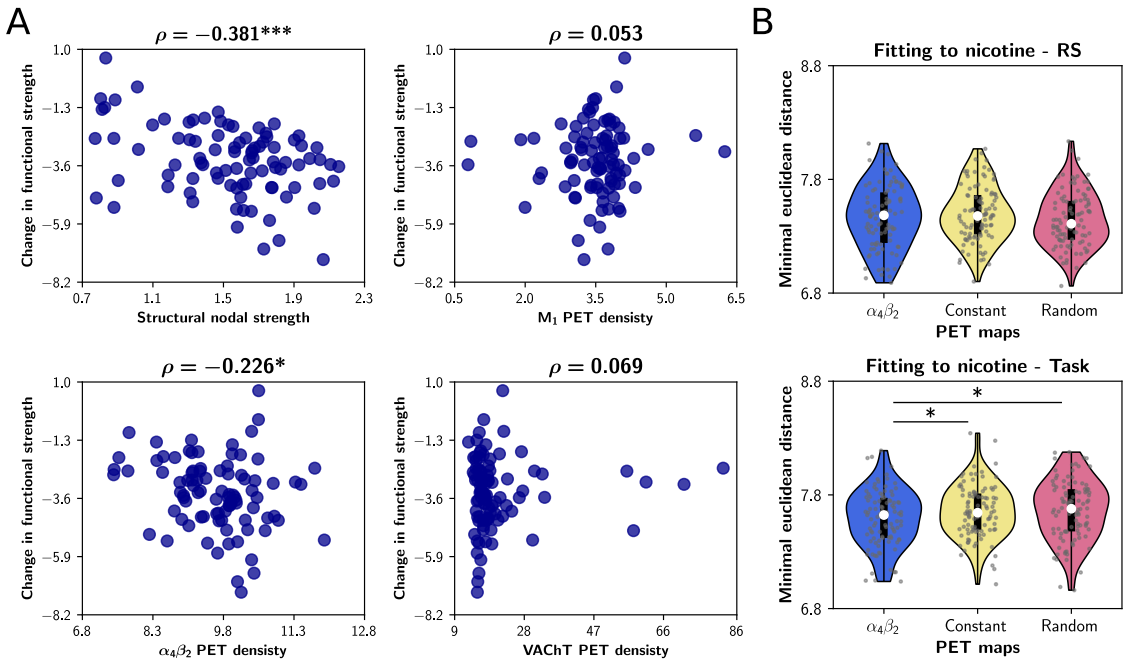

Figure 5.9: Relationship between cholinergic receptors and the nicotine-mediated effects on FC. A) Correlation between the change in empirical FC nodal strength (averaged for RS and task) with SC nodal strength and cholinergic-related receptors and transporters. **B)** Fitting to nicotine condition, both RS and task blocks, using the $\alpha_4\beta_2$ receptor density map. I compared the fitting of the original map with two different surrogates (random and uniform maps derived from the original $\alpha_4\beta_2$ receptor density vector). The minimal euclidean distance was shown. Violin plots represent the distributions of points (100 random seeds per condition); the box plot is constituted by the median (white circle), the first and third quartiles (box limits), and sample range (whiskers). Points corresponded to the AAL90 brain regions. * : $p < 0.05$, *** : $p < 0.001$.

a small effect size for $\alpha_4\beta_2$ receptor versus the constant and random surrogates ($d = -0.243$ and $d = -0.274$, respectively). Thus, the $\alpha_4\beta_2$ receptor could a play a key –but partial– role in explaining the effects of nicotine on whole-brain FC.

5.4 BRAIN DYNAMICS GET FASTER UNDER NICOTINE

To analyze how brain dynamics change with neuromodulation, I employed the sliding window method to characterize the FCD of the simulated signals. I did not include the analysis of empirical signals in this section because of their short durations (6.4 min for RS and 8-5 min for task). Instead, I took advantage of the computational model, analyzing the longer simulated recordings (20 min).

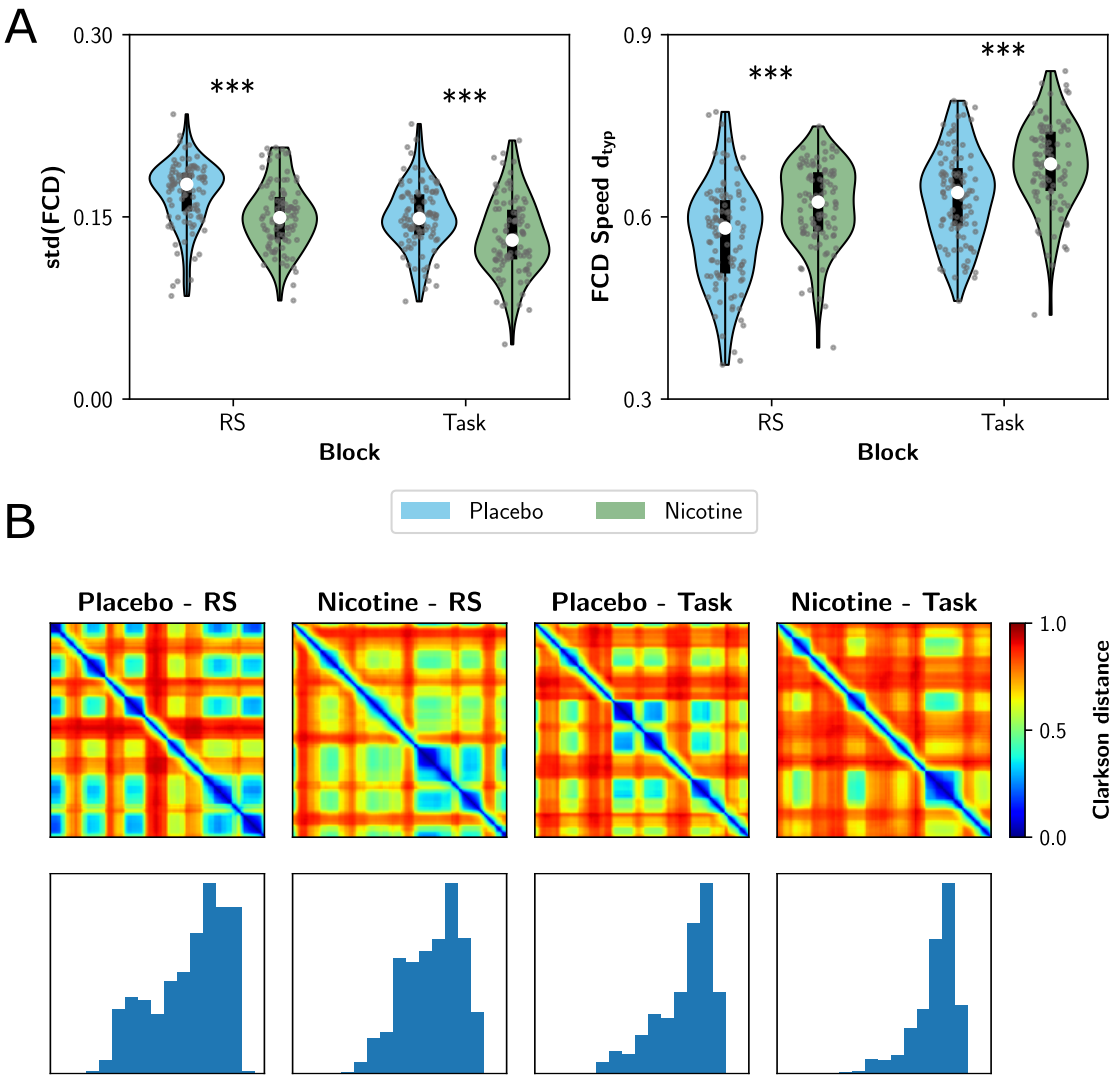

Figure 5.10: Nicotine modulation of functional connectivity dynamics (simulated signals). A) The standard deviation of the FCD matrix (left), a measure of dynamical richness, and FCD speed (right), d_{typ}, which quantifies how fast changes the FC patterns over time. **B)** Functional connectivity dynamics (FCD) matrices, and their respective histograms (below). The time vs time FCD matrices were built using Pearson correlation between the vectorized FCs. FCDs were built using 100 seconds time windows with 90% of overlap. Violin plots represent the distributions of points (100 random seeds per condition); the box plot is constituted by the median (white circle), the first and third quartiles (box limits), and sample range (whiskers). *** : $p < 0.001$.

Compared to the placebo condition, nicotine decreases the standard deviation of the FCD –a measure of dynamical richness (Orio et al., 2018)– both in RS and task ($p < 0.001$, Fig. 5.10A). Also, nicotine increases the FCD speed, d_{typ}, in the two blocks ($p < 0.001$, Fig. 5.10A). Qualitatively, those results can be observed through the FCD matrices and their histograms (the distribution of values) in Fig. 5.10B. From left to right, FCDs become less patchy and more

red-colored. This indicates that brain dynamics get faster as an effect of nicotine and the task. FC patterns also become more incoherent (less correlated), feature related to the decrease in the dynamical richness (the standard deviation of FCDs's histograms) by nicotine. The effect of nicotine, on brain dynamics, might comprise a de-correlation of FC patterns over time, producing faster dynamics with more incoherent patterns of connectivity.

5.5 EEG SIGNATURES OF NICOTINE

As commented before (**Whole-Brain Models For Understanding Neuromodulation** section), one of the advantages of employing computational models is to recover latent information, that is, information that is not available in the experiment (Blohm et al., 2020). In the specific case of this chapter, empirical fMRI data was provided, but the neural dynamics in faster timescales (e.g., EEG-like) was unreachable. However, the computational model fitted to each condition and block, using the empirical fMRI data, can be employed to gain some insights of the possible effects of nicotine in human EEG signals.

In the faster EEG time-scale, nicotine increases the relative power of the alpha band oscillations, and decreases the relative power of theta oscillatons, both in RS and task ($p < 0.001$ for all comparisons, Fig. 5.11A-B). Thus, similar to the results observed in Fig. 4.2B, nicotine produces a shift to faster oscillations. Further, the drug reduces the global phase synchrony, and slightly raises the mean firing rates of the neural masses ($p < 0.001$ for all comparisons, Fig. 5.11C-D). It is important to remark that the task, by itself, increases the mean firing rates in comparison with the RS condition (Fig. 5.11D). Finally, nicotine increases FC dimensionality (the number of eigenvalues needed for explaining the 50% of the FCs' variance) for both EEG-like ($p < 0.001$ for all comparisons, Fig. 5.11E) and BOLD-like FCs ($p < 0.01$ for RS and $p < 0.001$ for task, Fig. 5.11F). This suggests that, as a consequence of increasing the statistical dimensionality, nicotine enriches the information content of the neural signals, that is, more dimensions (eigenvalues) were required for explaining the same amount of information (variance of the FCs).

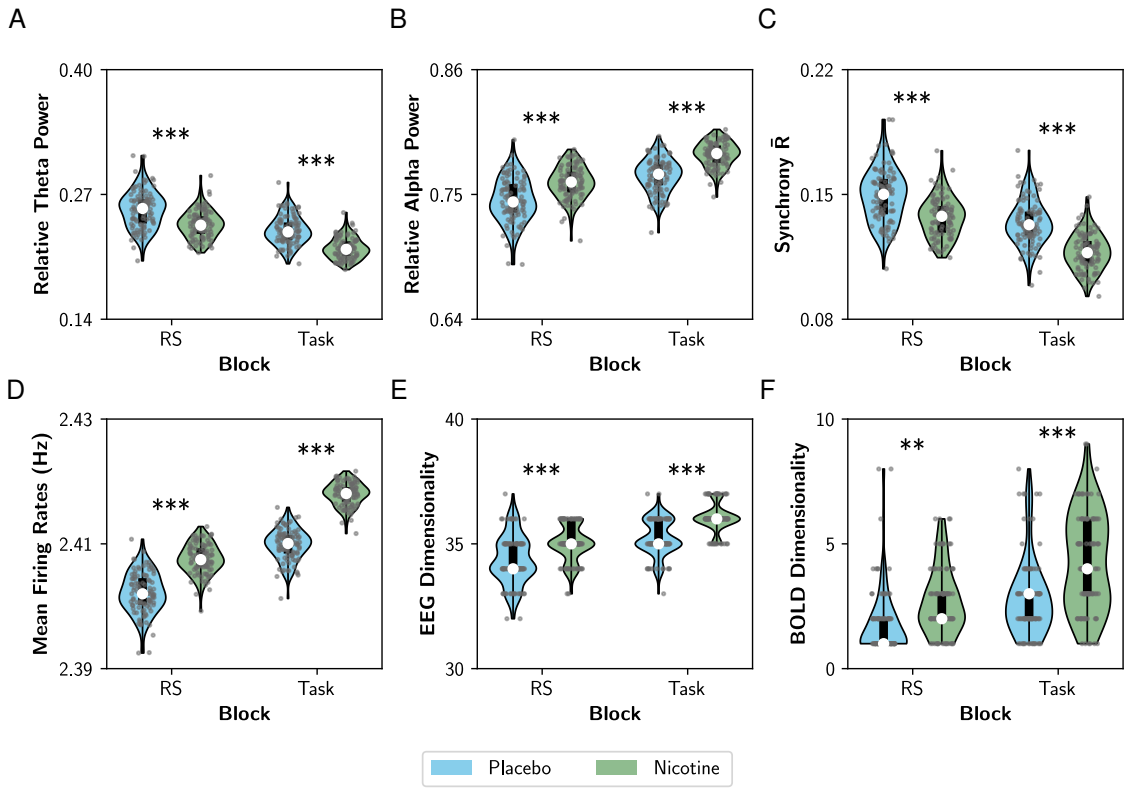

Figure 5.11: Effects of nicotine on EEG-like simulated signals. A-B) Relative power, normalized by broadband spectrum (0.5 - 12 Hz), of theta (4 - 8 Hz) and alpha (8 - 12 Hz) frequency bands of EEG. **C-D)** Global phase synchrony and mean firing rates of the Jansen & Rit neural masses. **D-E)** Statistical dimensionality of the EEG-like and BOLD-like (simulated, not empirical) FCs. Violin plots represent the distributions of points (100 random seeds per condition); the box plot is constituted by the median (white circle), the first and third quartiles (box limits), and sample range (whiskers). ** : $p < 0.01$, *** : $p < 0.001$.

The results presented in this section are derived from the computational model, and not directly for empirical data. In consequence, they constitute possible predictions to be tested, and must be interpreted with caution.

5.6 SUMMARY

The principal result presented in this section is the pro-segregation effects of acetylcholine, at the whole-brain level. The effect is also context-dependent: observed in the task block, but not in RS. Within the task, nicotine improves the performance of the subjects (lower reaction time). The in-task segregation negatively correlates with the reaction time, finding a link between

functional network topology and behavior. The fitted whole-brain neural mass model, to empirical FCs, reproduces the shift to functional segregation by nicotine observed in experimental data. I observed that the regional expression of the nicotinic acetylcholine $\alpha_4\beta_2$ receptor correlates with the empirical change in FC, and also improves the fitting of the model to the nicotine condition in the task block. This last result emphasizes the relevance of nicotinic acetylcholine receptors for explaining the whole-brain changes in FC produced by the cholinergic system. Finally, the model makes some predictions in relation to the effects of nicotine. Through FCD analysis, the model predicted a decrease in variability (dynamical richness) and an increase of FC fluctations (FCD speed) by nicotine. Using the simulated signals, I found that the drug incremented the power of alpha oscillations, the mean firing rates of neural masses and the information content (statistical dimensionality) of the EEG-like and BOLD-like FCs.

Chapter 6

Results Part Three: Structural Features of the Human Connectome That Facilitate the Switching of Brain Dynamics via Noradrenergic Neuromodulation

In this section, I analyzed the relationship between brain SC and neuromodulatory systems. To investigate this issue, I built a whole-brain model based on the Jansen & Rit equations (Jansen et al., 1993; Jansen and Rit, 1995) coupled to a human SC matrix, that allows to simulate the effect of the noradrenergic system on the functional integration and segregation features of the network (Coronel-Oliveros et al., 2021b). The interaction between neuromodulation and structural connectivity was studied at three levels: at the global-scale, using random surrogate connectomes that preserve the number and strength of connections but disrupt the global patterns. At the meso-scale, determining whether the modulation of a node subset containing the anatomical rich club (Opsahl et al., 2008; Van Den Heuvel and Sporns, 2011) or the critical *s*-core (Garas et al., 2012; Eidsaa and Almaas, 2013), is optimal to produce a change in network dynamics, compared to randomly chosen subsets. At the local-scale, exploring which local properties define the set of nodes that, when being neuromodulated, maximize the effect on network dynamics.

6.1 HUMAN STRUCTURAL CONNECTIVITY ENHANCES DYNAMICAL RICHNESS

First, I analyzed how neuromodulation depends on the connectivity pattern of the human connectome by using different randomized surrogate connectomes. I employed a degree- and strength-preserving randomization (DSPR), which randomizes the structural connectivity while

preserving original degree and strength distributions (Fig. 6.1B); in this way the effect of disrupting the global connectivity without altering the local nodal properties can be studied. In addition, I employed a complete randomization of the structural connectivity (Fig. 6.1C), which does not preserve the degree and strength distributions. Finally, a homogenization (binarization) of the connectome was considered (Fig. 6.1D); this surrogate preserves the topology, disrupting the non-uniform weight distribution. I simulated EEG-like and fMRI BOLD-like signals from the Jansen & Rit model at different combinations of $\alpha \in [0, 1]$ and $r_0 \in [0, 1]$ parameters. Here, the value of the parameters is equal for all the nodes, and I refer to this case as uniform neuromodulation. I computed the mean of the Kuramoto order parameter, also known as phase synchrony $\bar{R}$, the global efficiency, E^w, and the modularity, Q^w, as measures of global phase synchronization, integration, and segregation, respectively. Global efficiency is a measure of integration defined as the inverse of the characteristic path length (Rubinov and Sporns, 2010). High values of E^w represent an efficient coordination between all pairs of nodes in the network, a signature of integration. Modularity is a measure of segregation based on the detection of network communities, or modules (Rubinov and Sporns, 2010); high modularity Q^w is associated with segregation and vice-versa.

Fig. 6.1A shows how neuromodulation of the human connectome causes a shift of the model towards a synchronized and integrated state, with maximum integration observed in an intermediate region of the parameter space, as previously reported in (Shine et al., 2018a; Coronel-Oliveros et al., 2021b). The synchrony $\bar{R}$ has an upper bound of 0.76, that is, the network never fully synchronizes. The transition is gradual, with many regions showing an intermediate behavior characterized by higher metastability and richer dynamics (Coronel-Oliveros et al., 2021b; Zamora-López et al., 2016; Shine et al., 2018a). Moreover, the region of the parameter space where $\bar{R}$ increases matches the increment in global efficiency, E^w, verifying a link between the fast dynamics of EEG and the slower one of fMRI-BOLD.

I repeated the same exploration using the DSPR surrogate connectome Fig. 6.1B) (Rubinov and Sporns, 2011). The area of synchronized activity in the parameter space (r_0, α) is reduced, and a spot of over-synchronized activity can be appreciated. Most importantly, the area of

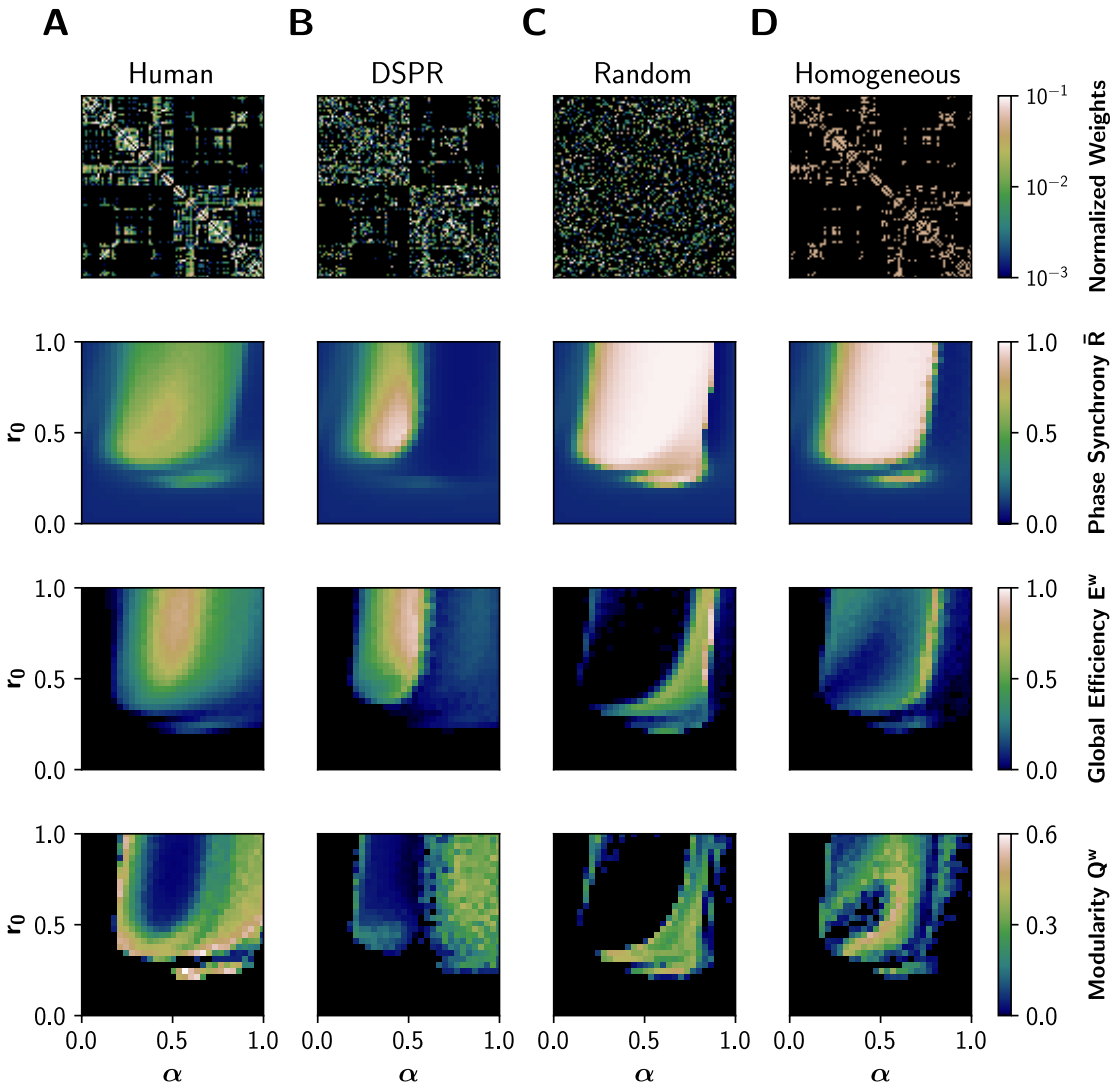

Figure 6.1: Effects of network structure in neural synchronization and integration. From top to bottom: structural connectivity matrix, phase synchrony $\bar{R}$, global efficiency E^w (a measure of integration), and modularity Q^w (measure of segregation), obtained in the model with different structural connectivities. $\bar{R}$ was obtained from EEG-like simulated activity, while E^w and Q^w were calculated using the FC obtained from the corresponding fMRI BOLD-like traces. **A)** Human structural connectivity (Human). **B)**, Degree- and strength-preserving randomized version of Human (DSPR). **C)** Randomized version of Human, where weight values were shuffled across the full matrix (Random). **D)** Homogeneous version of Human, having the same weight in all connections (Homogeneous).

intermediate values of synchrony and integration is largely reduced, suggesting a reduction of dynamical richness. When the connectivity matrix is completely randomized (Fig. 6.1C), or made homogeneous by assigning equal weights to all connections (Fig. 6.1D), neuromodulation produces a large area of over-synchronized activity in the parameter space and fewer regions with

intermediate behavior.

The dramatic decrease in E^w in Fig. 6.1C-D is a consequence of the over-synchronization ($\bar{R} \approx 1$) triggered by randomization. When signals are highly synchronized in the model, the envelope in the alpha band of the EEG (between 8-13 Hz) becomes flat, and so does the BOLD-like signal calculated with the hemodynamic model (Foster et al., 2016). For this reason, this drop in E^w should not be interpreted as a reduction of integration but a limitation of the hemodynamic model employed in input simulations. Nevertheless, an over-synchronized regime of activity is a feature never found in the healthy brain (Miron-Shahar et al., 2019).

Thus, in line with several previous reports (Cabral et al., 2014; Zamora-López et al., 2016; Wang et al., 2019; Fukushima and Sporns, 2020), disrupting the organization of the human connectome (or the weight relationships between nodes) causes over-synchronization, while highly metastable regimes can not be easily reached employing neuromodulation.

In the following, I will study which local- or meso-scale organization features are determinant in the effect of neuromodulation of human connectome by evaluating the network behavior when changing the r_0 parameter in subsets of network nodes.

6.2 NEUROMODULATION OF HIGH-STRENGTH NODES PROMOTES BETTER FUNCTIONAL INTEGRATION

In this section, I investigate the impact on functional integration when an increasing number of nodes are neuromodulated. The order in which nodes are modulated is defined considering nodal measures obtained from the structural matrix M. I calculated, for each node $i \in [1 \dots n]$: node strength, K_i^w, nodal efficiency, E_i^w, and clustering coefficient, C_i^w (Rubinov and Sporns, 2010). The superscript w indicates the use of the weighted versions of the measures. Then, for each metric, nodes were ordered either from high to low or from low to high. I fixed the global coupling $\alpha = 0.65$, and swept $r_0 \in [0.33, 1]$ and the number of nodes being neuromodulated in $[0, 90]$ in steps of three. As before, I used the EEG-like and BOLD-like signals to extract synchrony, integration and segregation.

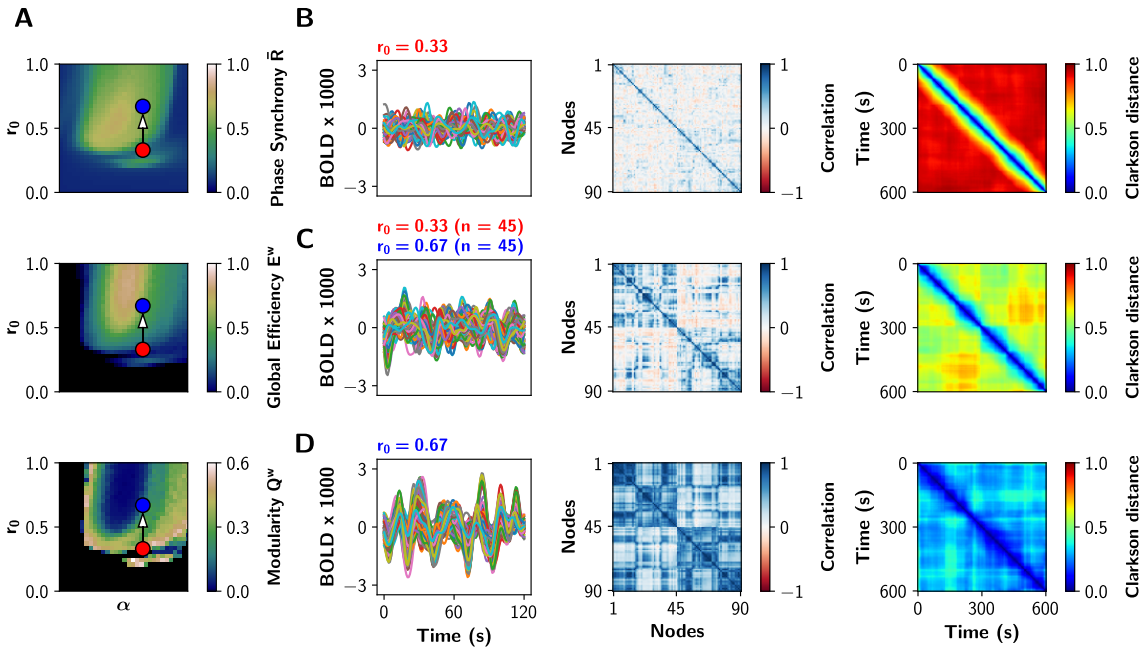

Figure 6.2: Partial noradrenergic neuromodulation. A) The (α, r_0) parameter space showing Phase synchrony $\bar{R}$, global efficiency E^w, and modularity Q^w, for the Human connectome (same as in Fig. 6.1A). Blue and red dots are references for panels B-D. **B-D)** BOLD-like signals, FC and FCD matrices obtained when all nodes have $\alpha = 0.65$ and B) $r_0 = 0.33$; C) 45 nodes have $r_0 = 0.33$ and 45 nodes have $r_0 = 0.67$; and D) all nodes have $r_0 = 0.67$. In C, the 45 nodes with the highest strength were modified to $r_0 = 0.67$.

A particular example of partial neuromodulation is shown with some detail in Fig. 6.2. The (α, r_0) parameter space is shown in Fig. 6.2A depicting global phase synchrony $\bar{R}$, global efficiency E^w and modularity Q^w in a uniform neuromodulation scenario (all nodes identical). Fig. 6.2B shows sample BOLD traces, the functional connectivity (FC) and the functional connectivity dynamics (FCD) matrices for $\alpha = 0.65, r_0 = 0.33$ (red dot in Fig. 6.2A). The FCD matrix visually represents the dynamical richness of the network, by computing time-dependent FCs using sliding windows (Cabral et al., 2017a; Orio et al., 2018). Then, FCs are vectorized and compared to each other using the Clarkson distance (Clarkson, 1936), resulting in a matrix of time vs time. At the bottom, Fig. 6.2D shows the same analysis for $\alpha = 0.65, r_0 = 0.67$ (blue dot in Fig. 3A). In the middle, Fig. 6.3C shows the results when only half of the nodes have been neuromodulated to $r_0 = 0.67$ while the rest remain with $r_0 = 0.33$. As the number of nodes with $r_0 = 0.67$ increases, the FC matrices become more integrated (high E^w and low Q^w values). Similarly, the FCD matrices change from incoherence (red FCD), to exhibit multi-stable behavior (FCD with yellow-

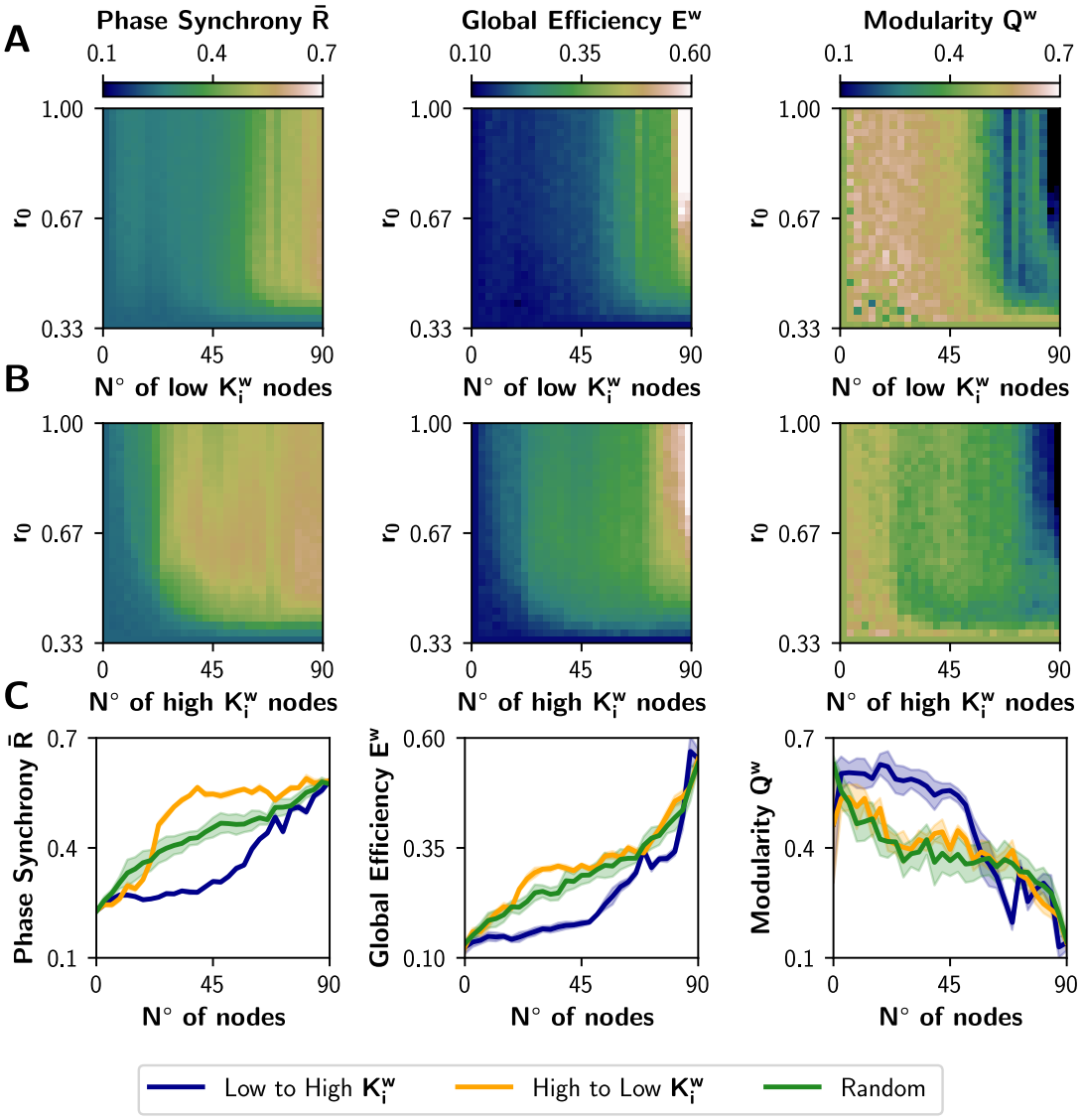

Figure 6.3: Incremental neuromodulation based on node strength. A) Effect of the neuromodulation on phase synchrony $\bar{R}$, global efficiency E^w, and modularity Q^w, at different combinations of r_0 and number of neuromodulated nodes. Nodes were affected by neuromodulation according to their strength, from low to high.. **B)** Effect of the neuromodulation of nodes sorted from high to low strength. **C)** Metrics as a function of the number of neuromodulated nodes, for $r_0 = 0.67$ as target value. Blue curves for neuromodulation of nodes with low strength, orange the opposite, and green for a random ordering of the nodes. Shaded areas correspond to 95% confidence intervals, for 10 realizations.

green patches), and finally to show correlated FC patterns (blue FCD). In summary, the increment of the number of neuromodulated nodes increases phase synchrony, functional integration, and the time correlation of FCs captured by the FCD.

Fig. 6.3 shows the result of neuromodulating r_0 with a target value in the $[0.33, 1]$ interval

and with the number of neuromodulated nodes ranging from 0 to 90. The order in which nodes are neuromodulated is either from low to high K_i^w (Fig. 6.3A) or viceversa (Fig. 6.3B). When the number of neuromodulated nodes is large, $\bar{R}$ and E^w raise markedly in both cases; the opposite can be observed for Q^w. However, picking the nodes of high strength first (Fig. 6.3B) has greater impact in the change of those metrics. The difference is best appreciated in Fig. 6.3C, where a target r_0 value of 0.67 was selected. There, the curves for the high to low K_i^w sorting (in orange) present a larger effect at the beginning, compared with the low to high K_i^w sorting (in blue). I can conclude that nodes with higher strength have a greater impact on functional integration, and inspection of the colormaps of Fig. 6.3A-B reveals that this is true for almost all values of target r_0. The results were also compared with a random selection of nodes for neuromodulation (green curves). As the blue curve is mainly below the green curve, neuromodulation of nodes with low K_i^w produces less synchronized and integrated dynamics than expected by a random neuromodulation. In contrast, choosing high K_i^w nodes is not different from random selection, when looking at the measures of integration and segregation. In consequence, there is a range (or possibly a set) of nodes that produce a robust integration when neuromodulated, compared to a random choice of nodes.

I compared the results of sorting the nodes based on strength K_i^w, with ranking the nodes based on nodal efficiency E_i^w or clustering coefficient C_i^w (Fig. 6.4). A node with a high E_i^w has many short paths to the rest of the nodes of the network, while a high C_i^w is expected for nodes whose neighbors are also connected between them. Fig. 6.4A shows the result of modulating an increasing number of nodes from a basal $r_0 = 0.33$ to a target $r_0 = 0.67$, when the nodes are ordered from low to high or high to low E_i^w. The results are similar to the ones obtained using the strength K_i^w: neuromodulation of nodes of high E_i^w has a greater impact in synchronization and integration, compared with the nodes of low E_i^w. Here, the random sorting of nodes is similar to the high to low E_i^w. However, when the nodes are sorted according to their C_i^w (Fig. 6.4B), there is little difference compared to random sorting.

When comparing the results in Fig. 6.4A-B with the neuromodulation of a random subset of nodes (green curves), there is no clear advantage of selecting the nodes with high E_i^w or C_i^w.

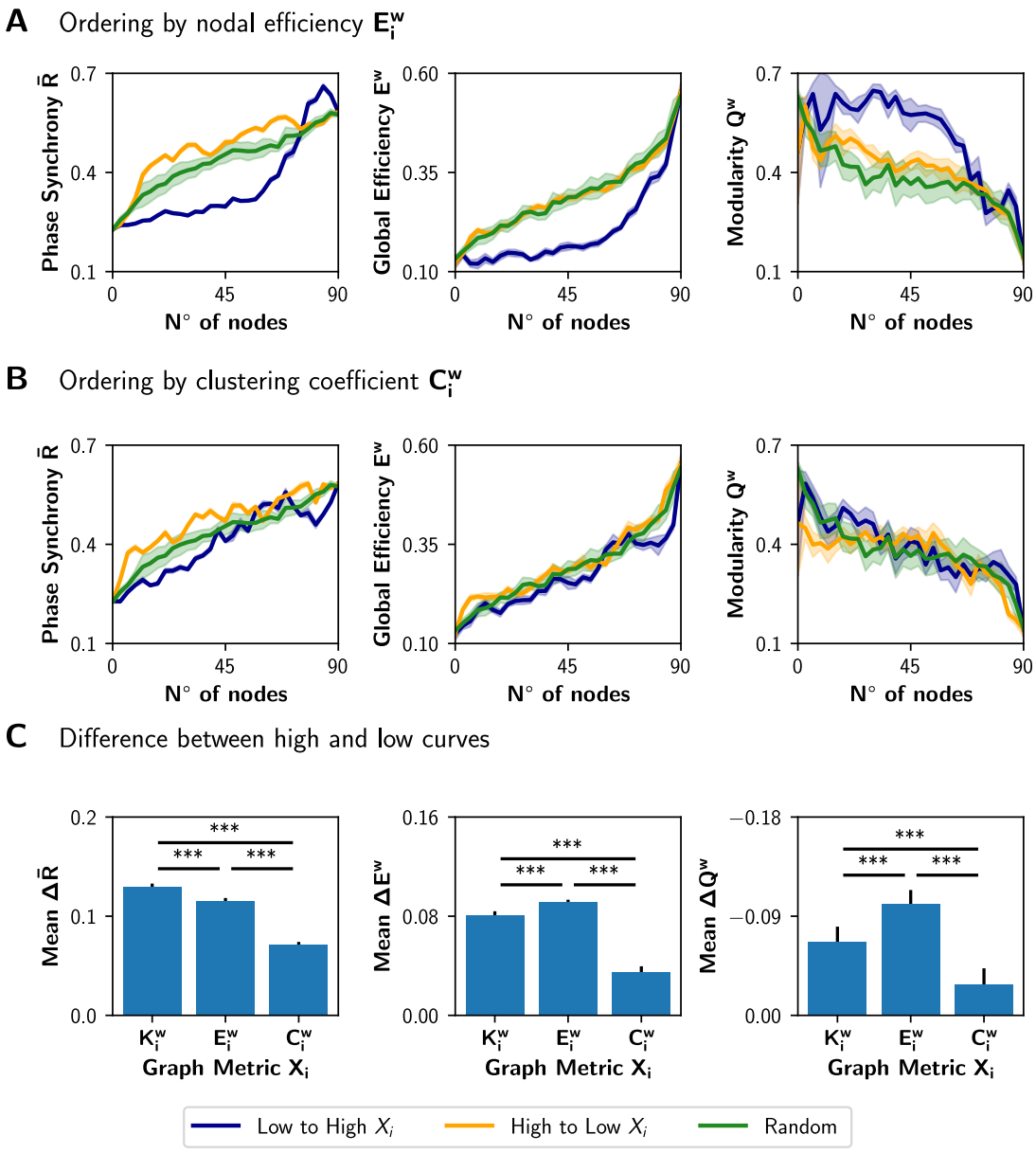

Figure 6.4: Incremental neuromodulation based on nodal efficiency and clustering coefficient. A-B) Phase synchrony $\bar{R}$, global efficiency E^w, and modularity Q^w as a function of the number of neuromodulated nodes, for $r_0 = 0.67$ as target value. In A, nodes were sorted according to nodal efficiency, E_i^w, and in B, according to the clustering coefficient, C_i^w. Blue curves for sorting of nodes from low to high (of the particular metric), orange is from high to low, and green for a random sorting of the nodes. **C)** Difference between the area under the curve (AUC) of high versus low sorting, averaged over the 10 realizations. Shaded areas in **A-B)** correspond to 95% confidence intervals, and barplots were built using the mean $\pm$ standard deviation. ***: $p < 0.001$.

Despite the increase in $\bar{R}$ is slightly higher for the orange curves, compared with the green curves, the difference in E^w is unnoticeable, except in Q^w when ordering the nodes from high to low E_i^w.

These results contrast with the ones in Fig. 6.4C, where the neuromodulation of nodes with high K_i^w produced an increase in synchronization and integration higher than random neuromodulation.

To summarize these results, I computed the difference between the area under the curve (AUC) for the high-to-low minus low-to-high (orange minus blue AUCs) (Fig. 6.4C). A larger difference implies a higher impact of neuromodulating first the nodes with a higher value of the chosen metric in synchronization, integration and segregation. The mean difference in the AUCs for the measures $\Delta\bar{R}$, ΔE^w and $-\Delta Q^w$ (note that the sign is inverted for visualization purposes), is lower for C_i^w than for K_i^w and E_i^w ($p < 0.001$ for all comparisons using Student's t test).

6.3 NEUROMODULATION OF RICH CLUB NODES STRONGLY IMPACTS FUNCTIONAL INTEGRATION

Node strength, nodal efficiency and clustering coefficient are considered local-scale properties, i.e., they belong to each node. Several meso-scale level network properties have been described as being determinant for network dynamic, too, such as the rich club organization (Van Den Heuvel and Sporns, 2011) and the *s*-core (Hagmann et al., 2008; Garas et al., 2012; Eidsaa and Almaas, 2013; Castro et al., 2020). I identified the nodes belonging to the "rich club", using the weighted rich club coefficient $\phi^w(K)$, where K is a threshold based on degree (Opsahl et al., 2008). The rich club comprises a subset of the graph, thresholded at K, in which nodes are more strongly interconnected than expected by chance (Van Den Heuvel and Sporns, 2011). The coefficient is normalized using random surrogates $\phi^w_{rand}(K)$, in this case DSPR surrogates (Rubinov and Sporns, 2011). If the normalized coefficient $\phi^w_{norm}(K)$ is greater than 1, the network has a rich club organization at threshold K. Fig. 6.5A shows a plot of $\phi^w_{norm}(K)$ (blue) as a function of K. The red arrow marks the point in which the normalized coefficient is maximal ($\phi^w_{norm}(K) = 1.367, p < 0.002$). Then, I identified feeder nodes –nodes that do not belong to the rich club but are connected to at least one of its members– and local nodes –connected to feeders but not to the rich club (Fig. 6.5B). I found 17 nodes belonging to the rich club, 60 feeders and 13 local nodes (Fig. 6.5B). The rich club members are the brain regions in Table 4.

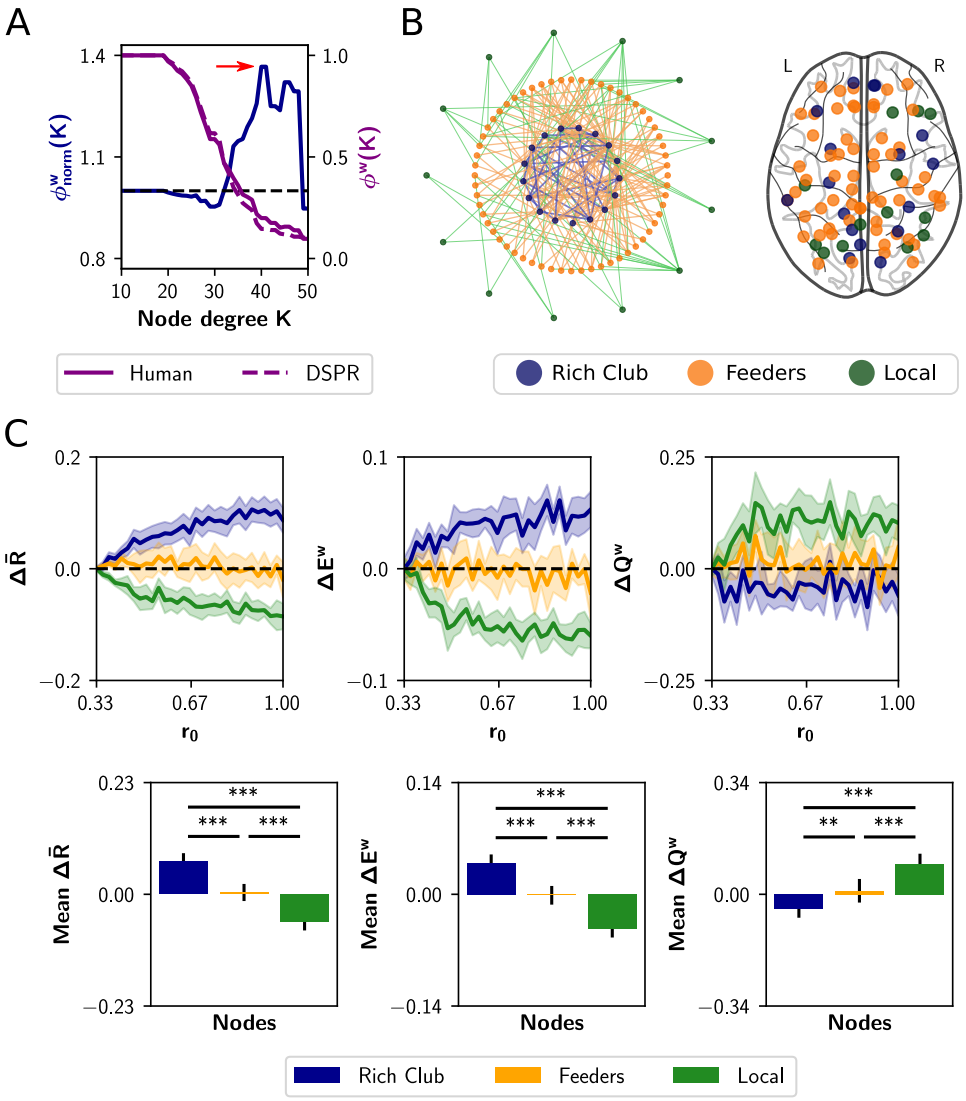

Figure 6.5: Neuromodulation based on the rich club organization. **A)** Normalized and weighted rich club coefficient $\phi^w_{norm}(K)$ (blue curve), as a function of the degree-based threshold K. This coefficient was calculated as the ratio between the human rich club coefficient (purple solid curve) and the mean coefficient for random surrogates (DSPR, purple dashed curve). The red arrow marks the point in which $\phi^w_{norm}(K)$ is maximal; rich club nodes were found at that point. **B)** Schematic depiction of the rich club, feeders (not belonging to the rich club, but connected with it) and local nodes, (connected only to feeders). At the right, I show a glass brain with the nodes identified rich club (n = 17 nodes), feeders (n = 60) and local (n = 13). **C)** Changes in synchrony $\bar{R}$, global efficiency E^w and clustering coefficient Q^w when neuromodulating 24-node sets containing the rich club (blue), local nodes (green) or only feeders (orange). The results are shown as the difference with respect to a random subset of nodes of equal size (null case). The bottom row summarizes the area under the curve (AUC) for each metric and nodal category, averaged over the 10 realizations. Shaded areas correspond to 95% confidence intervals, and bar plots were built using the mean $\pm$ standard deviation. **: $p < 0.01$, ***: $p < 0.001$.

As the analysis of the rich-club properties of the human SC defines sub-networks instead of sorting the nodes, I chose a different approach than the neuromodulation of increasing subsets of nodes. Here, I simulated neuromodulation of a fixed-size subset of nodes, that included all nodes belonging to a certain category (rich club, feeders or local). Because the categories differ in size, I complemented the rich club and local nodes with 7 and 11 nodes, respectively, selected randomly from the feeders. For the last one, I randomly chose 24 feeder nodes. Also, a null case was considered, composed of 24 nodes randomly selected from the complete set of nodes. I repeated the random selection of nodes with 10 realizations, always using subsets of 24 nodes. The nodes started with a basal r_0 value of 0.33, and r_0 was swept up to 1 but only in the designated subset of nodes. For each r_0 increment, I measured $\bar{R}$, E^w and Q^w. Then, I subtracted to each measurement the result of the null case. The results are shown in Fig. 6.5C. Neuromodulation of the rich club nodes produces an increase in synchronization and integration, and a decrease in modularity, above chance. The difference becomes more pronounced with further increments of r_0. Opposite results were observed for the subsets containing local nodes. Finally, neuromodulation of subsets containing only feeder nodes produce no difference compared to random selection of nodes. As a summary index, I calculated the AUC for each nodal category (Fig. 6.5C). Considering the three measurements, the AUC is higher (lower in the case of modularity Q^w) for the rich club respect to feeders and local, and higher (lower in the case of Q^w) between feeders and local ($p < 0.001$ for all comparisons using Student's t test). The results show that noradrenergic neuromodulation of a subset including the rich club nodes has a greater impact on integration compared to the feeders, locals, and a random selection of nodes.

As previously shown, functional integration is also achieved by neuromodulation of highest strength nodes. To highlight the difference between the local and meso-scale approaches, I quantified the overlap between the rich club nodes and the 17 nodes with higher strength. I found that only 8 members of the rich club belong to the subset of 17 nodes with higher strength (Table 4). Thus, there are some high-strength key nodes that do not belong to the rich club, that promote functional integration via neuromodulation.

To explore a second meso-scale network organization, I performed a *s*-core decomposition

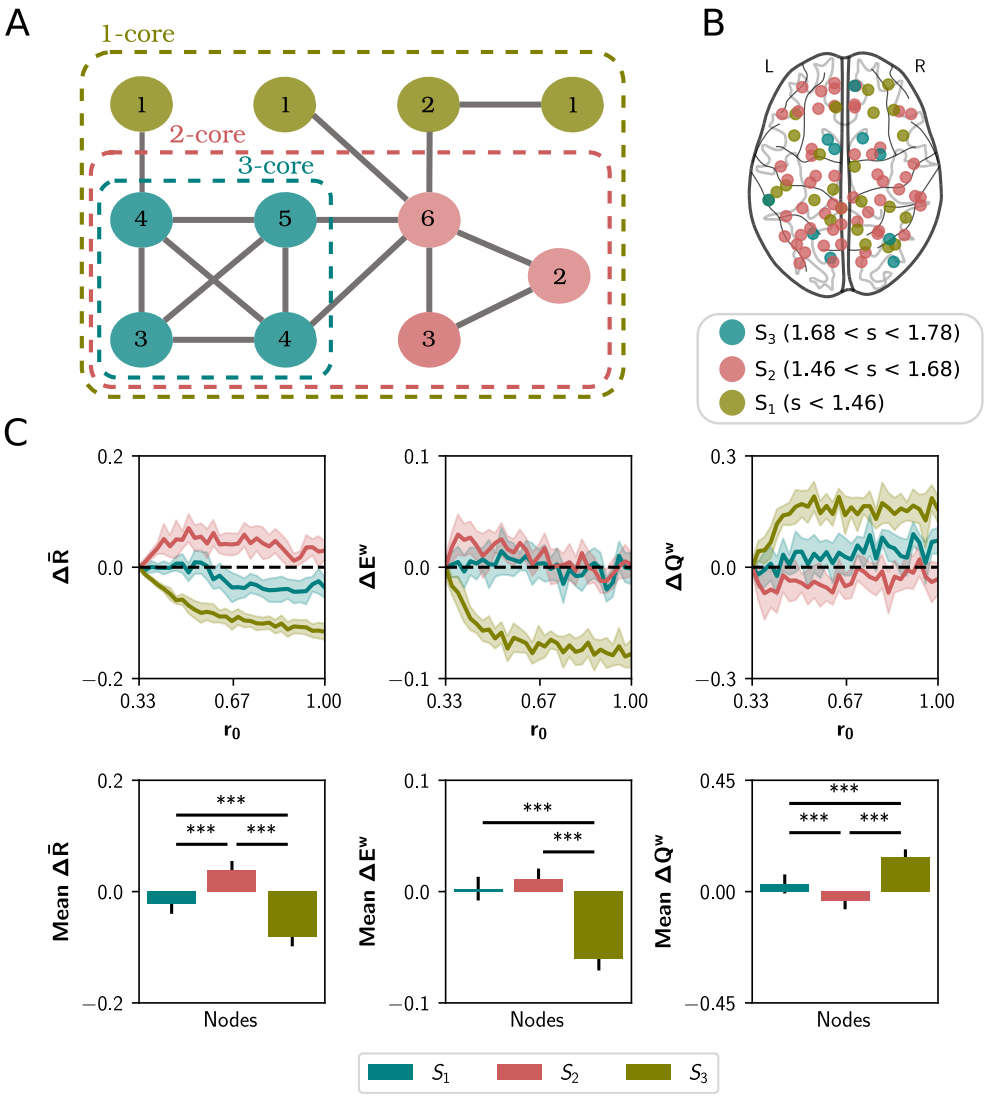

Figure 6.6: Neuromodulation based on the *s*-core decomposition. A) *s*-core decomposition. At the left, example based on degree (*k*-core). Nodes are recursively removed based on a degree threshold. The remaining nodes form a subgraph or core where all nodes have a within-degree above the threshold. For example, the 3-core of the figure corresponds to a subgraph where all nodes have a degree of 3 or more. The numbers on the circles correspond to nodes' degree. The right plot shows the number of remaining nodes in *s*-core after applying the strength-based threshold s. **B)** Brain regions identified using the *s*-core decomposition. Three categories were defined, considering a range of s values: S_3 (n = 10 nodes), S_2 (n = 56) and S_1 (n = 24). **C)** Changes in synchrony $\bar{R}$, global efficiency E^w and clustering coefficient Q^w when neuromodulating 24-node sets containing the S_3 nodes (blue), S_1 nodes (olive green) or only S_2 nodes (orange). S_1 and S_3 sets were complemented with random nodes from S_2 to obtain sets of 24. Results are shown as the difference with respect to a random subset of nodes of equal size (null case). The bottom row summarizes the area under the curve (AUC) for each metric and nodal category, averaged over the 10 random seeds. Shaded areas correspond to 95% confidence intervals, and bar plots were built using the mean $\pm$ standard deviation. ***: $p < 0.001$.

Brain regions	Rich Club	S_3 core	Top strength
Posterior cingulate gyrus (L, R)	X	X	X
Precuneus (L, R)	X	X	X
Calcarine fissure (L, R)		X	X
Cuncus (L, R)		X	
Cuneus (L, R)		X	X
Caudate nucleus (R)	X		
Hippocampus (L, R)	X		
Insula (L)			X
Middel occipital gyrus (L)	X		X
Pallidum (L, R)	X		
Putamen (L, R)	X		X
Rolandic Operculum (L)			X
Superior dorsal gyrus, dorsolateral (L, R)	X		
Superior frontal gyrus, orbital (L)			X
Superior occipital gyrus (L, R)			X
Superior frontal gyrus, medial (L)	X		X
Thalamus (L, R)	X		

Table 6.1: List of regions belonging (X) to the rich club, the S_3 category, and the 17 nodes with highest strength. L: left hemisphere; R: right hemisphere. The regions listed here are the same displayed in the glass brains of Fig. 6.5 and Fig. 6.6.

(Garas et al., 2012; Eidsaa and Almaas, 2013) that classifies nodes according to their core-periphery organization (Hagmann et al., 2008) (Fig. 6.6A). I defined three categories considering a range of critical s-core values: S_3 with 10 nodes ($1.54 < s < 1.78$), S_2 with 56 nodes ($1.48 < s < 1.54$), and S_1 with 10 nodes ($s < 1.48$) (Fig. 6.6B). The critical *s*-core is defined as the maximal value of s at which nodes are still connected to the network. Thus, S_3 are nodes connected within them with highest strength, S_2 middle-strength nodes, and S_1 the nodes with the lowest strength. The S_3 subset comprises the brain regions shown in Table 4.

I simulated the neuromodulation in subsets of 24 nodes, containing either the S_3 or the S_1 category, and complementing with 14 random nodes from S_2 as done with the rich club. A third group was built with 24 nodes from S_2, and all groups were compared to a random selection of 24 nodes from the whole set. As shown in Fig. 6.6C, the selection of S_2 nodes for neuromodulation shows the largest effect in $\Delta\bar{R}$, ΔE^w and ΔQ^w, compared with S_1 nodes ($p < 0.001$ using Student's t test) and compared to the selection of S_3 nodes ($p < 0.001$, except for ΔE^w with

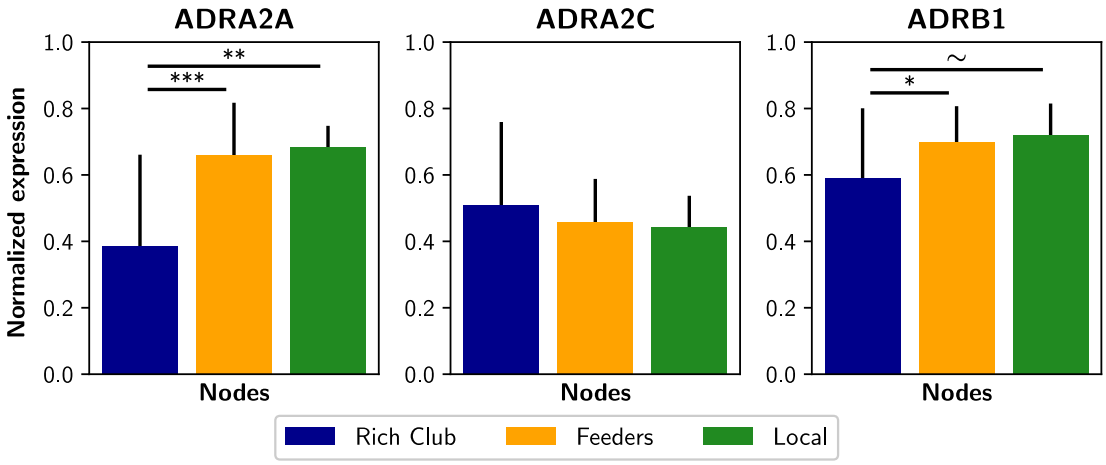

Figure 6.7: Expression of some noradrenergic receptors genes in brain regions. Genes ADRA2A, ADRA2C and ADRAB1 are related to noradrenergic receptors α_{2A}, α_{2C} and β_1, respectively. The normalized expression was obtained from the Allen Human Brain Atlas using the AAL parcellation. Bar plots were built using the mean $\pm$ standard deviation. ***: $p < 0.001$, **: $p < 0.01$, *: $p < 0.05$, $\sim$: $p < 0.1$.

$p = 0.106$). Thus, nodes belonging to the highest *s*-core (nodes of the highest within-strength sub-network) do not behave like the rich club, as their neuromodulation does not have the highest impact on network synchronization and integration/segregation properties.

The non-uniform expression of receptors across several brain areas suggests that the brain uses selective or partial neuromodulation. Surprisingly, using the Allen Human Brain Atlas database (Shen et al., 2012) I found that some adrenergic receptor genes, i.e., the ADRA2A and ADRB1, are less expressed in the rich club nodes than in feeders and local nodes (Fig. 6.7). As a consequence, the noradrenergic-mediated increase in filter gain could have a lower impact on rich club nodes.

6.4 SUMMARY

I found that when I selectively neuromodulated the brain regions by the rich club (meso-scale property) or the high strength criteria (local-scale) the whole-brain network dynamics is most effectively modified. Specifically, those regions facilitate the transition towards more functional integrated brain states. Additionally, I observed that surrogate connectomes reduced FC richness

compared with human SC when neuromodulated. The findings clarify how the neuromodulation interacts with the anatomical network features at local-, meso-, and macro-scale levels in a whole-brain model to facilitate switching between segregated and integrated brain states.

Chapter 7

Discussion

In this dissertation, I studied how the cholinergic and noradrenergic systems manage the transitions between different FC patterns. Specifically, I started from the hypothesis and mechanisms proposed by Shine (2019). In his work, the author proposed that aceylcholine and noradrenaline promote more segregated and integrated functional network topologies, respectively. For testing this hypothesis, I employed a whole-brain model based on Jansen & Rit neural masses interconnected using a human connectome. I found that the framework proposed by Shine (2019) might be true in the "consequences", but maybe not in the "causes". Specifically, I found a pro-segregation effect, ascribed to cholinergic system, using different biophysical mechanisms (Deco et al., 2014; Pfeffer et al., 2021) as the suggested initially by Shine (2019). The simulations showed that, at the macro-scale, acetylcholine and noradrenaline promote opposite (segregated vs integrated) network topologies. Next, using empirical fMRI data, I tested if the mechanisms reproduce the model predictions related to cholinergic system. Indeed, both the simulated and empirical data conveyed the same message: acetylcholine promotes segregation, but the effect is context-dependent.

The last part of this thesis is an attempt to link the features of SC with neuromodulatory systems. Employing a selective noradrenergic neuromodulation, I found that the global organization of the connectome sustains rich metastable and partially synchronized states, essential to the effects related to acetylcholine and noradrenaline. I observed that the brain hubs –regions with high strength or belonging to the rich club– are the best targets that, when neuromodulated, shift the brain dynamics towards integration.

The main result of my thesis relies on the mechanisms employed, by the neuromodulatory systems, to allow the transition from more segregated to integrated functional states (and viceversa). Moreover, the principal result consisted in the context-dependent effects of cholinergic neuromodulation on FC. Although this effect was reported using MEG data (Pfeffer et al., 2021), my work was the first that combines experimental fMRI BOLD recordings, computational modeling and

data analysis using tools from graph theory. In the next sections, I will discuss the meaningfulness of the results based on the current literature.

7.1 MECHANISMS OF ACTION FOR SIMULATING NEUROMODULATION

Here, the plausibility of the model employed in this work is briefly commented. The manipulation of the input-output function of neural populations was employed in many whole-brain models to simulate neuromodulation (Deco et al., 2018; Shine et al., 2018a; Herzog et al., 2020; Kringelbach et al., 2020; Luppi et al., 2021b; Pfeffer et al., 2021). In the case of the work of Shine et al. (2018a), using FitzHugh-Nagumo neural masses coupled with a hemodynamic model, functional segregation and integration were studied from the fMRI BOLD FCs. They found that the increase of the neural gain (conceptually the same as filter gain) produces a transition from functional segregation (high modularity) to integration (high participation coefficient and global efficiency). Also, the increase in integration was hand in hand with an increment of the phase synchrony of the faster neural oscillations (the direct output of the neural mass model). Thus, my results are in line with the increment in functional integration, triggered by noradrenaline through filter gain, found in Shine et al. (2018a). The gain of excitatory neural populations was also used to model the effects of LSD in a whole-brain model (Deco et al., 2018; Herzog et al., 2020; Kringelbach et al., 2020), which reflects, principally, the action of the serotonergic system. We can expect that, similar to Shine et al. (2018a), the LSD might promote functional integration. Surprisingly, a work from Luppi et al. (2021a) suggests that LSD can shift the brain dynamics towards a more segregated functional network topology. The authors reported an increment in clustering coefficient, measured over the static FC matrices, and also over the integrated and segregated substates obtained through the cartographic profile and k-means clustering, i.e., by computing integration and segregation using sliding windows. This discrepancy, between the effects of LSD (Luppi et al., 2021a) and pro-noradrenergic drugs (Coull et al., 1999; Shine et al., 2018a,b; Pfeffer et al., 2021) on functional network topology, emphasizes the necessity of finding more specific mechanisms of action for neurotransmitters and neuromodulators. In short,

what mechanisms can be ascribed to each neuromodulatory system, and what are the expected effects of specific neuromodulators on FC and brain dynamics? For example, while is it thought that acetylcholine and noradrenaline have an effect on increasing neural gain, the opposite was reported for serotonin (Ferguson and Cardin, 2020), which in fact contradicts the mechanisms described in Deco et al. (2018) for modeling the effects of LSD.

Moving in the opposite direction, the reader may think: what should be the effect of manipulating the neural gain of inhibitory neural populations? This issue was recently addressed in Luppi et al. (2021b), using a whole-brain model to simulate the effects of anesthesia through mechanisms that depend on GABAergic receptors. The anesthesia condition was simulated increasing the gain –slope of the input-output function– of the inhibitory neurons populations, as a function of the distribution of $GABA_A$ receptors. They found that the mechanism not only reproduced the effects of anesthesia –specifically the FCD under anesthesia–, but also they observed that the expression of the $GABA_A$ receptors was fundamental for explaining the effect of anesthetics. This case is worth to be commented, because the manipulation of the neural gain of inhibitory populations was used to put the model in a completely opposite state of consciousness, in comparison with the higher arousal levels that the noradrenergic system is supposed to support (Aston-Jones and Cohen, 2005; Shine et al., 2016, 2018b). In fact, a reduction of small-world propensity (a measure of segregation/integration balance), was reported under the effects of deep propofol anesthesia (Luppi et al., 2019).

The mechanisms employed here are compatible with previous computational models, which attempted to simulate the effects of acetylcholine on global brain dynamics (Deco et al., 2014; Nghiem et al., 2020; Pfeffer et al., 2021). In previous works, a decrease in global coupling and spike-frequency adaptation has been proposed to simulate the influence of acetylcholine in the transition from sleep to wakefulness (Deco et al., 2014; Nghiem et al., 2020). A similar mechanism was proposed by Pfeffer et al. (2021), who simulated the effects of acetylcholine by increasing the neural (filter) gain and decreasing global coupling. The main difference in my model was to reduce the feedback inhibition as an effect of nicotine, in contrast with the increment in neural gain used in Pfeffer et al. (2021). However, a reduction of feedback inhibition, at the level of single neuron

networks, can produce an increase in the neural responses of the entire network (Ferguson and Cardin, 2020; Pfeffer et al., 2021). For that reason, this mechanism could be compatible with the increase in neural gain proposed in Pfeffer et al. (2021). Also, in all the aforementioned models (including the one presented in my work), the increase in segregation was compatible with the reduction in global coupling by the cholinergic system. Indeed, the mechanisms are in accordance with the shift from internal to external processing of information within the brain by acetylcholine (Honey et al., 2017), as a consequence of reducing the influence of feedback connections in relation to external stimulation.

I showed that the effects of nicotine are context-dependent, an issue that will be more extensively discussed in the **Nicotine Context-Dependent Effects on Functional Connectivity** section. As future work, it could be interesting to corroborate the results presented by Coull et al. (1999), Shine et al. (2018b) and Pfeffer et al. (2021), related to the noradrenergic system. In that line, fMRI data and computational modeling could be used to study if the biophysical mechanisms proposed for noradrenaline –specifically, the increase in filter gain–, can reproduce the context-dependent effects of noradrenergic system on whole-brain FC.

Despite the main objective in this dissertation being to study the effects of neuromodulation on functional network topology, starting from fMRI BOLD time series, the neural mass model can be employed to gather some ideas about the possible effects of neuromodulators on a faster time-scale. For example, the results in Fig. 4.2, Fig. 4.5 suggest that the shift from segregation to integration happened together with an increase in the global phase synchrony of the EEG-like signals. The cholinergic shift to segregation produces a decrease in phase synchrony, while the noradrenline-mediated transition to integration produces the opposite result. This was in line with the effects of atomexetine and donepezil reported by Pfeffer et al. (2021), using MEG data. Another outcome of the neural mass model was the change in the alpha/theta ratio by neuromodulation. Acetylcholine increases (decreases) the relative power of alpha (theta) oscillations (Fig. 4.2 and Fig. 5.11), contrary to the effects ascribed to noradrenaline in my simulations (Fig. 4.5). The implications of these results will be commented below.

In a computational model to reproduce the transition from wakefulness to sleep (Deco et al.,

2014), the decrease of acetylcholine levels produced an increment of the power of the slower neural oscillations. Some studies reported an increase of alpha oscillations with donepezil and nicotine, and a decrease with scopolamine (Lozano-Soldevilla, 2018), an inhibitor of muscarinic acetylcholine receptors. Also, in Alzheimer disease, a signature of the pathology is the widespread increment of theta oscillations, and a decrease of alpha power, in particular in the posterior EEG scalp regions (Babiloni et al., 2016; Nakamura et al., 2018). Interestingly, one particular feature of Alzheimer disease is the impairment of cholinergic neuromodulation (Hampel et al., 2019). In that line, acetylcholinesterase inhibitors, such as donepezil, effectively recover the normal EEG rhythms in patients with Alzheimer (Babiloni et al., 2013).

The results presented in this work, pointed out that noradrenaline has a role in promoting functional integration, which constitutes one of the findings of Shine (Shine et al., 2016, 2018b,a; Shine, 2019), and also facilitates the synchronization of neural activity in faster time-scales (derived from my results). If that was the case, the increment in synchronization, in the neural mass model presented here, befalls with the reduction of alpha/theta relative power ratio (see for example Fig. 4.5). It was shown that atomoxetine has clinical efficacy to treat ADHD (Childress, 2016). A particular feature of ADHD is the increment of the power of the slower theta oscillations (Lenartowicz and Loo, 2014). It has been reported that atomoxetine can ameliorate the EEG abnormalities observed in ADHD (Barry et al., 2009). Considering that atomoxetine should “boost” the overall levels of noradrenaline in the brain, the results of the model contradicts those empirical observations, that is, a raise in alpha power (or a reduction of the theta power) was expected when increasing the filter gain to simulate the effects of noradrenaline. In contrast, I found the inverse result. However, some reports challenge this view of increased theta power in ADHD (Buyck and Wiersema, 2015).

The focus of my work relies on the effects of neuromodulation on fMRI BOLD FC. Even so, trying to interpret the outputs of the neural mass model constitutes, in my personal opinion, a temptation that is difficult to avoid. The drop off of oscillatory frequency its a consequence of neural synchronization. This effect was observed in a different neural mass model (Shine et al., 2018a), used to simulate fMRI BOLD-like signals. However, I want to deliver a more simple message.

The most concrete conclusion that could be obtained, through the neural mass model, is that acetylcholine and noradrenaline produced opposite effects in synchronization: the un-coordination and coordination of the EEG-like signals, respectively. That result constitutes another way of conceptualizing segregation and integration, and is compatible with the results obtained using the fMRI BOLD-like time series.

All the commented results, related to the EEG-like signals, should be interpreted with caution. They constitute possible predictions of the model, but, in contrast with the simulations comprising fMRI BOLD time series, an empirical test bench for EEG/MEG was not considered here. Also, the neural mass model employed has some limitations. First, brain regions consist of homogeneous neural masses (same parameters for all nodes). Effectively, an improvement in model fitting was reported using regional heterogeneity in a whole-brain model (Deco et al., 2021a), in comparison with its homogeneous version. Second, the original Jansen & Rit model has a limited oscillatory frequency bandwidth which, usually, is between the delta and alpha ranges of the EEG spectrum. More complex models, such as the one proposed by Wendling et al. (2002), can reproduce the faster signatures of the EEG recordings, for example, beta and gamma oscillations.

7.2 NEUROMODULATORY INFLUENCE ON BRAIN FUNCTIONAL CONNECTIVITY DYNAMICS

Simulated data shows that both cholinergic and noradrenergic neuromodulation moves the system –the whole-brain model– from a dynamical rich regime to a more restricted one. Also, the points in the parameter space where the model better reproduces the empirical FC, correspond to the points in which the model exhibits more complex dynamics, i.e., higher multistability (standard deviation of the FCD) or topological variability (standard deviation of integration and segregation). Several works suggest that, in RS conditions, the brain maximizes its dynamical repertoire (Cabral et al., 2014; Zamora-López et al., 2016; Foster et al., 2016; Shine et al., 2016, 2019; Fukushima and Sporns, 2020; Wang et al., 2021a). At rest, integration and segregation are

balanced, and functional complexity is higher as possible (Zamora-López et al., 2016; Wang et al., 2021a). RS condition can be conceived as a collection of “building blocks” (Leonardi et al., 2013), corresponding to several FCs patterns that might be observed in different behavioral contexts. From RS, the brain can “assembble” a new brain state, through neuromodulation, using the available collection of blocks. Selecting fewer and appropriate blocks, for a particular context, will reduce the temporal variability of FC, in comparison with the RS condition. Thus, from RS a change in brain dynamics can be easily achieved by neuromodulators, changing the blocks that constitute the foundations of the brain’s FC.

Both acetylcholine and noradrenaline, in the simulated data, decreased the dynamical richness with respect to the RS condition. However, they did it in different ways: While noradrenaline produces a decrease in FCD speed, acetylcholine has the opposite effect. A decrease in FCD speed is a signature of more correlated and stable FC patterns over time, something expected when the global correlations are higher. It is possible for this stability of FCs fluctuations to be desired in very changeling and complex tasks, when the activity of several brain networks must be coordinated to generate a coherent behavioral outcome. The works of Shine et al. (2016) and Wang et al. (2021a) showed, using experimental data, that integrated states are less variable over time, and more likely to be dynamically integrated (less time expended in segregated functional states). Another possibility is that the increment in global correlations, mediated by noradrenaline, is a consequence of prioritizing the internal priors (previous knowledge) over the external stimuli (the sensory information). Internal priors could be used when top-down control of information processing was required, e.g., when subjects performed mental calculations or in working memory tasks.

The influence of acetylcholine on dynamics appears to be the opposite of noradrenaline. Dynamics become faster when increasing the levels of acetylcholine in the simulations. Similar to Wang et al. (2021a), the cholinergic rearrangement to segregation reduces the transition between segregated and integrated states, that is, the system spends more time in segregated configurations, and global correlations are reduced. The shift to segregation could be a consequence, both in the model employed by Wang et al. (2021a) and the one presented in my

work, of decoupling brain regions. As mentioned before, the effect of acetylcholine in reducing global correlations, by decoupling brain areas, is compatible with the switch of the brain from being driven by internal information to external inputs. (Honey et al., 2017). This switch might reduce the influence of internal priors for effectively extracting the relevant features of the external stimuli.

Using the simulated data, I reproduced some possible hypothetical effects of nicotine on the faster EEG-like signals (Fig. 5.11). Specifically, nicotine decreased the global phase synchrony, and raised the firing rates of the neural masses' pyramidal neurons. Also, nicotine incremented the statistical dimensionality of the EEG-like and BOLD-like FCs. What are the implications of these changes mediated by nicotine? A possible explanation was provided by Ito et al. (2020). Using both empirical and simulated data, they showed that, during a task, the brain activity becomes more "quenched", that is, less variable. The task, by itself, moves the averaged firing rate at the right of the sigmoid transfer function. In consequence, the outputs of neural masses will be closer to the saturated range of the function, where the effective slope is lower, and output responses will be more narrowed (quenched). In effect, my simulations show that both the task and nicotine raise the firing rates of pyramidal neurons (Fig. 5.11D). As suggested by Ito et al. (2020), a lower effective slope produces a decrease of the overall output variability, as well as a reduction in shared variability (e.g., global correlations) of connected brain regions. This explains why the task, by itself, brings down the global correlations. On the other hand, the increase in EEG and BOLD dimensionality (Fig. 5.11E-F) could reflect an improvement in information representations (Ito et al., 2020), that is, the brain prioritizes information processing by halting background spontaneous activity, also reducing global correlations. Again, this is compatible with the hypothesis of the nicotine-mediated switch to the externally-driven processing of information (Honey et al., 2017). Interestingly, I found that global correlations are reduced, while statistical dimensionality is increased by nicotine in the simulated EEG-like and BOLD-like recordings, finding a common result in two different timescales of brain activity.

I demonstrated that neuromodulation decreases dynamical richness in RS, promoting more integrated or segregated regimes of activity over time. The neural mass model predicts, as

possible effects of nicotine, a quenching in brain dynamics, which might change the priority of the brain to a more externally-focused processing of information. As a whole, my results describe how the changes in functional integration and segregation impact brain dynamics and neural variability.

7.3 NICOTINE CONTEXT-DEPENDENT EFFECTS ON FUNCTIONAL CONNECTIVITY

Both empirical and simulated data showed that nicotine decreases the global correlations strongly during the task, and produces a shift to a more segregated functional network topology (not observed in RS). This dissociation has been previously reported as well for the noradrenergic system (Shine et al., 2018b; Pfeffer et al., 2021). The stronger effect of nicotine on global correlations during the task might be a consequence of an interaction between the task and nicotine. If we expect that the task by itself promotes the release of endogenous acetylcholine (Lohani et al., 2020), then nicotine could amplify the effect of cholinergic modulation by directly binding to nicotinic receptors or by promoting the release of more acetylcholine (Nordberg et al., 1989).

On the side of FC topology, the task promotes a more segregated functional network topology (see Fig. 5.1 and Fig. 5.7), and this increase in segregation is enhanced by the effects of nicotine. In the model, the heterogeneous increase in background input –to mimic the effects of the task– acts as a mechanism of network control (Gu et al., 2015), driving the network to a more functionally segregated state without any change in the brain SC. From this point, nicotine might produce a higher contrast with the placebo condition, a fact that is reflected in the reduced integration and increased segregation observed with nicotine.

The results suggest that nicotine promotes segregation during the task, and the degree of segregation correlates with in-task performance (Fig. 5.1B). In contrast, it has been well established that integration is associated with better performance in a wide range of behavioral tasks (Shine and Poldrack, 2018). However, segregation might be a convenient feature in more relatively simpler, monotonous or “automatic” motor tasks (Shine and Poldrack, 2018). This

was proposed by Cohen and D'Esposito (2016), arguing that relatively simpler tasks require the coordination of few brain subnetworks, and in this case a segregated network topology would be desirable for an optimal in-task performance. For example, enhanced segregation was reported in motor learning (Bassett et al., 2015), visual-attentional (Wang et al., 2021b) and sustained attention tasks (Zuberer et al., 2021). In the specific case of Zuberer et al. (2021), segregation increases in task-related networks (e.g. salience, cingulo-opercular, dorsal attention and visual networks), while integration jumps up in brain regions not involved in the task (auditory and sensorimotor networks). The increase in segregation might prevent the cross interference between brain networks, allowing the precise processing of task-relevant information within the brain. On the other hand, the local increment of integration could constitute a mechanism of top-down suppression, through network integration, of regions not relevant for the task (Zuberer et al., 2021). The role of the cholinergic system in selectively decoupling brain regions, to process in a more efficient way external stimuli, is in accordance with the cholinergic shift to functional segregation during the task (Shine, 2019).

Considering the effect of acetylcholine in enhancing attention in visual-spatial tasks (Klinkenberg et al., 2011; Picciotto et al., 2012; Thiele and Bellgrove, 2018), it is plausible to think that acetylcholine promotes segregation increasing the within and between network connectivity in regions involved in visual processing. I checked this possibility with an exploratory analysis, and measured the empirical change (nicotine - placebo, task block) in the nodal clustering coefficient, grouping also the brain regions in the commonly known RS networks (Beckmann et al., 2005). I found that nicotine strongly increases the mean clustering coefficient of nodes within the visual and extrastriate networks. This result is in line with the task-triggered increase in segregation reported by (Zuberer et al., 2021), where the increment in segregation was observed in regions involved in visual processing and attention. Furthermore, my results resonate with the work of Kowalczyk et al. (2018), where a long-term entrainment in a visual-attentional task promotes changes in brain SC, comprising an increase of within and between connectivity in occipital and parietal brain regions, both required for processing visual information. Topologically, they found an increase in local efficiency (segregation) within the occipito-parietal network. This case is interesting because

the change in network topology, which also was non-transient (long-standing), might comprise plasticity changes in the SC that enhance the bandwith of communication between and within occipital and parietal regions (Kowalczyk et al., 2018). The cholinergic system could play a similar role mediating transient changes in network topology, changes that facilitate the processing of visual information from noisy signals.

I found a negative correlation between the nicotinic $\alpha_4\beta_2$ receptor density, obtained by PET, and the change in FC nodal strength. In fact, this results should not be a surprise, considering that FC changes were analyzed under the effects of nicotine. Despite this, the results emphasize that the changes observed in FC can be ascribed to cholinergic system and, more specifically, to nicotinic receptors. The nicotinic $\alpha_4\beta_2$ receptor has a prominent role in attention and cognition (Hasselmo and Sarter, 2011). For example, a dysfunction in $\alpha_4\beta_2$ receptors is associated by cognitive impairments in mild Alzheimer's dementia (Sabri et al., 2018). Also, stimulation of $\alpha_4\beta_2$ receptors enhances performance in visual attentional tasks (Ueno et al., 2002; Howe et al., 2010), while their selective inhibition produces the opposite results (Ueno et al., 2002). Considering the $\alpha_4\beta_2$ PET density map in the whole-brain model improved the fitting to nicotine condition in the task block, but not in RS. This emphasizes the role of $\alpha_4\beta_2$ receptor in mediating the nicotine-induced changes on FC. However, it is important to remark that the effect of incorporating the map was small, and observed only in the task block. A possible explanation resides in the relatively low correlation between the $\alpha_4\beta_2$ density map with the changes in FC nodal strength (Fig. 5.9A), and/or the small effects of nicotine on FC in RS, in comparison with the task (Fig. 5.1A and Fig. 5.7C). On the other hand, I found that the optimized SC nodal strength correlates with the changes in FC. In that case, the brain SC could play a pivotal role in setting the changes in FC by nicotine, specially in the RS condition. There are some theoretical works arguing that the nodal properties, derived from the SC, better explains the effects of neuromodulation on brain dynamics (Shine et al., 2018a; Herzog et al., 2020; Coronel-Oliveros et al., 2021a). In consequence, it is plausible to think that the interaction between SC, neuromodulatory systems (and their receptors) and FC is not straightforward.

Another interesting result was the absence of correlation between overall FC and RT and,

in parallel, the negative one that I found between segregation and RT. Although one of the main effects of nicotine, considering my results, was to decrease the global correlations (overall FC), the change in network topology better predicts the performance of the subjects in the Go/No-Go task, rather than difference in global correlations. Also, the FC network topology during the task was meaningful to predict in-task performance, in opposition to the RS FC network topology. Thus, my findings suggest that 1) network topology matters to predict in-task performance; and 2) as pointed out by Pfeffer et al. (2021), a characterization of RS FC is not enough to explain the effects of neuromodulatory systems on behavior and network topology. Following this idea, a context-dependent effect of noradrenrgic neuromodulation was reported by Shine et al. (2018b). The authors found an increase of RS segregation triggered by atomoxetine (a noradrenaline reuptake inhibitor); the opposite results were observed during a N-back task: atomoxextine increases integration. They suggest that the cognitive load of the N-back, in comparison with the lack of cognitive constraints during RS, enhances locus coeruleus phasic firing patterns, which might be potentiated by atomoxetine, and finally promotes brain functional integration.

There are plenty of ideas to explore starting from this work. For example, the mechanisms employed here could be adapted to simulate the effects of the cholinergic system in the transition from sleep to wakefulness, similar to Deco et al. (2014) and Nghiem et al. (2020). Also, whole-brain models could be used to test specific targets for pharmacological treatments (Deco et al., 2018). By combining patients fMRI, structural and neurotransmitter PET data, personalized whole-brain models can be used to find specific targets for brain disorders. This could inspire new treatments for conditions in which the cholinergic system is impaired, such as Alzheimer disease and the cognitive decline caused by aging (Schliebs and Arendt, 2011). From a more theoretical motivation, I considered just pairwise interactions in my analysis, neglecting high-order effects that might contain relevant information related to high dimensional functional brain interactions. Information theory (Rosas et al., 2019) and algebraic topological approaches (Battiston et al., 2020), may provide useful information about the high-order interdependencies in the brain. In fact, a whole-brain model was proposed as a non-linear model of neurodegeneration for simulating the ageing of connectomes (Gatica et al., 2021b), which was shown to successfully reproduce the

high-order changes observed in neuroimaging data (Gatica et al., 2021a), specifically, a significant increase in redundancy-dominated interdependencies between BOLD activity in older subjects. In this scenario, it could be interesting to revert the ageing-triggered increment in redundancy by simulating the effect of cholinergic neuromodulation in a whole-brain model.

There are some limitations in modeling the effects of nicotine on the FC during the task, and also in ascribing the changes on FC, driven by nicotine, to the entire cholinergic system. First, nicotine is not a full pro-cholinergic drug, such as donepezil, galantamine and rivastigmin, which are cholinesterase inhibitors. However, nicotine can promote the release of acetylcholine (Nordberg et al., 1989), which is plausible considering that nicotinic receptors are widely expressed in several neuron types, including cholinergic neurons (Marchi and Grilli, 2010). Furthermore, the decrease in global correlations by nicotine, reported here, was also observed under the effects of donepezil (Pfeffer et al., 2021). Considering those points, I believe that the generalization, that is, to associate the influence of nicotine with the pro-segregation effects of the cholinergic system (Shine, 2019), constitutes a solid statement. A second limitation consists in the sources of empirical SC and the PET density maps, which do not belong to the same subjects of the empirical fMRI recordings used in this work. I partially solved this problem with the SC optimization, following Deco et al. (2019). However, in the ideal scenario MRI, PET and fMRI data should belong to the same subjects.

Overall, my results propose mechanisms to explain the pro-segregation effects of the cholinergic system, mechanisms compatible with previous computational models. This is the first work, to my knowledge, that combines empirical fMRI data, in-task performance and computational modeling to study the effects of the cholinergic system on network topology. Establishing links between neuromodulation and its functional correlates have great scientific potential to deepen our understanding of the brain and its response depending on the context, and more generally to shed new light on the complex interrelationship between the structure and function of the human brain.

7.4 INTERACTION BETWEEN STRUCTURAL CONNECTIVITY AND NEUROMODULATION

It is possible that the brain employs neuromodulators' receptors heterogeneity to produce more specific changes in FC. In that way, computational models suggest that heterogeneous expression of brain receptors can better explain the brain dynamics under the effect of neurotransmitters and neuromodulators (Deco et al., 2018; Kringelbach et al., 2020; Luppi et al., 2021b). Complementary, there is a large support of the role of the SC in shaping brain's FC (Suárez et al., 2020), evidence also underpinned by computational models (Deco et al., 2017; Castro et al., 2020; Fukushima and Sporns, 2020; Herzog et al., 2020). At a more local level, there are key regions that facilitate the switching between different functional states (Deco et al., 2017; Shine et al., 2018a; Deco et al., 2021b), and also these key regions are more likely to be neuromodulated (Shine et al., 2018a). In this subsection, I will discuss how the brain SC's macro-scale properties sets the basis for the action of neuromodulators, and then discuss the possible role of the brain hubs –the aforementioned key regions– in guiding the changes in FC driven by neuromodulation.

I found that the whole-brain model exhibits over-synchronized behavior when using surrogate connectomes, restricting the dynamic features of the model. This result is in the same line as other previous findings (Cabral et al., 2014; Zamora-López et al., 2016; Wang et al., 2019; Fukushima and Sporns, 2020). Here, I show this behavior in the (α, r_0) parameter space, where simulations with randomized connectomes show either incoherent or over-synchronized activity. Using a whole-brain model to simulate and fit magnetoencephalography (MEG) resting-state recordings, Cabral et al. (2014) found not only that randomized and homogenized versions of the human structural connectivity did not fit empirical data; moreover, they found that the fit was maximal in the metastable region of the parameter space, when unsynchronized (segregated) and synchronized (integrated) regimes of activity coexist. In the same way, Fukushima and Sporns (2020), using more complex surrogate data in the context of whole-brain models, found features of the human connectome that better capture the dynamic fluctuations in fMRI resting-state recordings. Additionally, computational studies conducted by Zamora-López et al. (2016) showed that the human connectome maximizes functional complexity in fMRI recordings,

compared with different surrogate connectomes. Finally, Wang et al. (2019) analyzed how the hierarchical modular structure of the human connectome enables the coexistence of segregated and integrated functional states, also with the use of network surrogates in which hierarchical levels were controlled. My study interpreted the explorations of the parameter space as levels of neuromodulation, that allow the brain to tune its integration or segregation levels to environmental demands. However, neuromodulation cannot bring back a dynamically rich regime to a network without a structural connectome that sustains it.

At the local level, the effects of neuromodulation strongly depend on the characteristics of the nodes in the human connectome. In my model, the nodes with high strength are the ones that better facilitate functional integration when neuromodulated. This result resonates with a recent work by Herzog et al. (2020), who studied a whole-brain model fitted to reproduce the effects of lysergic acid diethylamide (LSD) in resting-state brain dynamics. In their model, the serotonergic-induced changes in nodal entropy correlated positively with node strength. Notably, the correlation disappears when the human connectome is randomized without preserving the strength distribution, emphasizing the importance of the specific organization of the human connectome in shaping brain dynamics. Interestingly, the entropy changes described by Herzog et al. (2020) are poorly explained by the $5HT_{2A}$ receptor density map, obtained by PET (Beliveau et al., 2017), and depends on both node strength and receptor density. Thus, the interaction between the structural connectivity, receptor density and neuromodulation is not straightforward. A similar complex picture may arise if my results are contrasted with receptor maps of noradrenergic receptors.

Network hubs, or nodes belonging to the rich club or network's ignition core, can be critical elements for binding information of segregated brain regions, that is, to integrate information across brain areas (Castro et al., 2020; Griffa and Van den Heuvel, 2018). Considering the relevance of integration for the brain function (Tononi, 2004), and the noradrenergic influence on integration (Shine, 2019), I hypothesized that anatomical network hubs are pivotal elements for promoting functional network integration. My results confirmed this hypothesis, being the neuromodulation of rich club nodes the one that most effectively facilitates functional integration

and synchronization of brain activity. This result agrees with findings reported in a fMRI resting-state model of the brain by Deco et al. (2017), where removing the rich club nodes causes a larger decrease in integration compared to the removal of the non-rich club members. Similar results have been found in computational models of noradrenergic neuromodulation, where rich club nodes are strongly neuromodulated causing functional networks to switch from segregation to integration (Shine et al., 2018a).

Notably, neuromodulation of nodes belonging to the critical *s*-core (the maximally interconnected core) does not promote integration as the rich club nodes do. Both meso-scale analyses rely on sets of nodes organized with strong connection weights. However, they do it differently. The rich club coefficient threshold is based on degree, and rich club members are highly connected between them as well as with the non-rich club members. In contrast, the *s*-core decomposition finds subsets of nodes highly interconnected at strength s, but not necessarily well connected to the rest of the network. Thus, the whole-network changes are more easily achieved if the nodes to be neuromodulated are highly connected both between them and with the rest of the network. The rich-club organization captures additional information that is missing in the local (weight) analysis. For example, the 17 rich club nodes have an overlap of $\approx$ 50% with the 17 highest strength nodes. In contrast, nodes belonging to the S_3 category are the nodes of the highest strength in the network; however, they cannot boost functional integration to the same extent as the rich club nodes.

Part of the brain regions I found in the rich club support high order brain functions. For example, frontoparietal regions play an important role in cognition, and are markedly activated when subjects engage in cognitive tasks (Cavanna, 2007). Precuneus has been associated with consciousness, and a decrease in its activity was reported in sleep, anesthesia and vegetative states (Lückmann et al., 2014). Thalamus, the brain “relay station”, strongly connects several networks that comprise multiple cortical regions (Hwang et al., 2017). Multi-task fMRI recordings in humans suggest a robust role of the anatomical rich club as facilitating elements of functional integration in overall tasks (Shine et al., 2019). An extended analysis and discussion about the role of the rich club, in both health and disease, can be found in Griffa and Van den Heuvel (2018).

As commented before, a selective neuromodulation can be produced through neurotransmitter receptors. In this way, the effect of the noradrenergic system on filter gain may be modeled as proportional to adrenergic receptor expression. Experimentally, the optogenetic activation of the LC in mice increased average functional connectivity, which correlates with the expression of α_2, α_1 and β_1 adrenergic receptors (Zerbi et al., 2019). Thus, a future research avenue in computational models may include a density-dependent noradrenergic neuromodulation with the addition of some receptors maps, obtained by positron emission tomography (PET), or even gene expression maps (Shen et al., 2012) that correlate with receptor density maps (Komorowski et al., 2017). However, using the Allen Human Brain Atlas database (Shen et al., 2012) I found that some adrenergic receptor genes, i.e., the ADRA2A and ADRB1, are less expressed in the rich club nodes than in feeders and local nodes (Fig. 6.7). In consequence, the effect of noradrenline in increasing neural responses could be lower in the rich club regions. It is possible that this reduced expression constitutes a compensation for the high connectivity of rich club nodes, especially considering the higher metabolism of rich regions that exposed them to oxidative stress and neuroinflammation (Griffa and Van den Heuvel, 2018). On the other hand, receptor expression can itself be compensated by a specific sub-cellular localization or other excitability factors that may enhance the effect of noradrenaline.

It has been suggested that the effect of noradrenaline in functional connectivity is context-dependent (Coull et al., 1999; Shine et al., 2018b; Pfeffer et al., 2021). In that line, modeling the effect of noradrenaline in resting-state and task conditions could untangle the mechanisms behind this context-dependent effect of noradrenaline. The anatomical backbone and other dynamical parameters of this model can be substituted to study the mouse or monkey brain and to any other species for which the whole-brain white-matter connectivity is available.

My work considers an arbitrary basal value of r_0. Despite this, I reported a clear effect of the selective noradrenergic neuromodulation on functional integration, that is, some brain regions have a greater impact on the noradrenaline-mediated effects on brain function. A further improvement to the approach employed constitutes the use of a different benchmark, e.g., fitting the model to reproduce the empirical FC in resting-state, and then apply a homogenoeus or selective

neuromodulation. Furthermore, the addition of receptor maps may be considered, as commented above.

Overall, my results offer new insights into the key regions of the human brain that, when neuromodulated via the noradrenergic system, promote transitions to integrated functional states. The results highlight the importance of the rich club and high-strength connections in producing changes related to neuromodulation. I hope that the theoretical framework will inspire new research toward clinical applications or treatments of human brain disorders caused by or associated with changes in functional and structural brain connectivity.

Chapter 8

General Conclusions

This dissertation combines computational modeling and empirical data to characterize the effects of cholinergic and noradrenergic neuromodulatory systems, at the whole-brain level, on functional integration and segregation. The main hypothesis consisted in that acetylcholine and noradrenaline promote more segregated and integrated topologies, respectively. A second hypothesis was considered, and consisted in a possible context-dependent effect of cholinergic neuromodulation.

The *Objective 1* was addressed in the first results chapter. There, I showed that the effect of acetylcholine in reducing the global coupling and the local feedback inhibition, in the model, promotes a more segregated functional network topology. Similar to previous works, I also demonstrated that manipulating the filter gain, to simulate the effect of noradrenaline, moves the brain towards functional integration. Further, cholinergic and noradrenergic systems produce opposite consequences on brain dynamics, i.e, a shift to a faster or slower, respectively, switching between functional connectivity patterns.

The *Objective 2* constitutes an empirical validation of the model's predictions, and belongs to the second results chapter. There, using fMRI BOLD recordings, the effects of nicotine on functional connectivity were characterized. In resonance with the previous results chapter, I observed that nicotine decreases global correlations and also produces a shift to functional segregation. In accordance with the second hypothesis, the effects of nicotine are context-dependent, promoting a more segregated topology during an attentional task than in resting-state conditions. The whole-brain model, fitted to the empirical fMRI BOLD data, corroborated these results. At the behavioral level, nicotine has an effect in improving in-task performance, enhancing attention. To complete the story, I found a link between the changes in network topology and behavior, specifically, between the performance and the degree of functional segregation. Overall, in this section I established possible biophysical mechanisms to explain the macro-scale effects of nicotine, and also gave insights on the particular effects of the cholinergic system on functional

connectivity and its impact on behavior.

The interaction between neuromodulation and structural connectivity constitutes the major topic of the *Objective 3*. An *in-silico* noradrenergic neuromodulation was studied in three different scenarios. In the first one, the macro-scale, I observed that the human structural connectivity is essential to support the effects of neuromodulation on brain dynamics, supporting more dynamical richer regimes of activity. In the second scenario, the local-scale, I observed that the brain regions with high strength and nodal efficiency, more easily facilitate the transition to functional integration. In the last scenario, the meso-scale, I identified some key regions that, when neuromodulated as a whole, produced a strong increase in functional integration. These regions corresponded to the structural rich club, the networks hubs which facilitate the integration of functions of the segregated brain modules and clusters of the brain.

Neuroscience, and in general Biology, is overflowed with an extensive amount of empirical data. For that reason, the synergy between the experiments, mathematics and computational modeling constitutes a way to simplify and synthesize a high dimensional and complex system, as is the brain. Finding universal principles and causal (mechanistic) links might improve our understanding of the brain function.

There are several pathways to follow from this work. An empirical validation of the results using other modalities of brain recordings, such as electro or magnetoencephalography, might be useful for characterizing the effects of neuromodulators on a faster timescale of brain activity. Also, considering that the effects of noradrenaline could be context-dependent, linking possible biophysical mechanisms (e.g., the increase in filter gain) with the experimental data and computational modeling might improve our understanding of how noradrenaline shapes the brain functional connectivity.

Bibliography

Acebrón, J. A., Bonilla, L. L., Vicente, C. J. P., Ritort, F., and Spigler, R. (2005). The kuramoto model: A simple paradigm for synchronization phenomena. Reviews of modern physics, 77(1):137.

Aghourian, M., Legault-Denis, C., Soucy, J., Rosa-Neto, P., Gauthier, S., Kostikov, A., Gravel, P., and Bedard, M. (2017). Quantification of brain cholinergic denervation in alzheimer's disease using pet imaging with [18 f]-feobv. Molecular psychiatry, 22(11):1531–1538.

Allen, E. A., Damaraju, E., Plis, S. M., Erhardt, E. B., Eichele, T., and Calhoun, V. D. (2014). Tracking whole-brain connectivity dynamics in the resting state. Cerebral cortex, 24(3):663–676.

Alonso Martínez, S., Deco, G., Ter Horst, G. J., and Cabral, J. (2020). The dynamics of functional brain networks associated with depressive symptoms in a nonclinical sample. Frontiers in neural circuits, page 60.

Arnatkevicute, A., Fulcher, B. D., and Fornito, A. (2019). A practical guide to linking brain-wide gene expression and neuroimaging data. Neuroimage, 189:353–367.

Askew, C. E., Lopez, A. J., Wood, M. A., and Metherate, R. (2019). Nicotine excites vip interneurons to disinhibit pyramidal neurons in auditory cortex. Synapse, 73(9):e22116.

Aston-Jones, G. and Cohen, J. D. (2005). An integrative theory of locus coeruleus-norepinephrine function: adaptive gain and optimal performance. Annu. Rev. Neurosci., 28:403–450.

Babiloni, C., Del Percio, C., Bordet, R., Bourriez, J.-L., Bentivoglio, M., Payoux, P., Derambure, P., Dix, S., Infarinato, F., Lizio, R., et al. (2013). Effects of acetylcholinesterase inhibitors and memantine on resting-state electroencephalographic rhythms in alzheimer's disease patients. Clinical Neurophysiology, 124(5):837–850.

Babiloni, C., Del Percio, C., Caroli, A., Salvatore, E., Nicolai, E., Marzano, N., Lizio, R., Cavedo, E., Landau, S., Chen, K., et al. (2016). Cortical sources of resting state eeg rhythms are related

to brain hypometabolism in subjects with alzheimer's disease: an eeg-pet study. Neurobiology of aging, 48:122–134.

Baldassarri, S. R., Hillmer, A. T., Anderson, J. M., Jatlow, P., Nabulsi, N., Labaree, D., Cosgrove, K. P., O'Malley, S. S., Eissenberg, T., Krishnan-Sarin, S., et al. (2018). Use of electronic cigarettes leads to significant beta2-nicotinic acetylcholine receptor occupancy: evidence from a pet imaging study. Nicotine and Tobacco Research, 20(4):425–433.

Barry, R. J., Clarke, A. R., Hajos, M., McCarthy, R., Selikowitz, M., and Bruggemann, J. M. (2009). Acute atomoxetine effects on the eeg of children with attention-deficit/hyperactivity disorder. Neuropharmacology, 57(7-8):702–707.

Bassett, D. S., Yang, M., Wymbs, N. F., and Grafton, S. T. (2015). Learning-induced autonomy of sensorimotor systems. Nature neuroscience, 18(5):744–751.

Battaglia, D., Boudou, T., Hansen, E. C., Lombardo, D., Chettouf, S., Daffertshofer, A., McIntosh, A. R., Zimmermann, J., Ritter, P., and Jirsa, V. (2020). Dynamic functional connectivity between order and randomness and its evolution across the human adult lifespan. NeuroImage, 222:117156.

Battiston, F., Cencetti, G., Iacopini, I., Latora, V., Lucas, M., Patania, A., Young, J.-G., and Petri, G. (2020). Networks beyond pairwise interactions: structure and dynamics. Physics Reports, 874:1–92.

Beckmann, C. F., DeLuca, M., Devlin, J. T., and Smith, S. M. (2005). Investigations into resting-state connectivity using independent component analysis. Philosophical Transactions of the Royal Society B: Biological Sciences, 360(1457):1001–1013.

Bedard, M.-A., Aghourian, M., Legault-Denis, C., Postuma, R. B., Soucy, J.-P., Gagnon, J.-F., Pelletier, A., and Montplaisir, J. (2019). Brain cholinergic alterations in idiopathic rem sleep behaviour disorder: a pet imaging study with 18f-feobv. Sleep medicine, 58:35–41.

Beliveau, V., Ganz, M., Feng, L., Ozenne, B., Højgaard, L., Fisher, P. M., Svarer, C., Greve, D. N.,

and Knudsen, G. M. (2017). A high-resolution in vivo atlas of the human brain's serotonin system. Journal of Neuroscience, 37(1):120–128.

Benjamini, Y. and Hochberg, Y. (1995). Controlling the false discovery rate: a practical and powerful approach to multiple testing. Journal of the Royal statistical society: series B (Methodological), 57(1):289–300.

Birn, R. M., Molloy, E. K., Patriat, R., Parker, T., Meier, T. B., Kirk, G. R., Nair, V. A., Meyerand, M. E., and Prabhakaran, V. (2013). The effect of scan length on the reliability of resting-state fmri connectivity estimates. Neuroimage, 83:550–558.

Blohm, G., Kording, K. P., and Schrater, P. R. (2020). A how-to-model guide for neuroscience. Eneuro, 7(1).

Blondel, V. D., Guillaume, J.-L., Lambiotte, R., and Lefebvre, E. (2008). Fast unfolding of communities in large networks. Journal of statistical mechanics: theory and experiment, 2008(10):P10008.

Branco, T. and Häusser, M. (2011). Synaptic integration gradients in single cortical pyramidal cell dendrites. Neuron, 69(5):885–892.

Bullmore, E. and Sporns, O. (2009). Complex brain networks: graph theoretical analysis of structural and functional systems. Nature reviews neuroscience, 10(3):186–198.

Buyck, I. and Wiersema, J. R. (2015). Electroencephalographic activity before and after cognitive effort in children with attention deficit/hyperactivity disorder. Clinical EEG and neuroscience, 46(2):88–93.

Cabral, J., Kringelbach, M. L., and Deco, G. (2017a). Functional connectivity dynamically evolves on multiple time-scales over a static structural connectome: Models and mechanisms. NeuroImage, 160:84–96.

Cabral, J., Luckhoo, H., Woolrich, M., Joensson, M., Mohseni, H., Baker, A., Kringelbach, M. L., and Deco, G. (2014). Exploring mechanisms of spontaneous functional connectivity in meg:

how delayed network interactions lead to structured amplitude envelopes of band-pass filtered oscillations. Neuroimage, 90:423–435.

Cabral, J., Vidaurre, D., Marques, P., Magalhães, R., Silva Moreira, P., Miguel Soares, J., Deco, G., Sousa, N., and Kringelbach, M. L. (2017b). Cognitive performance in healthy older adults relates to spontaneous switching between states of functional connectivity during rest. Scientific reports, 7(1):1–13.

Carlson, J. S., Jensen, C. M., and Widaman, K. F. (1983). Reaction time, intelligence, and attention. Intelligence, 7(4):329–344.

Castro, S., El-Deredy, W., Battaglia, D., and Orio, P. (2020). Cortical ignition dynamics is tightly linked to the core organisation of the human connectome. PLOS Computational Biology, 16(7):1–23.

Cavanna, A. E. (2007). The precuneus and consciousness. CNS spectrums, 12(7):545–552.

Chen, Y., Huang, X., Wu, M., Li, K., Hu, X., Jiang, P., Chen, L., He, N., Dai, J., Wang, S., et al. (2019). Disrupted brain functional networks in drug-naive children with attention deficit hyperactivity disorder assessed using graph theory analysis. Human brain mapping, 40(17):4877–4887.

Childress, A. C. (2016). A critical appraisal of atomoxetine in the management of adhd. Therapeutics and clinical risk management, 12:27.

Clarkson, J. A. (1936). Uniformly convex spaces. Transactions of the American Mathematical Society, 40(3):396–414.

Cohen, J. R. and D'Esposito, M. (2016). The segregation and integration of distinct brain networks and their relationship to cognition. Journal of Neuroscience, 36(48):12083–12094.

Conners, C. K. (1994). The Conners Continuous Performance Test. Toronto: Multi-Health Systems. Inc.

Coronel-Oliveros, C., Castro, S., Cofré, R., and Orio, P. (2021a). Structural features of the human connectome that facilitate the switching of brain dynamics via noradrenergic neuromodulation. Frontiers in Computational Neuroscience, page 61.

Coronel-Oliveros, C., Cofré, R., and Orio, P. (2021b). Cholinergic neuromodulation of inhibitory interneurons facilitates functional integration in whole-brain models. PLOS Computational Biology, 17(2):1–25.

Coull, J. T., Büchel, C., Friston, K. J., and Frith, C. D. (1999). Noradrenergically mediated plasticity in a human attentional neuronal network. Neuroimage, 10(6):705–715.

Deco, G., Cruzat, J., Cabral, J., Knudsen, G. M., Carhart-Harris, R. L., Whybrow, P. C., Logothetis, N. K., and Kringelbach, M. L. (2018). Whole-brain multimodal neuroimaging model using serotonin receptor maps explains non-linear functional effects of lsd. Current biology, 28(19):3065–3074.

Deco, G., Cruzat, J., Cabral, J., Tagliazucchi, E., Laufs, H., Logothetis, N. K., and Kringelbach, M. L. (2019). Awakening: Predicting external stimulation to force transitions between different brain states. Proceedings of the National Academy of Sciences, 116(36):18088–18097.

Deco, G., Hagmann, P., Hudetz, A. G., and Tononi, G. (2014). Modeling resting-state functional networks when the cortex falls asleep: local and global changes. Cerebral cortex, 24(12):3180–3194.

Deco, G., Kringelbach, M. L., Arnatkeviciute, A., Oldham, S., Sabaroedin, K., Rogasch, N. C., Aquino, K. M., and Fornito, A. (2021a). Dynamical consequences of regional heterogeneity in the brain's transcriptional landscape. Science Advances, 7(29):eabf4752.

Deco, G., Van Hartevelt, T. J., Fernandes, H. M., Stevner, A., and Kringelbach, M. L. (2017). The most relevant human brain regions for functional connectivity: Evidence for a dynamical workspace of binding nodes from whole-brain computational modelling. Neuroimage, 146:197–210.

Deco, G., Vidaurre, D., and Kringelbach, M. L. (2021b). Revisiting the global workspace orchestrating the hierarchical organization of the human brain. Nature Human Behaviour, pages 1–15.

Dehaene, S. and Changeux, J. P. (2011). Experimental and Theoretical Approaches to Conscious Processing. Neuron.

delEtoile, J. and Adeli, H. (2017). Graph theory and brain connectivity in alzheimer's disease. The Neuroscientist, 23(6):616–626.

Eidsaa, M. and Almaas, E. (2013). S-core network decomposition: A generalization of k-core analysis to weighted networks. Physical Review E, 88(6):062819.

Ferguson, K. A. and Cardin, J. A. (2020). Mechanisms underlying gain modulation in the cortex. Nature Reviews Neuroscience, 21(2):80–92.

Fino, E., Packer, A. M., and Yuste, R. (2013). The logic of inhibitory connectivity in the neocortex. The Neuroscientist, 19(3):228–237.

Foster, B. L., He, B. J., Honey, C. J., Jerbi, K., Maier, A., and Saalmann, Y. B. (2016). Spontaneous neural dynamics and multi-scale network organization. Frontiers in systems neuroscience, 10:7.

Fukushima, M. and Sporns, O. (2020). Structural determinants of dynamic fluctuations between segregation and integration on the human connectome. Communications biology, 3(1):1–11.

Fuxe, K., Dahlström, A. B., Jonsson, G., Marcellino, D., Guescini, M., Dam, M., Manger, P., and Agnati, L. (2010). The discovery of central monoamine neurons gave volume transmission to the wired brain. Progress in neurobiology, 90(2):82–100.

Garas, A., Schweitzer, F., and Havlin, S. (2012). A k-shell decomposition method for weighted networks. New Journal of Physics, 14(8):083030.

Gatica, M., Cofré, R., Mediano, P. A., Rosas, F. E., Orio, P., Diez, I., Swinnen, S. P., and Cortes, J. M. (2021a). High-order interdependencies in the aging brain. Brain connectivity.

Gatica, M., Rosas, F. E., Mediano, P. A., Diez, I., Swinnen, S. P., Orio, P., Cofre, R., and Cortes, J. M. (2021b). High-order functional interactions in ageing explained via alterations in the connectome in a whole-brain model. bioRxiv.

Gießing, C., Thiel, C. M., Alexander-Bloch, A. F., Patel, A. X., and Bullmore, E. T. (2013). Human brain functional network changes associated with enhanced and impaired attentional task performance. Journal of Neuroscience, 33(14):5903–5914.

Gilbert, C. D., Hirsch, J. A., and Wiesel, T. N. (1990). Lateral interactions in visual cortex. In Cold Spring Harbor symposia on quantitative biology, volume 55, pages 663–677. Cold Spring Harbor Laboratory Press.

Ginestet, C. E., Nichols, T. E., Bullmore, E. T., and Simmons, A. (2011). Brain network analysis: separating cost from topology using cost-integration. PloS one, 6(7):e21570.

González, G. F., Van der Molen, M., Žarić, G., Bonte, M., Tijms, J., Blomert, L., Stam, C., and Van der Molen, M. (2016). Graph analysis of eeg resting state functional networks in dyslexic readers. Clinical Neurophysiology, 127(9):3165–3175.

Griffa, A. and Van den Heuvel, M. P. (2018). Rich-club neurocircuitry: function, evolution, and vulnerability. Dialogues in clinical neuroscience, 20(2):121–132.

Gu, S., Pasqualetti, F., Cieslak, M., Telesford, Q. K., Alfred, B. Y., Kahn, A. E., Medaglia, J. D., Vettel, J. M., Miller, M. B., Grafton, S. T., et al. (2015). Controllability of structural brain networks. Nature communications, 6(1):1–10.

Guan, S., Jiang, R., Bian, H., Yuan, J., Xu, P., Meng, C., and Biswal, B. (2020). The profiles of non-stationarity and non-linearity in the time series of resting-state brain networks. Frontiers in Neuroscience, 14:493.

Guimera, R. and Amaral, L. A. N. (2005). Cartography of complex networks: modules and universal roles. Journal of Statistical Mechanics: Theory and Experiment, 2005(02):P02001.

Hadley, J. A., Kraguljac, N. V., White, D. M., Ver Hoef, L., Tabora, J., and Lahti, A. C. (2016).

Change in brain network topology as a function of treatment response in schizophrenia: a longitudinal resting-state fmri study using graph theory. npj Schizophrenia, 2(1):1–7.

Hagmann, P., Cammoun, L., Gigandet, X., Meuli, R., Honey, C. J., Wedeen, V. J., and Sporns, O. (2008). Mapping the structural core of human cerebral cortex. PLoS Biol, 6(7):e159.

Hallquist, M. N., Hwang, K., and Luna, B. (2013). The nuisance of nuisance regression: spectral misspecification in a common approach to resting-state fmri preprocessing reintroduces noise and obscures functional connectivity. Neuroimage, 82:208–225.

Hampel, H., Mesulam, M.-M., Cuello, A. C., Khachaturian, A. S., Vergallo, A., Farlow, M., Snyder, P., Giacobini, E., and Khachaturian, Z. (2019). Revisiting the cholinergic hypothesis in alzheimer's disease: emerging evidence from translational and clinical research. The journal of prevention of Alzheimer's disease, 6(1):2–15.

Hansen, E. C., Battaglia, D., Spiegler, A., Deco, G., and Jirsa, V. K. (2015). Functional connectivity dynamics: modeling the switching behavior of the resting state. Neuroimage, 105:525–535.

Hansen, J. Y., Shafiei, G., Markello, R. D., Smart, K., Cox, S. M., Wu, Y., Gallezot, J.-D., Aumont, É., Servaes, S., Scala, S. G., et al. (2021). Mapping neurotransmitter systems to the structural and functional organization of the human neocortex. bioRxiv.

Hasselmo, M. E. and Sarter, M. (2011). Modes and models of forebrain cholinergic neuromodulation of cognition. Neuropsychopharmacology, 36(1):52–73.

Herzog, R., Mediano, P. A., Rosas, F. E., Carhart-Harris, R., Perl, Y. S., Tagliazucchi, E., and Cofre, R. (2020). A mechanistic model of the neural entropy increase elicited by psychedelic drugs. Scientific reports, 10(1):1–12.

Hillmer, A. T., Esterlis, I., Gallezot, J.-D., Bois, F., Zheng, M.-Q., Nabulsi, N., Lin, S.-F., Papke, R., Huang, Y., Sabri, O., et al. (2016). Imaging of cerebral $\alpha 4\beta 2$* nicotinic acetylcholine receptors with (-)-[18f] flubatine pet: Implementation of bolus plus constant infusion and sensitivity to acetylcholine in human brain. Neuroimage, 141:71–80.

Honey, C. J., Newman, E. L., and Schapiro, A. C. (2017). Switching between internal and external modes: a multiscale learning principle. Network Neuroscience, 1(4):339–356.

Howe, W. M., Ji, J., Parikh, V., Williams, S., Mocaër, E., Trocmé-Thibierge, C., and Sarter, M. (2010). Enhancement of attentional performance by selective stimulation of α 4 β 2* nachrs: Underlying cholinergic mechanisms. Neuropsychopharmacology, 35(6):1391–1401.

Hwang, K., Bertolero, M. A., Liu, W. B., and D'esposito, M. (2017). The human thalamus is an integrative hub for functional brain networks. Journal of Neuroscience, 37(23):5594–5607.

Ito, T., Brincat, S. L., Siegel, M., Mill, R. D., He, B. J., Miller, E. K., Rotstein, H. G., and Cole, M. W. (2020). Task-evoked activity quenches neural correlations and variability across cortical areas. PLoS computational biology, 16(8):e1007983.

Jansen, B. H. and Rit, V. G. (1995). Electroencephalogram and visual evoked potential generation in a mathematical model of coupled cortical columns. Biological cybernetics, 73(4):357–366.

Jansen, B. H., Zouridakis, G., and Brandt, M. E. (1993). A neurophysiologically-based mathematical model of flash visual evoked potentials. Biological cybernetics, 68(3):275–283.

Kelso, J. S. (2012). Multistability and metastability: understanding dynamic coordination in the brain. Philosophical Transactions of the Royal Society B: Biological Sciences, 367(1591):906–918.

Kilgard, M. P. and Merzenich, M. M. (1998). Cortical map reorganization enabled by nucleus basalis activity. Science, 279(5357):1714–1718.

Kimura, F. (2000). Cholinergic modulation of cortical function: a hypothetical role in shifting the dynamics in cortical network. Neuroscience research, 38(1):19–26.

Klinkenberg, I., Sambeth, A., and Blokland, A. (2011). Acetylcholine and attention. Behavioural brain research, 221(2):430–442.

Komorowski, A., James, G., Philippe, C., Gryglewski, G., Bauer, A., Hienert, M., Spies, M., Kautzky, A., Vanicek, T., Hahn, A., et al. (2017). Association of protein distribution and gene

expression revealed by pet and post-mortem quantification in the serotonergic system of the human brain. Cerebral Cortex, 27(1):117–130.

Kopell, N. (2005). Does it have to be this complicated? focus on “single-column thalamocortical network model exhibiting gamma oscillations, spindles, and epileptogenic bursts”. Journal of Neurophysiology, 93(4):1829–1830.

Kowalczyk, N., Shi, F., Magnuski, M., Skorko, M., Dobrowolski, P., Kossowski, B., Marchewka, A., Bielecki, M., Kossut, M., and Brzezicka, A. (2018). Real-time strategy video game experience and structural connectivity–a diffusion tensor imaging study. Human brain mapping, 39(9):3742–3758.

Kringelbach, M. L., Cruzat, J., Cabral, J., Knudsen, G. M., Carhart-Harris, R., Whybrow, P. C., Logothetis, N. K., and Deco, G. (2020). Dynamic coupling of whole-brain neuronal and neurotransmitter systems. Proceedings of the National Academy of Sciences, 117(17):9566–9576.

Kruglikov, I. and Rudy, B. (2008). Perisomatic gaba release and thalamocortical integration onto neocortical excitatory cells are regulated by neuromodulators. Neuron, 58(6):911–924.

Lancaster, G., Iatsenko, D., Pidde, A., Ticcinelli, V., and Stefanovska, A. (2018). Surrogate data for hypothesis testing of physical systems. Physics Reports, 748:1–60.

Lancichinetti, A. and Fortunato, S. (2012). Consensus clustering in complex networks. Scientific reports, 2:336.

Latora, V. and Marchiori, M. (2001). Efficient behavior of small-world networks. Physical review letters, 87(19):198701.

Lee, T.-H., Greening, S. G., Ueno, T., Clewett, D., Ponzio, A., Sakaki, M., and Mather, M. (2018). Arousal increases neural gain via the locus coeruleus–noradrenaline system in younger adults but not in older adults. Nature Human Behaviour, 2(5):356–366.

Lenartowicz, A. and Loo, S. K. (2014). Use of eeg to diagnose adhd. Current psychiatry reports, 16(11):1–11.

Leonardi, N., Richiardi, J., Gschwind, M., Simioni, S., Annoni, J.-M., Schluep, M., Vuilleumier, P., and Van De Ville, D. (2013). Principal components of functional connectivity: a new approach to study dynamic brain connectivity during rest. NeuroImage, 83:937–950.

Leonardi, N. and Van De Ville, D. (2015). On spurious and real fluctuations of dynamic functional connectivity during rest. Neuroimage, 104:430–436.

Litwin-Kumar, A., Harris, K. D., Axel, R., Sompolinsky, H., and Abbott, L. (2017). Optimal degrees of synaptic connectivity. Neuron, 93(5):1153–1164.

Lohani, S., Moberly, A. H., Benisty, H., Landa, B., Jing, M., Li, Y., Higley, M. J., and Cardin, J. A. (2020). Dual color mesoscopic imaging reveals spatiotemporally heterogeneous coordination of cholinergic and neocortical activity. bioRxiv.

Lozano-Soldevilla, D. (2018). On the physiological modulation and potential mechanisms underlying parieto-occipital alpha oscillations. Frontiers in computational neuroscience, 12:23.

Lückmann, H. C., Jacobs, H. I., and Sack, A. T. (2014). The cross-functional role of frontoparietal regions in cognition: internal attention as the overarching mechanism. Progress in neurobiology, 116:66–86.

Luppi, A. I., Carhart-Harris, R. L., Roseman, L., Pappas, I., Menon, D. K., and Stamatakis, E. A. (2021a). Lsd alters dynamic integration and segregation in the human brain. NeuroImage, 227:117653.

Luppi, A. I., Craig, M. M., Pappas, I., Finoia, P., Williams, G. B., Allanson, J., Pickard, J. D., Owen, A. M., Naci, L., Menon, D. K., et al. (2019). Consciousness-specific dynamic interactions of brain integration and functional diversity. Nature communications, 10(1):1–12.

Luppi, A. I., Mediano, P. A., Rosas, F. E., Allanson, J., Pickard, J. D., Williams, G. B., Craig, M. M., Finoia, P., Peattie, A. R., Coppola, P., et al. (2021b). Paths to oblivion: Common neural mechanisms of anaesthesia and disorders of consciousness. bioRxiv.

Marchi, M. and Grilli, M. (2010). Presynaptic nicotinic receptors modulating neurotransmitter

release in the central nervous system: functional interactions with other coexisting receptors. Progress in neurobiology, 92(2):105–111.

Mather, M., Clewett, D., Sakaki, M., and Harley, C. W. (2016). Norepinephrine ignites local hotspots of neuronal excitation: How arousal amplifies selectivity in perception and memory. Behavioral and Brain Sciences, 39.

McGuire, B. A., Gilbert, C. D., Rivlin, P. K., and Wiesel, T. N. (1991). Targets of horizontal connections in macaque primary visual cortex. Journal of Comparative Neurology, 305(3):370–392.

Miron-Shahar, Y., Kantelhardt, J. W., Grinberg, A., Hassin-Baer, S., Blatt, I., Inzelberg, R., and Plotnik, M. (2019). Excessive phase synchronization in cortical activation during locomotion in persons with parkinson's disease. Parkinsonism & related disorders, 65:210–216.

Naganawa, M., Nabulsi, N., Henry, S., Matuskey, D., Lin, S.-F., Slieker, L., Schwarz, A. J., Kant, N., Jesudason, C., Ruley, K., et al. (2021). First-in-human assessment of 11c-lsn3172176, an m1 muscarinic acetylcholine receptor pet radiotracer. Journal of Nuclear Medicine, 62(4):553–560.

Nakamura, A., Cuesta, P., Fernández, A., Arahata, Y., Iwata, K., Kuratsubo, I., Bundo, M., Hattori, H., Sakurai, T., Fukuda, K., et al. (2018). Electromagnetic signatures of the preclinical and prodromal stages of alzheimer's disease. Brain, 141(5):1470–1485.

Newman, M. (2003). The structure and function of complex networks. SIAM review, 45(2):167–256.

Newman, M. E. (2004). Analysis of weighted networks. Physical review E, 70(5):056131.

Newman, M. E. (2006). Modularity and community structure in networks. Proceedings of the national academy of sciences, 103(23):8577–8582.

Nghiem, T.-A. E., Tort-Colet, N., Górski, T., Ferrari, U., Moghimyfiroozabad, S., Goldman, J. S., Teleńczuk, B., Capone, C., Bal, T., Di Volo, M., et al. (2020). Cholinergic switch between two types of slow waves in cerebral cortex. Cerebral Cortex, 30(6):3451–3466.

Nichols, T. E. and Holmes, A. P. (2002). Nonparametric permutation tests for functional neuroimaging: a primer with examples. Human brain mapping, 15(1):1–25.

Nieuwenhuis, S., De Geus, E. J., and Aston-Jones, G. (2011). The anatomical and functional relationship between the p3 and autonomic components of the orienting response. Psychophysiology, 48(2):162–175.

Nordberg, A., Romanelli, L., Sundwall, A., Bianchi, C., and Beani, L. (1989). Effect of acute and subchronic nicotine treatment on cortical acetylcholine release and on nicotinic receptors in rats and guinea-pigs. British journal of pharmacology, 98(1):71–78.

Opsahl, T., Colizza, V., Panzarasa, P., and Ramasco, J. J. (2008). Prominence and control: the weighted rich-club effect. Physical review letters, 101(16):168702.

Orio, P., Gatica, M., Herzog, R., Maidana, J. P., Castro, S., and Xu, K. (2018). Chaos versus noise as drivers of multistability in neural networks. Chaos: An Interdisciplinary Journal of Nonlinear Science, 28(10):106321.

Pfeffer, T., Ponce-Alvarez, A., Tsetsos, K., Meindertsma, T., Gahnström, C. J., van den Brink, R. L., Nolte, G., Engel, A. K., Deco, G., and Donner, T. H. (2021). Circuit mechanisms for the chemical modulation of cortex-wide network interactions and behavioral variability. Science Advances, 7(29):eabf5620.

Picciotto, M. R., Higley, M. J., and Mineur, Y. S. (2012). Acetylcholine as a neuromodulator: cholinergic signaling shapes nervous system function and behavior. Neuron, 76(1):116–129.

Poorthuis, R. B., Bloem, B., Schak, B., Wester, J., de Kock, C. P., and Mansvelder, H. D. (2013). Layer-specific modulation of the prefrontal cortex by nicotinic acetylcholine receptors. Cerebral cortex, 23(1):148–161.

Poorthuis, R. B. and Mansvelder, H. D. (2013). Nicotinic acetylcholine receptors controlling attention: behavior, circuits and sensitivity to disruption by nicotine. Biochemical pharmacology, 86(8):1089–1098.

Power, J. D., Barnes, K. A., Snyder, A. Z., Schlaggar, B. L., and Petersen, S. E. (2012). Spurious but systematic correlations in functional connectivity mri networks arise from subject motion. Neuroimage, 59(3):2142–2154.

Reimer, J., McGinley, M. J., Liu, Y., Rodenkirch, C., Wang, Q., McCormick, D. A., and Tolias, A. S. (2016). Pupil fluctuations track rapid changes in adrenergic and cholinergic activity in cortex. Nature communications, 7(1):1–7.

Rosas, F. E., Mediano, P. A., Gastpar, M., and Jensen, H. J. (2019). Quantifying high-order interdependencies via multivariate extensions of the mutual information. Physical Review E, 100(3):032305.

Rubinov, M. and Sporns, O. (2010). Complex network measures of brain connectivity: uses and interpretations. Neuroimage, 52(3):1059–1069.

Rubinov, M. and Sporns, O. (2011). Weight-conserving characterization of complex functional brain networks. Neuroimage, 56(4):2068–2079.

Sabri, O., Meyer, P. M., Gräf, S., Hesse, S., Wilke, S., Becker, G.-A., Rullmann, M., Patt, M., Luthardt, J., Wagenknecht, G., et al. (2018). Cognitive correlates of $\alpha 4\beta 2$ nicotinic acetylcholine receptors in mild alzheimer's dementia. Brain, 141(6):1840–1854.

Schliebs, R. and Arendt, T. (2011). The cholinergic system in aging and neuronal degeneration. Behavioural brain research, 221(2):555–563.

Schmolesky, M. (2016). The primary visual cortex. In Kolb, H., Nelson, R., Fernandez, E., and Jones, B., editors, Webvision: The Organization of the Retina and Visual System. Moran Eye Center.

Servan-Schreiber, D., Printz, H., and Cohen, J. D. (1990). A network model of catecholamine effects: gain, signal-to-noise ratio, and behavior. Science, 249(4971):892–895.

Shen, E. H., Overly, C. C., and Jones, A. R. (2012). The allen human brain atlas: comprehensive gene expression mapping of the human brain. Trends in neurosciences, 35(12):711–714.

Shine, J. M. (2019). Neuromodulatory influences on integration and segregation in the brain. Trends in cognitive sciences.

Shine, J. M., Aburn, M. J., Breakspear, M., and Poldrack, R. A. (2018a). The modulation of neural gain facilitates a transition between functional segregation and integration in the brain. Elife, 7:e31130.

Shine, J. M., Bissett, P. G., Bell, P. T., Koyejo, O., Balsters, J. H., Gorgolewski, K. J., Moodie, C. A., and Poldrack, R. A. (2016). The dynamics of functional brain networks: integrated network states during cognitive task performance. Neuron, 92(2):544–554.

Shine, J. M., Breakspear, M., Bell, P. T., Martens, K. A. E., Shine, R., Koyejo, O., Sporns, O., and Poldrack, R. A. (2019). Human cognition involves the dynamic integration of neural activity and neuromodulatory systems. Nature neuroscience, 22(2):289–296.

Shine, J. M., Müller, E. J., Munn, B., Cabral, J., Moran, R. J., and Breakspear, M. (2021). Computational models link cellular mechanisms of neuromodulation to large-scale neural dynamics. Nature neuroscience, 24(6):765–776.

Shine, J. M. and Poldrack, R. A. (2018). Principles of dynamic network reconfiguration across diverse brain states. NeuroImage, 180:396–405.

Shine, J. M., van den Brink, R. L., Hernaus, D., Nieuwenhuis, S., and Poldrack, R. A. (2018b). Catecholaminergic manipulation alters dynamic network topology across cognitive states. Network Neuroscience, 2(3):381–396.

Sporns, O. (2013). Network attributes for segregation and integration in the human brain. Current opinion in neurobiology, 23(2):162–171.

Stephan, K. E., Weiskopf, N., Drysdale, P. M., Robinson, P. A., and Friston, K. J. (2007). Comparing hemodynamic models with dcm. Neuroimage, 38(3):387–401.

Suárez, L. E., Markello, R. D., Betzel, R. F., and Misic, B. (2020). Linking structure and function in macroscale brain networks. Trends in Cognitive Sciences, 24(4):302–315.

Thiele, A. and Bellgrove, M. A. (2018). Neuromodulation of attention. Neuron, 97(4):769–785.

Tognoli, E. and Kelso, J. S. (2014). The metastable brain. Neuron, 81(1):35–48.

Tononi, G. (2004). An information integration theory of consciousness. BMC Neuroscience.

Tremblay, R., Lee, S., and Rudy, B. (2016). Gabaergic interneurons in the neocortex: from cellular properties to circuits. Neuron, 91(2):260–292.

Tzourio-Mazoyer, N., Landeau, B., Papathanassiou, D., Crivello, F., Etard, O., Delcroix, N., Mazoyer, B., and Joliot, M. (2002). Automated anatomical labeling of activations in spm using a macroscopic anatomical parcellation of the mni mri single-subject brain. Neuroimage, 15(1):273–289.

Ueno, K.-i., Togashi, H., Matsumoto, M., Ohashi, S., Saito, H., and Yoshioka, M. (2002). $\alpha 4\beta 2$ nicotinic acetylcholine receptor activation ameliorates impairment of spontaneous alternation behavior in stroke-prone spontaneously hypertensive rats, an animal model of attention deficit hyperactivity disorder. Journal of Pharmacology and Experimental Therapeutics, 302(1):95–100.

van den Heuvel, M. P., de Lange, S. C., Zalesky, A., Seguin, C., Yeo, B. T., and Schmidt, R. (2017). Proportional thresholding in resting-state fmri functional connectivity networks and consequences for patient-control connectome studies: Issues and recommendations. Neuroimage, 152:437–449.

Van Den Heuvel, M. P. and Sporns, O. (2011). Rich-club organization of the human connectome. Journal of Neuroscience, 31(44):15775–15786.

Wainstein, G., Rojas-Libano, D., Medel, V., Alnæs, D., Kolskår, K. K., Endestad, T., Laeng, B., Ossandon, T., Crossley, N., Matar, E., et al. (2021). The ascending arousal system promotes optimal performance through mesoscale network integration in a visuospatial attentional task. Network Neuroscience, 5(4):890–910.

Wang, R., Lin, P., Liu, M., Wu, Y., Zhou, T., and Zhou, C. (2019). Hierarchical connectome modes

and critical state jointly maximize human brain functional diversity. Physical review letters, 123(3):038301.

Wang, R., Liu, M., Cheng, X., Wu, Y., Hildebrandt, A., and Zhou, C. (2021a). Segregation, integration and balance of large-scale resting brain networks configure different cognitive abilities. arXiv preprint arXiv:2103.00475.

Wang, R., Su, X., Chang, Z., Lin, P., and Wu, Y. (2021b). Flexible brain transitions between hierarchical network segregation and integration associated with cognitive performance during a multisource interference task. IEEE Journal of Biomedical and Health Informatics.

Welch, P. (1967). The use of fast fourier transform for the estimation of power spectra: a method based on time averaging over short, modified periodograms. IEEE Transactions on audio and electroacoustics, 15(2):70–73.

Wendling, F., Bartolomei, F., Bellanger, J., and Chauvel, P. (2002). Epileptic fast activity can be explained by a model of impaired gabaergic dendritic inhibition. European Journal of Neuroscience, 15(9):1499–1508.

Xia, M., Wang, J., and He, Y. (2013). Brainnet viewer: a network visualization tool for human brain connectomics. PloS one, 8(7):e68910.

Xu, K., Maidana, J. P., Castro, S., and Orio, P. (2018). Synchronization transition in neuronal networks composed of chaotic or non-chaotic oscillators. Scientific reports, 8(1):1–12.

Zamora-López, G., Chen, Y., Deco, G., Kringelbach, M. L., and Zhou, C. (2016). Functional complexity emerging from anatomical constraints in the brain: the significance of network modularity and rich-clubs. Scientific Reports, 6(1):38424.

Zerbi, V., Floriou-Servou, A., Markicevic, M., Vermeiren, Y., Sturman, O., Privitera, M., von Ziegler, L., Ferrari, K. D., Weber, B., De Deyn, P. P., et al. (2019). Rapid reconfiguration of the functional connectome after chemogenetic locus coeruleus activation. Neuron, 103(4):702–718.

Zuberer, A., Kucyi, A., Yamashita, A., Wu, C. M., Walter, M., Valera, E. M., and Esterman, M.

(2021). Integration and segregation across large-scale intrinsic brain networks as a marker of sustained attention and task-unrelated thought. NeuroImage, 229:117610.